



Université du Québec
à Chicoutimi

**Effect of Zr-Bearing Dispersoids Evolution on Hot Deformation and
Recrystallization of 6xxx Alloys**

By

Ali Elashery

**Under the supervision of Prof. X.-Grant Chen and co-supervision of
Prof. Nick Parson**

**Manuscript-Based Thesis presented to the University of Quebec at Chicoutimi with a
view to obtaining the degree of Philosophiae doctor (Ph. D.) in engineering.**

Defended on 21 September 2022

BOARD OF EXAMINERS:

Professor Zhan Zhang, Department of Applied Sciences at UQAC, President of the board of examiners

Professor Daniel Larouche, Université Laval, Quebec, External Member of examiners

Professor X.-Grant Chen, department of Applied Sciences at UQAC, Internal Member of examiners

Professor Nick Parson, Rio Tinto Aluminum, Saguenay, Quebec, Internal Member of examiners

Professor Kun Liu, Department of Applied Sciences at UQAC, Internal Member of examiners

Québec, Canada

© Ali Elashery, 2022

Résumé

Actuellement, il existe une tendance vers une plus grande utilisation des alliages d'extrusion d'aluminium dans les applications automobiles en raison de leurs poids léger, de leur rapport résistance/poids élevé et de leur recyclabilité facile. Parmi les différents alliages d'aluminium, Al-Mg-Si 6xxx acquiert près de 90% de tous les produits d'extrusion d'aluminium car ils peuvent être extrudés à des vitesses plus élevées que les autres séries d'alliages avec des problèmes de qualité de surface mineurs. Le procédé de production des alliages 6xxx extrudés comprend les procédés de coulée, d'homogénéisation et de déformation à chaud suivis d'un recuit post-déformation. Le contrôle de la structure des grains est obligatoire pendant et après le procédé de déformation à chaud. Le zirconium a reçu beaucoup d'attention ces dernières années en tant qu'un élément d'ajout aux alliages d'aluminium pour inhiber la recristallisation et maintenir la structure fibreuse déformée par la précipitation de dispersoïdes de taille nanométrique.

Dans la première partie, on a étudié le comportement de précipitation des dispersoïdes contenant de Zr dans l'alliage Al-0,8%Mg-1,0%Si sous différents traitements d'homogénéisation (450-550 °C). L'effet des dispersoïdes sur la résistance à la recristallisation de l'alliage a également été étudié lors du recuit post-déformation, avec un ajout de 0,2 % en poids de Zr, on a observé deux dispersoïdes différents contenant du Zr en fonction des conditions d'homogénéisation. L'homogénéisation à 450 °C pendant 2 h a entraîné la précipitation de dispersoïdes fins et denses $L1_2$ -Al₃Zr (8-10 nm). Cependant, la prolongation en temps d'homogénéisation, tels que 12 h à 450 °C ou l'élévation de la température d'homogénéisation à 500-550 °C ont produit des dispersoïdes allongés DO₂₂- (Al, Si)₃Zr de taille plus grande. Lors des essais de compression à chaud, l'ajout de 0,2 % en poids de Zr combiné à une homogénéisation à 450 °C a augmenté la contrainte d'écoulement à haute température de 20 % par rapport à l'alliage de base sans Zr, ce qui révèle leur potentiel à inhiber le mouvement de dislocation et la restauration dynamique. Les deux dispersoïdes

ont montré un effet positif sur le retard de recristallisation lors du recuit post-déformation, mais les dispersoïdes fins et cohérents Al_3Zr sont plus efficaces que les dispersoïdes grossiers et incohérents $(\text{Al},\text{Si})_3\text{Zr}$.

Dans la deuxième partie, on a étudié le comportement de précipitation des dispersoïdes contenant de Zr dans des alliages Al-Si-Mg 6xxx avec différents niveaux d'addition de Si (0,4, 0,7 et 1,0 % en poids) et à trois températures d'homogénéisation (450, 500 et 550 °C). Les résultats ont montré une influence significative de la teneur en Si et de la température d'homogénéisation sur la précipitation de deux types de dispersoïdes contenant de Zr. Si favorise la précipitation des dispersoïdes sphériques $\text{L1}_2\text{-Al}_3\text{Zr}$ et allongés $\text{DO}_{22}\text{-(Al,Si)}_3(\text{Zr,Ti})$ lors de l'homogénéisation à basse température. Cependant, il accélère la transformation des dispersoïdes à Zr de L1_2 en DO_{22} à haute température d'homogénéisation. La contrainte d'écoulement est plus influencée par le niveau de solution solide et les paramètres de déformation à chaud que par la distribution des dispersoïdes. En raison de la distribution uniforme des dispersoïdes et des zones libres et limitées de dispersoïdes, l'alliage à haute teneur en Si (1,0 %) présente la meilleure résistance à la recristallisation parmi les trois alliages étudiés.

Dans la troisième partie, on a appliqué une homogénéisation en deux étapes pour l'alliage 6xxx contenant du Zr afin d'améliorer les caractéristiques des dispersoïdes contenant du Zr et la résistance à la recristallisation. Les traitements d'homogénéisation en deux étapes étaient composés d'une première étape à 400 °C pendant 48 h et d'une deuxième étape à 500 °C pendant 2 et 5 h comparés à une homogénéisation en une seule étape réalisée à 500 °C pendant 2 et 5 h. Pour étudier la résistance à la recristallisation, un recuit post-déformation à 500 °C pendant 1 h a été effectué sur les échantillons déformés. Les résultats ont montré que les caractéristiques des dispersoïdes étaient significativement améliorées en utilisant l'homogénéisation en deux étapes par rapport à l'homogénéisation en une seule étape, où la densité numérique des dispersoïdes $\text{L1}_2\text{-Al}_3\text{Zr}$ augmentait de 75 à 145 % tandis que leur taille diminuait de 9 à 25 %, ajoutant que la distribution des dispersoïdes

$DO_{22}-(Al,Si)_3(Zr,Ti)$ sont devenus plus uniformes. Les caractéristiques améliorées des dispersoïdes contenant de Zr et les plus étroites zones sans dispersoïdes produites par l'homogénéisation en deux étapes ont considérablement amélioré la résistance à la recristallisation, réduisant la fraction de surface recristallisée en atteignant 85 % par rapport à l'homogénéisation en une seule étape.

Dans la quatrième partie, on a étudié le comportement de précipitation des dispersoïdes contenant Zr dans les alliages Al-Mg-Si-Zr pendant différents traitements thermiques par microscopie électronique à transmission. De plus, le comportement de transformation de la métastable $L1_2$ à l'équilibre DO_{22} a été étudié au moyen d'un traitement en une et deux étapes. Les résultats ont montré que $L1_2$ a précipité préférentiellement le long des directions $\langle 001 \rangle$ de α -al aux premiers stades de la nucléation, coïncidant avec les mêmes sites et orientation de β' - Mg_2Si décomposée à basse température. Les zones enrichies de Si laissées après la dissolution de β' - Mg_2Si ont pu agir comme des sites hétérogènes pour les dispersoïdes $L1_2-Al_3Zr$. De plus, le profil de concentration Zr à travers le grain a joué un rôle crucial dans l'introduction de la force motrice des précipitations. D'un autre côté, la précipitation précoce des dispersoïdes DO_{22} a été observée le long des directions $\langle 001 \rangle$ de α -al (au-dessus de 500 ° C), suggérant une transformation des dispersoïdes $L1_2$ préexistants plutôt que nucléés directement à partir de la matrice d'aluminium. La présence de paroi anti-phase (APB) au milieu des dispersoïdes $L1_2$ a été observée aux premiers stades de la transformation, qui ont préférentiellement grandi le long des directions $\langle 001 \rangle$ vers la structure DO_{22} finale

Abstract

Currently, there is a trend in the increased use of aluminum extrusion alloys in automotive applications due to their light weight, high strength-to-weight ratio, and easy recyclability. Among the different aluminum alloys, Al-Mg-Si 6xxx acquire nearly 90% of all aluminum extrusion products since they can be extruded at higher speeds than other alloy series with more minor surface quality problems. The manufacturing process of the extruded 6xxx alloys includes casting, homogenization, and hot deformation processes followed, sometimes, by post-deformation annealing. Controlling the grain structure is mandatory during and after the hot deformation process. Zirconium has received much attention in recent years as an addition to aluminum alloys to inhibit the recrystallization and maintain the deformed fibrous structure through the precipitation of nano-sized dispersoids.

In the first part, the precipitation behavior of Zr-bearing dispersoids in an Al-0.8%Mg-1.0%Si alloy was investigated for different homogenization treatments (450-550 °C). The effect of the dispersoids on the recrystallization resistance of the alloy was also studied during post-deformation annealing. With an addition of 0.2 wt.% Zr, two different Zr-bearing dispersoids were observed depending on the homogenization conditions. Homogenization at 450 °C for 2 h resulted in the precipitation of fine and dense $L1_2$ -Al₃Zr dispersoids (8-10 nm). In contrast, extended homogenization times, such as 12 h at 450 °C or increasing the homogenization temperature to 500-550 °C, produced elongated DO₂₂-(Al,Si)₃Zr dispersoids with a larger size. During hot compression testing, the addition of 0.2 wt.% Zr combined with homogenization at 450 °C increased the high-temperature flow stress by 20% relative to the base alloy free of Zr, revealing their potential to inhibit dislocation motion and dynamic

recovery. Both dispersoids were found to have a positive impact on the retardation of recrystallization during post-deformation annealing, but the fine and coherent Al_3Zr dispersoids were more effective than the coarse and incoherent $(\text{Al,Si})_3\text{Zr}$ dispersoids.

In the second part, the precipitation behavior of Zr-bearing dispersoids is investigated in Al-Si-Mg 6xxx alloys with different Si levels (0.4, 0.7, and 1.0 wt%) at three homogenization temperatures (450, 500, and 550 °C). The results showed a significant influence of the Si level and homogenization temperature on the precipitation of two types of Zr-bearing dispersoids. Si promotes the precipitation of both spherical $\text{L1}_2\text{-Al}_3\text{Zr}$ and elongated $\text{DO}_{22}\text{-(Al,Si)}_3\text{(Zr,Ti)}$ dispersoids during low-temperature homogenization. However, it accelerates the transformation of Zr dispersoids from L1_2 to DO_{22} at high homogenization temperature. The flow stress is more influenced by the solid solution level and hot deformation parameters rather than by the dispersoid distribution. Owing to the uniform distribution of dispersoids and limited dispersoid free zones, the high Si alloy (1.0%) exhibits the best recrystallization resistance among the three alloys studied.

In the third part, two-step homogenization was applied to a Zr-containing 6xxx alloy to enhance the characteristics of Zr-bearing dispersoids and recrystallization resistance. The two-step homogenization treatments were composed of the first step at 400 °C for 48 h and a second step at 500 °C for 2 and 5 h and compared with single-step homogenization conducted at 500 °C for 2 and 5 h. To study the recrystallization resistance, post-deformation annealing at 500 °C for 1 h was performed on the deformed samples. The results showed that compared to single-step homogenization, the dispersoid characteristics were significantly improved using two-step homogenization, where the number density of $\text{L1}_2\text{-Al}_3\text{Zr}$ dispersoids increased by 75 to 145% while their size decreased by 9 to 25% and the

distribution of the $\text{DO}_{22}\text{-(Al, Si)}_3\text{(Zr, Ti)}$ dispersoids became more uniform. The improved characteristics of Zr-bearing dispersoids and the narrower dispersoid-free zones produced by the two-step homogenization significantly improved the recrystallization resistance, reducing the recrystallized area fraction by reaching 85% when compared with single-step homogenization.

In the fourth part, the precipitation behavior of Zr-bearing dispersoids in Al-Mg-Si-Zr alloys during different heat treatments was studied by transmission electron microscopy. Also, the transformation behavior of metastable L_{12} to the equilibrium DO_{22} was studied by means of single- and two-step treatment. The results showed that L_{12} precipitated preferentially along $\langle 001 \rangle_{\alpha\text{-Al}}$ directions at the early stages of nucleation, coinciding with the same sites and orientation of β' - Mg_2Si decomposed at low temperature. The Si enriched areas left after the dissolution of β' - Mg_2Si could act as heterogeneous sites for $\text{L}_{12}\text{-Al}_3\text{Zr}$ dispersoids. In addition, the Zr concentration profile across the grain played a crucial role in introducing the driving force of precipitation. On the other hand, the early precipitation of DO_{22} dispersoids was observed to be precipitated along $\langle 001 \rangle_{\alpha\text{-Al}}$ directions (above 500 °C), suggesting a transformation of the pre-existing L_{12} dispersoids rather than nucleated directly from the aluminum matrix. The presence of anti-phase boundary (APB) in the middle of the L_{12} dispersoids was observed at the early stages of transformation, which preferentially grew along $\langle 001 \rangle$ directions to the final DO_{22} structure.

Table of Contents

Résumé.....	iii
Table of Contents.....	ix
List of Figures.....	xii
List of Tables.....	xvii
DEDICATION.....	xviii
ACKNOWLEDGEMENT.....	xix
CHAPTER 1 : INTRODUCTION.....	1
1.1. Background.....	1
1.1.1. 6xxx series alloys.....	3
1.1.2. Hot deformation behaviour and softening mechanisms.....	5
1.1.3. Post deformation annealing and static recrystallization.....	7
1.1.4. Zener-drag effect.....	8
1.1.5. Zirconium micro-alloying and related dispersoids.....	10
1.1.6. Effect of Zr dispersoids on recrystallization.....	13
1.2. Definition of the problem.....	15
1.3. Objectives.....	17
1.4. Originality Statement.....	19
1.5. Thesis outlines.....	21
CHAPTER 2: Evolution of Zr-Bearing Dispersoids During Homogenization and Their Effects on Hot Deformation and Recrystallization Resistance in Al-0.8%Mg-1.0%Si Alloy	30
Abstract.....	30
2.1. Introduction.....	31

2.2. Experimental work	33
2.3. Results and Discussion.....	35
2.3.1. As cast and homogenized microstructures	35
2.3.2. Evolution of Zr-bearing dispersoids.....	40
2.3.3. Hot deformation behavior.....	46
2.3.4. Recrystallization resistance	49
2.4. Conclusions	54
References	56
CHAPTER 3 : Effect of Si Level on the Evolution of Zr-bearing Dispersoids and the Related Hot Deformation and Recrystallization Behaviors in Al-Si-Mg 6xxx Alloys	
Abstract	60
3.1. Introduction	61
3.2. Experimental procedures.....	63
3.3. Results and discussion.....	66
3.3.1. As-cast microstructure.....	66
3.3.2. Evolution of Zr-bearing dispersoids during homogenization.....	67
3.3.3. Hot deformation behavior.....	77
3.4. Conclusions	92
References	93
CHAPTER 4: Improving the dispersoid distribution and recrystallization resistance of a Zr-containing 6xxx alloy using two-step homogenization	
4.1. Introduction	99
4.2. Experimental procedures.....	101
4.3. Results and discussion.....	104
5.3.1. Dispersoid Microstructure	104
5.3.2. Flow stress	111

5.3.3. Recrystallization resistance	112
4.4. Conclusions	119
CHAPTER 5: Nucleation and Transformation of Zr-bearing dispersoids in Al-Mg-Si 6xxx alloys	124
Abstract	124
5.1. Introduction	125
5.2. Experimental Procedures	127
5.3. Results and discussion.....	128
5.3.1. The nucleation of L1 ₂ dispersoids	128
5.2. The Transformation of L1 ₂ to DO ₂₂	135
5.3. The precipitation of dispersoids during one-step treatment	140
5.4. Conclusions	145
References	146
CHAPTER 6: GENERAL CONCLUSIONS AND RECOMMENDATIONS	150
6.1. General Conclusions	150
6.2. Recommendations	153
List of Publications	155

List of Figures

Figure 1.1 Typical 6xxx alloys with their range of Si and Mg amounts .	4
Figure 1.2 Typical thermomechanical steps of the manufacturing of 6xxx alloys.	5
Figure 1.3 The typical three cases of the flow curve behaviours. ©Ali Elashery 2022	6
Figure 2.1 SEM images of as-cast microstructure and EBSD images of grain distribution for the base (a,c) and 0.2Zr (b,d) alloys.	36
Figure 2.2 Optical micrographs showing the base alloy microstructure for different homogenization conditions.	38
Figure 2.3 Optical micrographs showing the 0.2Zr alloy microstructure of for different homogenization conditions. The black arrows in (d) and (e) indicate dispersoid zones (DZs).	39
Figure 2.4 SEM images showing the Zr bearing dispersoids in the 0.2Zr alloy after homogenization at 450 °C (a), 500 °C (b), and 550 °C (c) for 12 h soaking time.	39
Figure 2.5 Bright field TEM images of 0.2Zr alloy for different homogenization conditions: (a,b) 450 °C for 2 and 12 h, (c,d) 500 °C for 2 and 12 h, and (e,f) 550 °C for 2 and 12 h.	41
Figure 2.6 Identification of Zr-bearing dispersoids: (a) dark field TEM image showing L1 ₂ -Al ₃ Zr dispersoids after homogenization at 450 °C for 2 h; (b) SAEDP corresponding to (a); (c) bright field TEM image showing DO ₂₂ -(Al,Si) ₃ Zr dispersoids after homogenization at 550 °C for 12 h; (d) SAEDP corresponding to (c); and (e) TEM-EDS analysis of DO ₂₂ -(Al,Si) ₃ Zr dispersoids.	43
Figure 2.7 Number density (a) and average size (b) of L1 ₂ -Al ₃ Zr and DO ₂₂ -(Al,Si) ₃ Zr dispersoids at different homogenization conditions.	45
Figure 2.8 Typical flow curves at 400°C and 1 s ⁻¹ strain rate: (a) base alloy and (b) 0.2Zr alloy. WH refers to the work hardening which mainly controls the flow behavior in the first stages of compression, while WH + DS refers to both the work hardening and the dynamic softening after reaching the peak flow stress.	46
Figure 2.9 Euler orientation maps of as-deformed structures after hot deformation (400 °C, 1 s ⁻¹) for the base alloy (a, b) and 0.2Zr alloy (c, d) homogenized at 450°C/2h and 550°C/2hr, respectively. Low angle (2°-5°), medium angle (5°-15°), and high	

angle boundaries ($>15^\circ$) are represented by white, green, and black lines, respectively.	49
Figure 2.10 Euler orientation maps after annealing (500 °C for 4 h) for the base (a, b) and 0.2Zr alloys (c, d) for two homogenization conditions (450°C/2h and 550°C/2h). Low angle (2° - 5°), medium angle (5° - 15°), and high angle boundaries ($>15^\circ$) are represented by white, green, and black lines, respectively.	50
Figure 2.11 Misorientation angle distribution for base and 0.2Zr alloys for different homogenization conditions after annealing treatment at 500 °C for 4 h.	52
Figure 2.12 OM dark field image (a) and dark field TEM image (b) of 0.2Zr alloy homogenized at 550°C/2h (a) and 450°C/2h (b), respectively.	54
Figure 3.1 SEM images of As-cast condition for (a) 0.4Si, (b) 0.7Si and (c) 1.0Si alloys.	66
Figure 3.2 Dark-field optical micrographs showing the distribution of Zr-bearing dispersoids for different Si levels and homogenization temperatures.	68
Figure 3.3 SEM micrographs showing Zr-dispersoids and β -Mg ₂ Si (large particles indicated by white arrows) after homogenization at 450°C/5h (a-c) and 550°C/5h (d-f) for 0.4Si, 0.7Si and 1.0Si alloys, and (g) SEM-EDS analysis of β -Mg ₂ Si particle.	69
Figure 3.4. Bright-Field TEM images of (a) 0.4Si, (b) 0.7Si, and (c) 1.0Si alloys after homogenization at 550°C/5h and TEM-EDS analysis of (d) spherical and (e) elongated dispersoids.	71
Figure 3.5 Dark-field TEM images for the spherical Al ₃ Zr dispersoids at different Si levels and homogenization temperatures.	73
Figure 3.6 Number density of spherical dispersoids (a) and elongated dispersoids (b) for Si and homogenization variants	75
Figure 3.7 Schematic illustration of the evolution of Zr-bearing dispersoids, β -Mg ₂ Si and DFZs in different alloys during low- and high-temperature homogenization. .	77
Figure 3.8 Typical flow curves in different Z conditions for (a) 0.4Si, (b) 0.7Si and (c) 1.0Si alloys under different homogenization conditions.	79
Figure 3.9 Flow stress at a strain of 0.7 in the high Z condition for the Si and homogenization variants.	81
Figure 3.10 Electrical conductivity for the Si and homogenization variants.	81
Figure 3.11 All-Euler orientation maps of as-deformed structures in the high Z condition (350 °C, 1.0 s^{-1}) for: (a, d) 0.4Si, (b, e) 0.7Si and (c, f) 1.0Si alloys homogenized	

at (a-c) 450°C/5h and (d-f) 550°C/5h. Low angle (2°-5°), medium angle (6°-15°), and high angle boundaries (>15°) were represented by white, green, and black lines, respectively.....	83
Figure 3.12 All-Euler orientation maps of as-deformed structures in the low Z condition (450°C, 0.001 s ⁻¹) for: (a, d) 0.4Si, (b, e) 0.7Si and (c, f) 1.0Si alloys homogenized at (a-c) 450°C/5h and (d-f) 550°C/5h. Low angle (2°-5°), medium angle (6°-15°), and high angle boundaries (>15°) were represented by white, green, and black lines, respectively.....	85
Figure 3.13 Misorientation angle fractions after deformation at high Z and low Z (a) 0.4Si, (b) 0.7Si and (c) 1.0Si alloys homogenized at different temperatures.....	86
Figure 3.14 All-Euler orientation maps after annealing at 500°C/1h for: (a, d) 0.4Si, (b, e) 0.7Si and (c, f) 1.0Si alloys homogenized at (a-c) 450°C/5h and (d-f) 550°C/5h.	88
Figure 3.15 All-Euler orientation maps after annealing at 540°C/1h for: (a, d) 0.4Si, (b, e) 0.7Si and (c, f) 1.0Si alloys homogenized at (a-c) 450°C/5h and (d-f) 550°C/5h.	89
Figure 3.16 Recrystallization area fractions after annealing at 500°C/1h and 540°C/1h for Si and homogenization variants.	90
Figure 4.1 Schematic diagrams of the homogenization treatments, (a) single-step and (b) two-step treatments.	102
Figure 4.2 TEM dark-field images of Al ₃ Zr dispersoids formed after different homogenization treatments: (a) 400°C/48h (first step), (b) 500°C/2h, (c) 500°C/5h, (d) 400°C/48h + 500°C/2h and (e) 400°C/48h + 500°C/5h.	105
Figure 4.3 Bright field TEM images near grain boundaries showing the width of DFZs in, (a) single- step 500°C/2h, and (b) two-step 400°C/48 h + 500°C/2h homogenization conditions.	108
Figure 4.4 (a) Bright field TEM image showing the elongated DO ₂₂ -(Al,Si) ₃ (Zr,Ti) dispersoids and (b) the corresponding TEM-EDS spectrum.	109
Figure 4.5 Optical dark field and SEM images showing the distribution of the DO ₂₂ -(Al,Si) ₃ (Zr,Ti) dispersoids for single-step 500°C/5h (a-c) and two-step 400°C/48h + 500°C/5h (d-f) treatments.	110
Figure 4.6. Typical flow stress curves after deformation at 350 °C and 1.0 s ⁻¹ in different homogenization conditions.	112

Figure 4.7. Grain spread orientation maps for different alloy conditions after deformation at 350 °C and 1.0 s ⁻¹ and annealing at 500 °C for 1 h.	114
Figure 4.8 Recrystallization area fraction for different alloy conditions after deformation at 350 °C and 1.0 s ⁻¹ and annealing at 500 °C for 1 h.	115
Figure 4.9 All-Euler orientation maps of as-deformed (a, b) and annealed (c, d) grain structures for the single-step homogenization of 500°C/2h (a, c) and the two-step homogenization of 400°C/48h + 500°C/2h (b, d). Low angle (2°-5°), medium angle (6°-15°), and high angle boundaries (>15°) are represented by white, green, and black lines, respectively.	116
Figure 4.10 The misorientation angle distribution of as-deformed (a, b) and annealed (c, d) grain structures for the single-step homogenization of 500°C/2h (a, c) and the two-step homogenization of 400°C/48 h + 500°C/2h (b, d).	117
Figure 5.1 Different heat treatment procedures performed on the studied alloy.	128
Figure 5.2 Bright-field TEM images showing the precipitation during heating to 400 °C for the samples quenched from (a) 200 °C, (a) 300 °C, (a) 400 °C.	130
Figure 5.3 Dark-field TEM images of samples isothermally held for (a) 2 h, (b) 5 h, (c)12 h and (d) 48 h at 400 °C.	132
Figure 5.4 a) bright-field TEM image showing the precipitation of β ¹ -Mg _{1.8} Si in the L-Si alloy quenched at 300 °C, and the dark-field TEM images of L ₁₂ -Al ₃ Zr precipitation after isothermal holding at 400 °C for (b) 5 h and (c) 48 h.	133
Figure 5.5 Montage of dark-field TEM micrographs of the sample holding at 400 °C for 12 h showing the precipitation of Al ₃ Zr dispersoids across the grain.	135
Figure 5.6 The evolution of dispersoids after heating ramp from 400 °C to 500 °C (a,b) and 550 °C (c,d) after the samples hold at 400°C/48h.	137
Figure 5.7 Bright-field TEM images during heating to 550 °C after the first step of 400°C/48h and TEM-EDS line scans of Si and Zr distribution across typical dispersoids (arrow-marked); (a) spherical, (b) ellipsoidal and (c) elongated dispersoids.	139
Figure 5.8 Dark-filed TEM images showing the transformation sequence of spherical L ₁₂ dispersoids into elongated DO ₂₂ dispersoids.	140
Figure 5.9 The evolution of dispersoids after ramp heating from RT to 500 °C (a,b,c) and 550 °C (d,e,f).	142

Figure 5.10 Schematic illustration of the nucleation and transformation of Zr-bearing dispersoids in Al-Mg-Si 6xxx alloys. 144

List of Tables

Table 2.1 Chemical composition (wt.%) of the experimental alloys.....	34
Table 2.2. Quantitative analysis of EBSD results.....	52
Table 3.1. Chemical composition (wt.%) of the experimental alloys.....	65
Table 4.1: Chemical composition of the studied 6xxx alloy (wt.%).	102
Table 4.2. Characteristics of Al ₃ Zr dispersoids after different homogenization treatments.	106

DEDICATION

To the memory of my mother, *Fatma Elhdad*,

who has been the whole world for me.

To my father, *Ahmed Elashery*,

who is the role model of my entire life.

To my wife, *Amira Ibrahim*,

My love, My life, My strength

ACKNOWLEDGEMENT

I would like to express my sincere gratitude to everyone who helped, encouraged, and supported me during my Ph.D. study at the University of Quebec at Chicoutimi (UQAC).

First and foremost, I would like to express my sincere gratitude to my thesis supervisor Prof. X.-Grant Chen for offering me the opportunity to conduct Ph.D. research in Canada. I also convey a great appreciation for his continuous trust, support, patience, motivation, immense knowledge, stimulating ideas and enlightening discussions. Without his timely help and valuable advice, I could not have completed this thesis.

My deep appreciation also goes to my co-supervisor, Dr. Nick Parson from Arvida Research & Development Centre (ARDC) of Rio Tinto, for his industrial expertise, guidance and suggestions during the planning and development of the research tasks as well as the paper writing.

I am also thankful to Prof. Emad Elgallad for his encouragement and whole-hearted support; his valuable suggestions, comments, and scientific discussions played a crucial role in the improvements of the papers and thesis quality. He always inspired me to explore new possibilities.

A special thanks to Prof. Zhan Zhang and Mr. Zhixing Chen for helping me to conduct SEM and TEM observations. Also, Thanks to Prof. Kun liu for the valuable scientific discussions. I would like to convey my sincere gratitude to Prof. Khaled Ragab for giving me a chance to make my dream come true. He greatly supported my wife and me in

settling down in Chicoutimi and adapting to the new environment and culture. He has always been supportive during my study and treated me as his brother.

I would also like to thank all the staff in CURAL for their help and support. Special thanks go to our technicians, Mr. Dany Racine, Mr. Samuel Dessureault, Mr. Felix Tremblay and Mr. Dave Girard, for supporting our experiments in CURAL.

I am also deeply indebted to all my colleagues and friends in the department for their kind support, scientific discussions, suggestions, and for making my life much more delightful in Chicoutimi: Siamak Nikzad, M. Attia, Jovid Rakhmonov, A. Algendy, M. Ramadan, M. Hafez, Chaima Hajji, Mohammadreza Mofarreh, Peng Hu, Liying Cui, Zimeng Wang, Redouane Farid, Henry Agbe, Karthikeyan Rajan, and Lanfeng Jin, Alyaa bakr, Abhishek.

Finally, but no means least, I would like to thank my beloved wife for her unconditional love and infinite encouragement throughout my PhD research. I cannot find words to express my gratitude to her. Most importantly, I could not possibly finish this work without the encouragement and support of my father and my sister. Warm wishes to my whole family for their unending love and trust throughout my education.

This project was financially supported by the Natural Science and Engineering Research Council of Canada (NSERC) and Rio Tinto Aluminum through the NSERC Industry Research Chair in the Metallurgy of Aluminum Transformation at Université du Québec à Chicoutimi (UQAC). I would like to thank both organizations for their support during my study.

CHAPTER 1 : INTRODUCTION

1.1. Background

The trend to reduce vehicle fuel emissions continues to offset the effect on global warming. Therefore, the industrial demand to develop light, fuel-efficient automobiles has increased rapidly. Because of their high strength-to-weight ratio, good weldability, and suitability for different product forms, Al-Mg-Si 6xxx aluminum alloys are excellent candidates for manufacturing automotive parts, such as front rails, bumpers, and structural body components [1]. These alloys are commonly used in the form of extruded profiles acquiring nearly 90% of all aluminum extrusion products since they can be extruded at higher speeds than other alloy series with more minor surface quality problems [2]. Hence, hot deformation and mainly the extrusion could be considered as the main plastic deformation processes for 6xxx aluminum alloys used to achieve the desirable and complex geometric profiles. However, maintaining a fibrous grain structure substantially improves strength, fatigue, and toughness properties [3]. Also, controlling the grain structure is vital for adequate performance during post-deformation processes such as annealing or solution treatment usually performed on 6xxx alloys [4]. In this regard, adjusting the alloy chemistry, homogenization treatment, and hot deformation parameters are the main approaches.

Commonly, there are two main approaches to inhibit recrystallization during the hot deformation process. The first approach is to optimize the processing parameters (temperature, deformation speed...., etc.). The other approach is to control the grain structure during and after the hot deformation of 6xxx alloys by adding transition elements that have

limited solubility and diffusivity in the aluminum matrix [5, 6]. Among these elements, Zr has received much attention in recent years to be added to certain aluminum alloys [3, 7, 8]. In addition to its relatively low cost, it has a very low diffusivity and perfect lattice mismatch with the aluminum matrix [9]. It has been proven to positively affect the flow stresses and recrystallization resistance of several aluminum alloys [7, 10, 11]. This could be achieved by introducing a high density of coherent $L1_2$ - Al_3Zr dispersoids that precipitated during homogenization treatment. However, the precipitation behavior of such dispersoids is significantly altered by either the homogenization parameters (i.e., temperature and soaking time) or by adding other solutes such as Si, which exist in a considerable amount in 6xxx alloys.

The pinning effect of the dispersoids depends on the size, number density, and inter-particle spacing, which are strongly influenced by the homogenization process [12]. Therefore, the homogenization parameters should be carefully selected to optimize dispersoid characteristics. Commonly, the conventional single-step homogenization at high temperatures, *i.e.*, ~ 550 °C, aims to reduce microsegregation, dissolve the low melting eutectic phases, and refine /transform the iron-rich constituent particles than optimizing the dispersoid precipitation. However, only a few coarse dispersoids may be formed at such high temperatures. In contrast, homogenization at lower temperatures promotes the nucleation of dispersoids rather than their growth, resulting in a high number density of fine dispersoids, but it fails to fulfill the industrial requirements. Two-step homogenization is a recent approach that combines both low- and high-temperature homogenization advantages. The

first step is commonly conducted at a low temperature for a relatively long soaking time, while a much higher temperature for a shorter time is used for the second step.

1.1.1. 6xxx series alloys

The 6xxx series alloys refer to the heat treatable Al-Mg-Si alloys. Due to the versatile mechanical properties of these alloys, they are widely used in the construction and transportation industries. Magnesium and Si are their main alloying elements added in a proper ratio to form strengthening Mg-Si precipitates. Figure 1.1 shows some typical 6xxx alloys with the range of Mg and Si and the average strength. The content of Mg and Si determines the potential strength that can be acquired either by the solution strengthening or through the precipitation strengthening during the age-hardening treatment. The general sequence of the precipitation is solid solution \rightarrow GP zones \rightarrow β'' \rightarrow β' \rightarrow β (Mg_2Si) [13]. The coherent needle-like β'' precipitates are considered to have the highest strengthening effect in 6xxx alloys [14]. This type of precipitate has the stoichiometry of Mg_5Si_6 , which has an Mg: Si ratio close to 1.0.

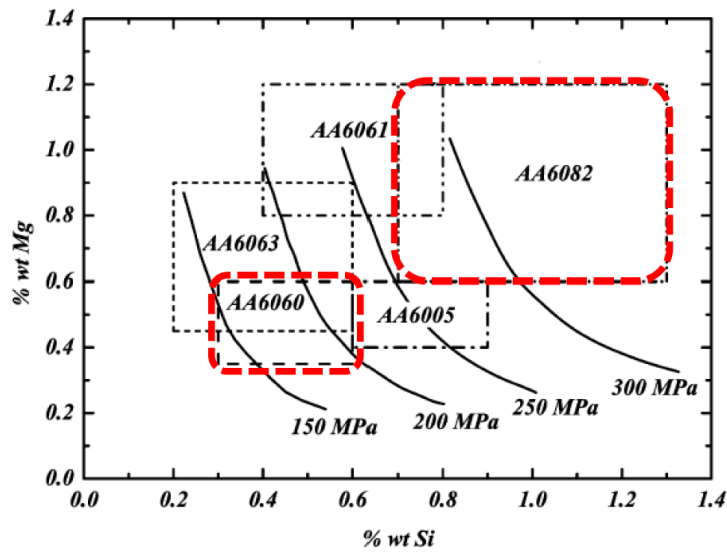


Figure 1.1 Typical 6xxx alloys with their range of Si and Mg amounts [15].

AA6xxx alloys are the dominant Al alloys for extrusion due to their ease of extrusion, relatively low cost, versatility, superior surface appearance and strength [16-18]. The manufacturing of the extruded 6xxx alloys (Figure 1.2) includes DC casting of the billets, followed by homogenization, extrusion and the post extrusion treatment, namely the aging treatment to achieve the desired mechanical properties. The main purposes of the homogenization treatment are (1) dissolving the low melting eutectics such as the primary Mg_2Si particles; (2) reducing the microsegregation of Mg and Si; (3) fragmentation and transformation of large intermetallics and (4) the precipitation of small dispersoids. Such microstructural development that occurs during the homogenization treatment significantly impacts the downstream hot deformation behaviour and the subsequent microstructure and mechanical properties.

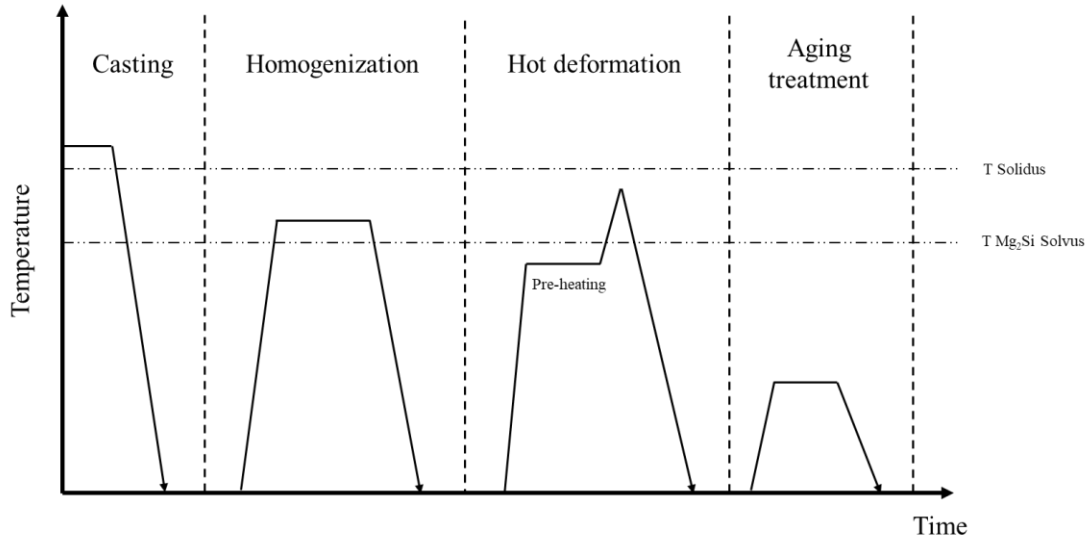


Figure 1.2 Typical thermomechanical steps of the manufacturing of 6xxx alloys. ©Ali

Elashery 2022

1.1.2. Hot deformation behaviour and softening mechanisms

In general, aluminum alloys have a high stacking fault energy (SFE, 250 mJ/m²) which facilitates the dislocation slipping in the lattice structure during the plastic deformation [19]. The slipping occurs in the most densely packed planes and in the most densely packed directions in the crystal. However, at high temperatures, more slipping systems could be activated, resulting in multi-slip of dislocations [20]. During the hot deformation, the stress required to sustain the plastic deformation at constant temperature and strain rate is defined as flow stress. The high-temperature flow stress is one of the most important factors for the extrusion of 6xxx alloys to determine the required pressure and to determine the kinetics of the metallurgical transformation [21]. Depending on the dominant hardening/ softening mechanism, the flow stress curves can be divided into three typical cases (figure 1.3). In the first case, the flow stress rises rapidly with an increase in the strain and then continues to

increase at a lower rate. Such behaviour indicates that the work hardening rate is dominant due to the higher rate of dislocation multiplication. In the second case, the flow stress rises to a plateau followed by steady stress, demonstrating a dynamic balance between the work hardening and the softening mechanisms. For the third case, a sudden decrease of the flow stress obtained after exhibiting a peak at certain strain, indicating the enhancement of the softening mechanisms.

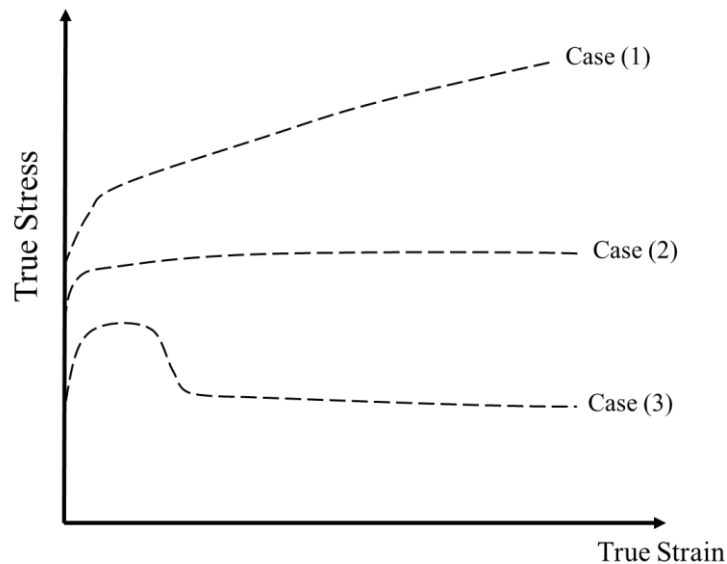


Figure 1.3 The typical three cases of the flow curve behaviours. ©Ali Elashery 2022

The work hardening arises when dislocation motion is hindered by obstacles such as other dislocations, solute atoms and dispersoids, requiring high stress to continue the plastic deformation. The increase of dislocation density and work hardening are continuously counteracted by the dynamic softening processes during the deformation at elevated temperatures. Dynamic recovery (DRV) and dynamic recrystallization (DRX) are the common softening mechanisms that occur in aluminum alloys during thermomechanical processing. The high temperature provides the energy for the dislocation to move and annihilate each other, leading to softening of the material through the recovery process. DRV

is the most frequently encountered softening mechanism since they have high stacking fault energy, high dislocation mobility, and low grain boundary mobility [22]. However, if the rate of dislocation annihilation is not sufficient, the driving force of recrystallization during the thermomechanical process increases. DRX can occur by the development or formation of new grains at deformation conditions (i.e., deformation temperature and strain rate). The powerful Zener-Hollomon parameter (Z) can describe the combined effect of the temperature and strain rate on the flow stress and the microstructure evolution during hot deformation [23].

1.1.3. Post deformation annealing and static recrystallization

After the hot deformation of 6xxx alloys, a post-deformation heat treatment is usually performed, such as annealing or solutionizing treatment. The annealing treatment is usually used to reduce the internal stresses evolved during the deformation process and to get a stable property. On the other hand, the solutionizing treatment at high temperature is required to dissolve all Mg-Si particles to maximize the age-hardening effect. However, Static recrystallization (SRX) can occur during post-deformation heat treatment in the case of weak recrystallization resistance. Unlike the dynamic recrystallization that occurred during the deformation process, SRX occurs after deformation by the migration of grain boundaries and nucleation and growth of new grains [24]. It is known that a deformed state and prior plastic strain significantly affect the recrystallization characteristics [25]. The substructures formed during deformation and the annealing temperature are the driving force for the nucleation of the recrystallized grains.

To retain the mechanical properties of the deformed 6xxx alloys, the fibrous grain texture has to be maintained, particularly, during the post-deformation heat treatments. Partial recrystallization is undesirable due to its detrimental effect on mechanical properties, surface quality and corrosion resistance [26-28]. For instance, Birol [29] found that the soft zones of the partially recrystallized structures acted as a favourable site for crack initiation and propagation in 6005A tube extrusions. Also, the formation of recrystallized grain bands leads to decreased strength and toughness, as reported in the case of 7xxx alloys [30]. Hence, the recrystallized volume fraction should be minimized by hindering the dislocation motion and grain boundaries migration.

1.1.4. Zener-drag effect

The grain structure can be significantly inhibited by the interaction between the pre-existing thermally stable dispersoids and grain boundaries [31, 32]. When small dispersoids are present at the grain boundary, they will exert a dragging force which could hinder the grain boundary movement and hence the process of recovery, recrystallization, and grain growth. This effect is referred to as the Zener pinning effect. The Zener pinning pressure represents the magnitude of the force exerted in a direction opposite to the boundary movement and is expressed by the following equation:

$$F_Z = \frac{3f\gamma}{4R}$$

Where f is the volume fraction of dispersoids, R is particle radius, and γ is the grain boundary energy.

According to the equation above, for a given volume fraction, the smaller the particle, the greater the dragging force. However, several other parameters can affect this interaction,

such as dispersoid morphology, coherency and distributions. Regarding particle morphology, the pinning models typically assume that particles are geometrically spherical. It has been reported [33] that the disk or needle-shaped particles may offer greater pinning resistance or Zener drag to migrating boundaries than spherical ones. However, the pinning resistance of non-spherical particles is very sensitive to particle orientation and aspect ratio [34]. Additionally, the coherency of the particles is also important, but not as much as the morphology factor [35]. In general, the coherent dispersoids exert higher Zener drag force compared to the incoherent ones. It is believed that the pinning pressure can be twice higher than that of the incoherent particles having the same size due to the additional force of creating a new interface when the grain boundary passes [35, 36]. Finally, the homogenous distribution of the dispersoids is very important for having a uniform pinning effect across the microstructure [37]. In contrast, the spatial distribution leads to the formation of dispersoids free zones (DFZs) where the minimum pinning force exists [38].

The use of dispersoids in Al alloys is a well-established method of controlling grain growth and recrystallization during annealing treatment via Zener pinning, which considers one of the most important factors in determining the recrystallized grain size [39]. An example of where Zener pinning has been used is in AA6xxx aluminum alloys to improve the grain size stability at elevated temperatures of a fine-grained superplastic material through the addition of zirconium. Zirconium produced small precipitates, which did not dissolve at high temperatures and helped to prevent grain growth [40].

1.1.5. Zirconium micro-alloying and related dispersoids

The addition of micro-alloying elements, such as Zr, V, Sc, Sn, In, Cd, and Ag, has been reported to increase the material strength of the alloys and afford reasonably high toughness by precipitation of dispersoids [41, 42]. Among these elements, Zr offers the lowest diffusivity and very low solubility in the aluminum matrix. The addition of Zr to aluminum alloys has several advantages. It can be used as a grain refiner during solidification through the formation of primary crystals of the equilibrium Al_3Zr phase [43]. The primary (Al_3Zr) crystal has similar lattice parameters and crystal structure to α -Al and can act as effective heterogeneous nuclei for Al and refine the grain size. The mismatch between L1_2 type Al_3Zr and $\alpha(\text{Al})$ is low (about 0.5%), which might increase the nucleating effectiveness [44]. According to the binary phase diagram of the Al-Zr system, the maximum solubility in the aluminum matrix is around 0.27% which is also the peritectic reaction point. However, under non-equilibrium solidification with high cooling rates, the peritectic point shifts towards a higher Zr concentration, allowing more Zr solutes to be dissolved in the aluminum solid, resulting in Zirconium supersaturations [45]. In addition, Zr atoms tend to segregate to cell/dendrite centers, resulting in a concentration gradient between the interdendritic regions and the dendrite centers.

Due to the supersaturation of the matrix with Zr solutes after rapid solidification, the decomposition of the supersaturated solid solution subsequently occurs during heat treatment by the formation of nanosize L1_2 - Al_3Zr dispersoids. However, the driving force for Al_3Zr formation is not the same across the grain due to the uneven distribution of Zr solutes in solid solution resulting from the peritectic reaction during solidification [46]. As a result, there is a higher number density of Al_3Zr dispersoids in the interior of the dendrite/grain than near

the dendrite/grain boundaries, and a particle-free zone often exists adjacent to grain boundaries [47]. In addition, the basic alloying elements can significantly affect the precipitation kinetics of the Al_3Zr phase in multicomponent aluminum alloys. Theoretically, Cu, Mg, and Zn have been predicted to accelerate the Al_3Zr precipitation kinetics compared to those in binary Al-Zr alloys [48].

The precipitation of the dispersoids usually occurs during homogenization treatment. However, the size, density, and spatial distribution of the dispersoids are influenced by the homogenization processing parameters, i.e., the heating rate, soaking temperature, and time. The heating rate affects the morphology and spatial distribution of the dispersoids that are formed during homogenization [49-51]. Also, The size of the Al_3Zr dispersoids depends partially on the heating rate to the homogenization temperature, with slower heating rates apparently leading to a refinement in dispersoid size [45]. The homogenization temperature and soaking time also affect the dispersoid density and size during homogenization [52]. The dispersoid size was found to be generally increased with a higher homogenization temperature and longer soaking time.

As discussed above, the conventional homogenization treatment (single-step) is mainly intended to dissolve low melting eutectic phases and redistribute the solutes in the aluminum matrix, but not necessary to optimize the precipitation of Al_3Zr dispersoids. The high homogenization temperature of the conventional practice causes both high solubility and diffusion rate of zirconium, which results in a low volume fraction of large dispersoids and wide precipitate free zones. To improve the distribution of Al_3Zr dispersoids, some approaches to stepwise homogenization were explored in the literature [53-59]. The first step was used to create a favourable condition of dispersoid precipitation for developing an

optimized distribution. The subsequent step then completed the homogenization of the alloy conventionally.

Zirconium-bearing dispersoids can exist in different crystal structures depending on the heat treatment temperature. At relatively low temperatures (300°C to 450°C), The high-symmetry cubic $L1_2$ - Al_3Zr type with lattice parameter $a=0.4066\text{nm}$ and a 001_{Al} habit plane [60]. It commonly precipitates with spherical morphology and a tiny size ranging from 8nm to 60 nm [58, 61]. Such dispersoids were reported to nucleate homogeneously and exhibit a coherent interface with the matrix due to their very low mismatch with the aluminum matrix. $L1_2$ - Al_3Zr dispersoids are thermodynamically metastable and were observed to eventually transform to the tetragonal structure (DO_{22} or DO_{23}) at higher temperatures (above 500°C). However, the incoherent DO_{23} is the most stable state at high temperatures with an elongated morphology.

In 6xxx alloys, the presence of a considerable amount of Si could influence the nucleation rate of Zr-bearing dispersoids. The Si-vacancy clusters that form by attractive binding energy may act as heterogeneous sites for Zr dispersoids [62]. Silicon was also reported to reduce the peak-aging time of Al_3Zr dispersoids by improving the Zr diffusion kinetics in the Al matrix in the temperature range of 300 to 400 °C [63, 64]. In addition, Si was reported to stabilize DO_{22} - $(Al,Si)_3Zr$ at the expense of the coherent metastable $L1_2$ - Al_3Zr via phase transformation at high-temperature homogenization [60, 64, 65]. The stability of $L1_2$ is negatively affected by the addition of Si by decreasing the stacking fault energy of $L1_2$, which subsequently lowers the barrier for the transformation to DO_{22} . This transformation occurs by substituting Al with a small amount of Si and changing the crystal structure of $L1_2$ to DO_{22} instead of the stable DO_{23} that forms in the absence of Si [60]. While

$L1_2$ - Al_3Zr has spherical morphology with small diameters ranging from 8 to 60 nm, the tetragonal DO_{22} - $(Al,Si)_3Zr$ has a rod-like morphology with a much larger size of around 1.5 μm long and 0.5 μm wide [64, 65].

1.1.6. Effect of Zr dispersoids on recrystallization

The rationale behind adding minor amounts of Zr in wrought aluminum alloys is based on its efficiency for altering the recrystallization via precipitation of coherent high density of the metastable $L1_2$ - Al_3Zr precipitates from supersaturated solid solution. The size, number, density, distribution, and morphology of dispersoids could significantly influence the recrystallization resistance. The dislocation movement and the growth of recrystallized grains can be impeded due to the Zener pinning pressure of the dense Al_3Zr dispersoids [35].

According to the literature, several studies have reported the effect of Zr addition in different aluminum alloys. Guo et al. [7] studied the effects of Al_3Zr dispersoids on recrystallization resistance in 7150 aluminum alloy. After annealing at 470 °C for 24 h, samples with Zr contents from 0 to 0.09% showed partially recrystallized microstructures, and the sample with 0.16% Zr exhibited a recovery microstructure with few, small and isolated recrystallized grains. Li et al. [66] studied the effects of the combined addition of Er and Zr on precipitation and recrystallization of pure aluminum and found that the combined addition of Er and Zr to pure aluminum results in remarkable recrystallization resistance. Regarding 6xxx alloys, Zr has been rarely used alone and combined with other elements (Sc, Mn, Cr). For instance, Meng [65] observed a strong inhibition effect on dynamic recrystallization after adding 0.15wt%Zr into the Al-Mg-Si-Cu-Cr alloy. Also, Birol [3] reported that the combined addition of Zr and Cr positively impacted the recrystallization

resistance of 6082 alloys. Also, better recrystallization resistance was reported in Al-Mg-Si-Sc-Zr alloy than Al-Mg-Si-Mn-Cr [67].

1.2. Definition of the problem

To date, there are discrepancies in the reported effects of Zr containing dispersoids on recrystallization resistance in Al-Mg-Si 6xxx alloys, which could be related to the different dispersoid characteristics in these studies. The effects of the homogenization treatment and the other alloying elements have a direct impact on the precipitation of Zr-bearing dispersoids. Regarding the effect of homogenization treatment, the precipitation behavior of Zr-bearing dispersoids has not been studied systematically under different homogenization conditions in 6xxx alloys. Although a number of studies applied multi-step homogenization to improve the characteristics of Zr-bearing dispersoids in specific aluminium alloy systems, such as 2xxx and 7xxx, there is a lack of research work relating to the use of such an approach in the Al-Mg-Si 6xxx series.

On the other hand, the presence of Si was reported by several studies to play a substantial role in the precipitation behaviour of Zr-bearing dispersoids, which, in turn, can significantly influence the hot deformation and recrystallization resistance. However, there is a lack of literature on how the level Si affects the precipitation of Zr-bearing dispersoids in 6xxx alloys. Given the fact that Si and Mg are the main alloying elements in 6xxx alloys, it would be interesting to investigate the behaviour of Zr-bearing dispersoids in the case of different Si levels and, subsequently, their effects on the hot deformation and recrystallization resistance.

Finally, understanding the nucleation and transformation behaviour of the different types of Zr-bearing dispersoids is essential to achieving the desired dispersoids characteristics. Zr-dispersoids were reported to nucleate homogeneously inside the dendrites in 7xxx alloys.

However, there is a possibility of heterogeneous nucleation in 6xxx alloys assisted by the prior precipitation of Mg-Si particles. Some literature reported that Mg-Si precipitates could act as heterogeneous nucleation sites but for other dispersoids such as α -AlMnSi dispersoids. Also, the transformation mechanism from L1₂ to DO₂₂ dispersoids is still unclear and needs more investigation to understand.

1.3. Objectives

The general objective of this work is to understand the effect of the evolution of Zr-bearing dispersoids on the hot flow stress behavior of 6xxx series aluminum alloys and recrystallization resistance under various homogenization treatments. This main objective has four sub-objectives representing the four parts of the thesis as follows:

1. Part 1: Evolution of Zr-Bearing Dispersoids during Homogenization and their Effects on Hot Deformation and Recrystallization Resistance.

- a. Study the evolution of Zr-bearing dispersoids under various homogenization conditions.
- b. Study the effect of different dispersoid characteristics on the flow stress curves and compare it with the base alloy.
- c. Study microstructural evolution after hot deformation for base alloy and Zr-containing alloy.
- d. Study the recrystallization resistance performance of each dispersoids type after annealing treatment

2. Part 2: Effect of Si Level on the Evolution of Zr-bearing Dispersoids and the Related Hot Deformation and Recrystallization Behaviors.

- a. Study the evolution of Zr-bearing dispersoids under three different Si levels at various homogenization temperatures.
- b. Study the flow stress curves in the studied alloys using various deformation conditions (i.e., strain rate and temperatures).
- c. Study microstructural evolution of studied alloys after hot deformation.

- d. Study the recrystallization resistance after annealing treatment at different annealing temperatures.

3. Part 3: Effect of Two-Step Homogenization on the Evolution of Al₃Zr Dispersoids and recrystallization resistance

- a. Compare the evolution of Zr- bearing dispersoids under single-step and two-step homogenization treatment.
- b. Study the effect of two-step homogenization on the flow stress values.
- c. Study the effect of two-step homogenization on the recrystallization resistance after the annealing treatment.

4. Part 4: The nucleation and transformation of Zr-bearing dispersoids in 6xxx alloys.

- a. Investigate the nucleation of L1₂ Al₃Zr dispersoids.
- b. Investigate the nucleation of DO₂₂-(Al, Si)₃Zr.
- c. Study the transformation of L1₂-Al₃Zr dispersoids to the tetragonal DO₂₂ dispersoids.

1.4. Originality Statement

By adding Zr only to 6xxx alloys, this project was undertaken to understand and maximize the benefits of Zr-bearing dispersoids in 6xxx alloys to inhibit the recrystallization during the hot deformation process and the post-deformation annealing. The following points addressed the subjects in this thesis that have either lack of knowledge in the literature or no systematical studies.

In the first part, various homogenization treatments were performed at different temperatures and soaking times to study and understand the evolution of Zr-bearing dispersoids in Zr-containing 6xxx alloy. This study explained the reason behind the discrepancy in results reported in the literature regarding the effects of Zr in 6xxx alloys, which was attributed to the different pinning effects of different Zr dispersoid types.

In the second part, we added a fixed Zr amount to different 6xxx alloys with various Si levels to study the evolution of Zr-bearing dispersoids in each alloy. To the best of our knowledge, there is a lack of literature on how the Si content affects the precipitation of Zr dispersoids in 6xxx alloys. Three different homogenization temperatures were used to evaluate the precipitation behavior and the hot deformation behavior in each alloy. Increasing the silicon level enhanced the precipitation of Zr-bearing dispersoids and consequently the recrystallization resistance.

In the third part, the low silicon alloys were used to improve their recrystallization resistance by means of a two-step homogenization treatment. Although there are several studies regarding using multi-step treatments in aluminum alloys, there is insufficient literature regarding using this approach in 6xxx, particularly for Zr-containing 6xxx alloys.

The results showed significant improvement in the recrystallization resistance owing to the improved dispersoid distribution after the two-step homogenization treatment.

In the fourth part, the nucleation of spherical $L1_2$ - Al_3Zr dispersoids was investigated during heating and holding at the aging temperature. In addition, the transformation to the elongated DO_{22} was studied at higher aging temperatures. Although there are few reports that studied the nucleation of $L1_2$ dispersoids and their transformation to the equilibrium form DO_{23} in the Al-Zr system, the nucleation mechanism in 6xxx alloys has not been thoroughly studied. In the early stages, the precipitation of $L1_2$ dispersoids showed a preferred orientation that coincides with the typical orientation of Mg-Si precipitates. Subsequently, such dispersoids coarsen and transform to DO_{22} dispersoids by introducing anti-phase boundaries (APBs) in $L1_2$ particles.

1.5. Thesis outlines

The thesis consists of six chapters. In Chapter 1, Introduction, a brief background is presented, which starts with the definition of the 6xxx series alloys and the relevant manufacturing process steps. Then, the hot deformation behavior was discussed, along with the softening mechanisms that commonly occur during and after the thermomechanical process. In addition, the microalloying of Zirconium as a recrystallization inhibitor was discussed according to the relevant literature.

In Chapter 2, the published paper “Evolution of Zr-Bearing Dispersoids during Homogenization and their Effects on Hot Deformation and Recrystallization Resistance in Al-0.8%Mg-1.0%Si Alloy” in the *Journal of Material Engineering and Performance*, 2021 is presented. The paper is drawn from the experimental results, discussing the effect of the addition of Zr and homogenization treatment on the evolution of different types of Zr-bearing dispersoids in Al-Mg-Si alloy. In addition, the recrystallization resistance of each dispersoids type was discussed.

In Chapter 3, the published paper “Effect of Si Level on the Evolution of Zr-bearing Dispersoids and the Related Hot Deformation and Recrystallization Behaviors in Al-Si-Mg 6xxx Alloy” in the journal of *Advanced Engineering Materials*, 2022 is presented. In this paper, different 6xxx alloys with different Si levels were used to study the effect of Si content on the evolution of different types of Zr dispersoids after different homogenization treatments. Accordingly, the different hot deformation behaviours and recrystallization resistance related to different alloys were studied.

In Chapter 4, the paper entitled “Improving the dispersoid distribution and recrystallization resistance of a Zr-containing 6xxx alloy using two-step homogenization” is published in the *Philosophical Magazine*, 2022. The results of this paper were obtained from the third part of the Ph.D. project. In this study, a two-step homogenization approach was used to improve the distribution of the Zr-bearing dispersoids. The first step was used to promote the nucleation of the dispersoids. While the second step aimed to fulfill the industrial requirements. The recrystallization behavior was evaluated using Grain Orientation Spread (GOS) maps after single-step and two-step homogenization treatments.

In Chapter 5, The manuscript entitled “On the Nucleation and Transformation of Zr-bearing dispersoids in Al-Mg-Si 6xxx alloy” is presented. Using transmission electron microscopy (TEM), the nucleation of different Zr-bearing dispersoids ($L1_2$ and DO_{22}) was studied using one-step and two-step heat treatment. The schematic drawing in this paper illustrated the different stages of the evolution of such dispersoids. In addition, the transformation mechanism from $L1_2$ -type to DO_{22} -type was discussed.

Finally, in Chapter 6, the general conclusions and recommendations for future work are presented. Following this chapter, a list of publications, posters and awards has been presented.

References

1. HIRSCH, J., *Recent development in aluminium for automotive applications*, in *Transactions of Nonferrous Metals Society of China*. 2014. p. 1995-2002.
2. Cai, M. and G.J. Cheng, *Microstructure-properties relationship in two Al-Mg-Si alloys through a combination of extrusion and aging*. *Jom*, 2007. **59**(8): p. 58-61.
3. Birol, Y., *Effect of Cr and Zr on the grain structure of extruded EN AW 6082 alloy*. *Metals and Materials International*, 2016. **20**(4): p. 727-732.
4. Poletti, C., T. Wójcik, and C. Sommitsch, *Hot Deformation of AA6082 Containing Fine Intermetallic Particles*. *Metallurgical and Materials Transactions A: Physical Metallurgy and Materials Science*, 2012. **44**(3): p. 1577-1586.
5. Li, C., K. Liu, and Chen, X.G, *Improvement of elevated-temperature strength and recrystallization resistance via Mn-containing dispersoid strengthening in Al-Mg-Si 6082 alloys*. *Journal of Materials Science & Technology*, 2020. **39**: p. 135-143.
6. Zhang, G.W., et al., *Effects of Mn and Cr Additions on the Recrystallization Behavior of Al-Mg-Si-Cu Alloys*. *Materials Science Forum*, 2017. **877**: p. 172-179.
7. Guo, Z., G. Zhao, and Chen, X.G, *Effects of two-step homogenization on precipitation behavior of Al₃Zr dispersoids and recrystallization resistance in 7150 aluminum alloy*. *Materials Characterization*, 2015. **102**: p. 122-130.
8. Ding, Y., et al., *The recrystallization behavior of Al-6Mg-0.4Mn-0.15Zr-xSc (x = 0.04–0.10 wt%) alloys*. *Materials Characterization*, 2019. **147**: p. 262-270.
9. Knipling, K.E., D.C. Dunand, and D.N. Seidman, *Precipitation evolution in Al–Zr and Al–Zr–Ti alloys during aging at 450–600°C*. *Acta Materialia*, 2008. **56**(6): p. 1182-1195.

10. Deng, Y.-l., et al., *Three-Stage Homogenization of Al-Zn-Mg-Cu Alloys Containing Trace Zr*. Metallurgical and Materials Transactions A: Physical Metallurgy and Materials Science, 2013. **44**(6): p. 2470-2477.
11. Guo, Z., G. Zhao, and Chen, X-G, *Effects of homogenization treatment on recrystallization behavior of 7150 aluminum sheet during post-rolling annealing*. Materials Characterization, 2016. **114**: p. 79-87.
12. Humphreys, F.J. and M. Hatherly, *Recrystallization and related annealing phenomena*. 2012: Elsevier.
13. Andersen, S.J., *Quantification of the Mg₂Si β'' and β' phases in AlMgSi alloys by transmission electron microscopy*. Metallurgical and Materials Transactions A, 1995. **26**(8): p. 1931-1937.
14. Ding, L., et al., *The structural and compositional evolution of precipitates in Al-Mg-Si-Cu alloy*. Acta Materialia, 2018. **145**: p. 437-450.
15. Qian, X., *Hot deformation behavior of 6xxx aluminum alloys*. 2019, Université du Québec à Chicoutimi.
16. Birol, Y., *Precipitation during homogenization cooling in AlMgSi alloys*. Transactions of Nonferrous Metals Society of China, 2013. **23**(7): p. 1875-1881.
17. Mukhopadhyay, P., *Alloy Designation, Processing, and Use of AA6XXX Series Aluminium Alloys*. ISRN Metallurgy, 2012. **2012**: p. 1-15.
18. Li, J., et al., *Intermetallic phase selection during homogenization for AA6082 alloy*. Philosophical Magazine, 2014. **94**(8): p. 830-846.
19. Qi, Y. and R.K. Mishra, *Ab initio study of the effect of solute atoms on the stacking fault energy in aluminum*. Physical Review B, 2007. **75**(22).

20. Li, C., K. Liu, and Chen, X.G, *Improvement of elevated-temperature strength and recrystallization resistance via Mn-containing dispersoid strengthening in Al-Mg-Si 6082 alloys*. Journal of Materials Science & Technology, 2020. **39**: p. 135-143.
21. Boulger, F.W. and T. Altan, *Flow Stress of Metals and Its Application in Metal Forming Analyses*. Journal of Engineering for Industry, 1973. **95**(4): p. 1009-1019.
22. Chamanfar, A., et al., *Analysis of flow stress and microstructure during hot compression of 6099 aluminum alloy (AA6099)*. Materials Science and Engineering A, 2019. **743**: p. 684-696.
23. Liu, S., et al., *Characterization of hot deformation behavior and constitutive modeling of Al-Mg-Si-Mn-Cr alloy*. Materials Science, 2019. **54**(5): p. 4366-4383.
24. McQueen, H.J., et al., *Hot Deformation and Processing of Aluminum Alloys*. 2016: CRC Press. 1-564.
25. Alaneme, K.K. and E.A. Okotete, *Recrystallization mechanisms and microstructure development in emerging metallic materials: A review*. Journal of Science: Advanced Materials and Devices, 2019. **4**(1): p. 19-33.
26. Liu, J., et al., *Effect of minor Sc and Zr on recrystallization behavior and mechanical properties of novel Al-Zn-Mg-Cu alloys*. Journal of Alloys and Compounds, 2016. **657**: p. 717-725.
27. Shi, Y., et al., *Effect of Sc and Zr additions on corrosion behaviour of Al-Zn-Mg-Cu alloys*. Journal of Alloys and Compounds, 2014. **612**: p. 42-50.
28. Chen, K., et al., *Effect of Yb, Cr and Zr additions on recrystallization and corrosion resistance of Al-Zn-Mg-Cu alloys*. Materials Science and Engineering: A, 2008. **497**(1-2): p. 426-431.
29. Birol, Y., *Impact of partial recrystallization on the performance of 6005A tube extrusions*. Engineering Failure Analysis, 2010. **17**(5): p. 1110-1116.

30. Morere, B., et al., *Microstructural effects on fracture toughness in AA7010 plate*. Metallurgical and Materials Transactions A, 2000. **31**(10): p. 2503-2515.
31. Hillert, M., *Inhibition of grain growth by second-phase particles*. Acta Metallurgica, 1988. **36**(12): p. 3177-3181.
32. Hellman, P., *On the effect of second-phase particles on grain growth*. Scand. Jour. Metall., 1975. **4**: p. 211-219.
33. Li, W.B. and K.E. Easterling, *The influence of particle shape on zener drag*. Acta Metallurgica et Materialia, 1990. **38**(6): p. 1045-1052.
34. Du, L., et al., *Pinning effect of different shape second-phase particles on grain growth in polycrystalline: numerical and analytical investigations*. Composite Interfaces, 2018. **25**(4): p. 357-368.
35. Nes, E., N. Ryum, and O. Hunderi, *On the Zener drag*. Acta Metallurgica, 1985. **33**(1): p. 11-22.
36. Hazzledine, P., *Grain boundary pinning in two-phase materials*. Czechoslovak Journal of Physics B, 1988. **38**(4): p. 431-443.
37. Wu, L.-M., et al., *Effects of homogenization treatment on recrystallization behavior and dispersoid distribution in an Al-Zn-Mg-Sc-Zr alloy*. Journal of Alloys and Compounds, 2008. **456**(1): p. 163-169.
38. Tangen, S., et al., *Effect of concurrent precipitation on recrystallization and evolution of the P-texture component in a commercial Al-Mn alloy*. Metallurgical and Materials Transactions A, 2010. **41**(11): p. 2970-2983.
39. Lillywhite, S.J., P.B. Prangnell, and F.J. Humphreys, *Interactions between precipitation and recrystallisation in an Al-Mg-Si alloy*. Materials Science and Technology, 2013. **16**(10): p. 1112-1120.

40. Kaibyshev, R., et al., *Grain refinement and superplastic behaviour of a modified 6061 aluminium alloy*. Materials Science and Technology, 2013. **19**(4): p. 483-490.
41. Robson, J.D., *A new model for prediction of dispersoid precipitation in aluminium alloys containing zirconium and scandium*. Acta Materialia, 2004. **52**(6): p. 1409-1421.
42. Hirosawa, S., et al., *Classification of the role of microalloying elements in phase decomposition of Al based alloys*. Acta Materialia, 2000. **48**(8): p. 1797-1806.
43. Kahrman, F. and M. Zeren, *Mechanical and Fractographical Characterization of Extruded Al-Mg-Si-Zr Alloys*, in *MATEC Web of Conferences*, S. Pantelakis and S. Koubias, Editors. 2018. p. 02017.
44. Dang, J.-z., Y.-f. Huang, and J. Cheng, *Effect of Sc and Zr on microstructures and mechanical properties of as-cast Al-Mg-Si-Mn alloys*. Transactions of Nonferrous Metals Society of China, 2009. **19**(3): p. 540-544.
45. Robson, J.D. and P.B. Prangnell, *Dispersoid precipitation and process modelling in zirconium containing commercial aluminium alloys*. Acta Materialia, 2001. **49**(4): p. 599-613.
46. Knipling, K.E., D.C. Dunand, and D.N. Seidman, *Precipitation evolution in Al-Zr and Al-Zr-Ti alloys during isothermal aging at 375–425 C*. Acta Materialia, 2008. **56**(1): p. 114-127.
47. Liu, S., et al., *Effects of Combined Additions of Mn and Zr on Dispersoid Formation and Recrystallization Behavior in Al-Zn-Mg Alloys*. Metallurgical and Materials Transactions A, 2019. **50**(10): p. 4877-4890.
48. Robson, J.D. and P.B. Prangnell, *Modelling Al₃Zr dispersoid precipitation in multicomponent aluminium alloys*. Materials Science and Engineering: A, 2003. **352**(1-2): p. 240-250.

49. Lodgaard, L. and N. Ryum. *Distribution of Mn-and Cr-containing dispersoids in Al-Mg-Si-alloys*. in *Materials science forum*. 2000. Trans Tech Publ.
50. Hu, R., et al., *Dispersoid Formation and Recrystallization Behavior in an Al-Mg-Si-Mn Alloy*. *Journal of Materials Science & Technology*, 2010. **26**(3): p. 237-243.
51. Remøe, M.S., et al. *The Effect of Heating Rate on the Density and Spatial Distribution of Dispersoids during Homogenisation of 6xxx Aluminium Alloys*. in *Materials Science Forum*. 2017. Trans Tech Publ.
52. Rometsch, P., et al. *The effect of homogenizing on the quench sensitivity of 6082*. in *Materials Science Forum*. 2002. Trans Tech Publ.
53. Robson, J.D., *Optimizing the homogenization of zirconium containing commercial aluminium alloys using a novel process model*. *Materials Science and Engineering: A*, 2002. **338**(1-2): p. 219-229.
54. Jia, Z., et al., *Enhancement of recrystallization resistance of Al-Zr-Mn by two-step precipitation annealing*. *Materials Science and Engineering A*, 2008. **483-484**: p. 195-198.
55. Mochugovskiy, A.G., et al., *The mechanism of L12 phase precipitation, microstructure and tensile properties of Al-Mg-Er-Zr alloy*. *Materials Science and Engineering: A*, 2019. **744**: p. 195-205.
56. Mikhaylovskaya, A.V., et al., *Precipitation behavior of L12 Al₃Zr phase in Al-Mg-Zr alloy*. *Materials Characterization*, 2018. **139**: p. 30-37.
57. Xiao, T., et al., *Effect of three-stage homogenization on mechanical properties and stress corrosion cracking of Al-Zn-Mg-Zr alloys*. *Materials Science and Engineering: A*, 2016. **675**: p. 280-288.
58. Mousavi Anijdan, S.H., et al., *Precipitation behavior of strip cast Al-Mg-0.4Sc-0.15Zr alloy under single and multiple-stage aging processes*. *Materials Science and Engineering: A*, 2015. **640**: p. 275-279.

59. Deng, Y., et al., *Effect of double-step homogenization treatments on the microstructure and mechanical properties of Al–Cu–Li–Zr alloy*. Materials Science and Engineering: A, 2020. **795**.
60. Litynska, L., et al., *TEM and HREM study of Al₃Zr precipitates in an Al-Mg-Si-Zr alloy*. J Microsc, 2006. **223**(Pt 3): p. 182-4.
61. LÜ, X.-y., et al., *Effect of one-step and two-step homogenization treatments on distribution of Al₃Zr dispersoids in commercial AA7150 aluminium alloy*. Transactions of Nonferrous Metals Society of China, 2012. **22**(11): p. 2645-2651.
62. Wolverton, C., *Solute–vacancy binding in aluminum*. Acta Materialia, 2007. **55**(17): p. 5867-5872.
63. Vo, N.Q., D.C. Dunand, and D.N. Seidman, *Role of silicon in the precipitation kinetics of dilute Al-Sc-Er-Zr alloys*. Materials Science and Engineering A, 2016. **677**: p. 485-495.
64. Gao, T., et al., *Precipitation behaviors of cubic and tetragonal Zr-rich phase in Al-(Si-)Zr alloys*. Journal of Alloys and Compounds, 2016. **674**: p. 125-130.
65. Meng, Y., et al., *Effect of Zr on microstructures and mechanical properties of an AlMgSiCuCr alloy prepared by low frequency electromagnetic casting*. Materials Characterization, 2014. **92**: p. 138-148.
66. Li, H., et al., *Effects of Er and Zr additions on precipitation and recrystallization of pure aluminum*. Scripta Materialia, 2013. **68**(1): p. 59-62.
67. Babaniaris, S., et al., *Effect of Al₃(Sc,Zr) dispersoids on the hot deformation behaviour of 6xxx-series alloys: A physically based constitutive model*. Materials Science and Engineering A, 2020. **793**.

CHAPTER 2: Evolution of Zr-Bearing Dispersoids During Homogenization and Their Effects on Hot Deformation and Recrystallization Resistance in Al-0.8%Mg-1.0%Si Alloy

(Published in the Journal of Materials Engineering and Performance)

Abstract

The precipitation behavior of Zr-bearing dispersoids in an Al-0.8%Mg-1.0%Si alloy was investigated for different homogenization treatments (450-550 °C). The effect on the recrystallization resistance of the alloy was also studied during post-deformation annealing. With an addition of 0.2 wt.% Zr, two different Zr-bearing dispersoids were observed depending on the homogenization conditions. Homogenization at 450 °C for 2 h resulted in the precipitation of fine and dense $L1_2$ - Al_3Zr dispersoids (8-10 nm), which were found to be coherent with the matrix. In contrast, extended homogenization times, such as 12 h at 450 °C, or increasing the homogenization temperature to 500-550 °C produced elongated DO_{22} - $(Al,Si)_3Zr$ dispersoids with a larger size. During hot compression testing, the addition of 0.2 wt.% Zr combined with homogenization at 450 °C increased the high-temperature flow stress by 20% relative to the base alloy free of Zr, revealing their potential to inhibit dislocation motion and dynamic recovery. Both dispersoids were found to have a positive impact on the retardation of recrystallization during post-deformation annealing, but the fine and coherent Al_3Zr dispersoids were more effective than the coarse and incoherent $(Al,Si)_3Zr$ dispersoids.

Keywords: Zr dispersoids; Al-Mg-Si alloys, homogenization; hot deformation; recrystallization.

2.1. Introduction

The trend to reduce vehicle fuel emissions continues to offset the effect on global warming. As a result, the industrial demand to develop light, fuel-efficient automobiles has increased rapidly. Because of their high strength-to-weight ratio, good weldability, inherent corrosion resistance, and suitability for different product forms, including extrusions, Al-Mg-Si 6xxx aluminum alloys are excellent candidates for manufacturing automotive parts, such as front rails, bumpers, and structural body components [1]. During the manufacturing process of such products, 6xxx alloys can undergo hot deformation processes such as extrusion and rolling. The hot workability of a particular alloy has a direct impact on the production cost. In addition, the thermomechanical process itself can influence the material's properties, including strength and ductility [2], and control of grain structure and recrystallization during hot deformation and subsequent heat treatment is of particular importance. Alloying using transition elements is an effective technique [3-5] to achieve this goal through the formation of small and dense dispersoids, which induce a pinning effect on high and low angle grain boundaries. Dispersoids can also prevent slip localization in precipitation hardened materials which is important for ductility critical applications such as crash systems. As a result, the correct distribution of such particles can inhibit recrystallization and improve mechanical properties [5, 6]. Dispersoids are relatively stable at high temperatures, having slow coarsening kinetics, and can therefore pin the grain boundaries and dislocations effectively during hot deformation. The desired dispersoid characteristics, e.g., size, distribution and number density, can be achieved by optimizing the homogenization treatment and the alloy chemistry [7, 8].

Zirconium is widely used as a microalloying element added to Al-Zn-Mg 7xxx aluminum alloys to form fine and thermally stable dispersoids due to its low diffusion rate [8-10]. Fine and coherent L_{12} - Al_3Zr dispersoids can precipitate during annealing or homogenization as a consequence of the supersaturation of Zr in the α -Al during solidification [7, 11]. Cubic L_{12} -structured Al_3Zr dispersoids form principally in the grain interior during homogenization at relatively low temperatures. It is reported that these dispersoids transform to an undesirable equilibrium tetragonal DO_{23} - Al_3Zr phase during prolonged heat treatments at high temperatures [5, 7, 12]. By using high-resolution transmission electron microscopy (HRTEM), some planar faults were observed inside L_{12} - Al_3Zr , indicative of the early stage of transformation from a cubic to tetragonal structure after high-temperature treatment [13]. Moreover, Himuro [14] suggested that this transformation occurred as a result of the interactions of coherent dispersoids with migrating grain boundaries during recrystallization. However, in 6xxx alloys, the presence of Si can influence the Zr dispersoid phase-type by forming a different phase at high temperatures. It has been reported that Si tends to stabilize DO_{22} - $(Al,Si)_3Zr$ instead of DO_{23} - Al_3Zr through the substitution of Si for Al in the metastable Al_3Zr phase [12, 13, 15]. In addition, Si was found to increase the nucleation rate of dispersoids by reducing the volume of free energy for dispersoid formation [5].

Thermomechanical processes such as extrusion and rolling are commonly used to get the desired product form, i.e., extruded profiles and sheets. Post-deformation heat treatments such as annealing or solutionizing followed by aging are sometimes performed to achieve the desired mechanical properties. However, static recovery (SRV) and static recrystallization (SRX) occur during post-deformation annealing because of the high strain energy and the high density of substructures [16]. For many applications, the retention of a

non-recrystallized structure is preferred for improving mechanical properties and corrosion resistance [8, 17, 18]. Thermally stable Zr dispersoids have been shown to have a significant impact on retarding dislocation movements and inhibiting recrystallization in aluminum alloys [8, 17, 19-21]. Regarding 6xxx alloys, Hichem *et al.* [5] reported that the precipitation of Al₃Zr before the deformation of Al-Mg-Si alloys effectively inhibited recrystallization. On the other hand, Meng [22] and Zou *et al.* [23] reported a reduced inhibition effect of Al₃Zr precipitates in 6xxx alloys compared to Al₃Sc and Al₃(Zr,Sc). Birol [24] found that the combined addition of Cr and Zr had a favorable impact on the recrystallization resistance in AA6082.

To date, there are discrepancies in the reported effects of Zr containing dispersoids on recrystallization resistance in Al-Mg-Si 6xxx alloys. Furthermore, the precipitation behavior of different types of Zr dispersoids has not been studied systematically. The present work was therefore undertaken to study the precipitation behavior of Zr dispersoids during homogenization and their effects on the recrystallization resistance in an Al-0.8%Mg-1.0%Si alloy. Different homogenization treatments were conducted at 450, 500, and 550 °C for 2 and 12 h. The microstructure evolution was characterized with optical microscopy and scanning electron microscopy. The hot deformation behavior of the alloys was evaluated by hot compression testing. The recrystallization resistance during post-deformation annealing was assessed using electron backscatter diffraction (EBSD) analysis.

2.2. Experimental work

Two Al-0.8%Mg-1.0%Si alloys were prepared and referred to as “base” and “0.2Zr” alloys. The chemical compositions analyzed using an optical emission spectrometer are listed in Table 2.1. The alloys were prepared using pure Al (99.7 wt.%), pure Mg (99.8

wt.%) and Al-50 wt.% Si, Al-25 wt.% Fe, and Al-15 wt.% Zr master alloys. The materials were melted using an electrical resistance furnace and cast into a permanent steel mold preheated to 250 °C to obtain rectangular ingots with dimensions of 30 mm × 40 mm × 80 mm. Different homogenization treatments were conducted on cast ingots at 450, 500 and 550 °C for 2 and 12 h with a heating rate of 100 °C/h followed by water quenching to room temperature.

Table 2.1 Chemical composition (wt.%) of the experimental alloys

Alloy	Mg	Si	Fe	Zr	Ti	Al
Base	0.81	1.05	0.18	---	0.15	Bal.
0.2Zr	0.83	1.01	0.20	0.193	0.11	Bal.

Uniaxial hot compression tests were performed on a Gleeble 3800 thermomechanical simulator using cylindrical samples with a diameter of 10 mm and length of 15 mm. The compression tests involved heating the samples up to the deformation temperature (400 °C) with a heating rate of 2 °C/s and then holding for 3 minutes to ensure a uniform temperature. The samples were deformed to a true strain of 0.8 with a strain rate of 1.0 s⁻¹ followed by water quenching to retain the deformed microstructure. Graphite foils were inserted between the cylindrical samples and the anvils to minimize the friction occurring during the deformation. To study the recrystallization resistance, a post-deformation anneal was performed at 500 °C for 4 h for selected homogenization conditions.

To reveal the microstructural features, the homogenized samples were polished using standard metallographic methods. The intermetallic phases and dispersoids were observed using optical microscopy (Nikon, Eclipse ME600) and scanning electron microscopy (SEM, JEOL-6480LV) after etching by 0.5% HF for 30 seconds. A transmission electron

microscope (TEM, JEM–2100) operated at 200 kV was used to resolve the Zr dispersoids. The TEM samples were ground and electropolished using a twin-jet electropolisher operated at 15 V and -20 °C with 30 vol.% nitric acid and 70 vol.% methanol. The samples were observed in both dark and bright field modes near the [001] zone axis to reveal different types of Zr dispersoids. The average dispersoid size and number density were calculated based on a quantitative analysis of TEM images. The TEM foil thickness was measured by the convergent electron beam diffraction (CBED) method [25].

The microstructures after deformation and annealing were characterized using EBSD analysis. The EBSD samples were sectioned parallel to the deformation axis along the centerline direction and then mounted and mechanically ground using SiC papers. The polishing was subsequently carried out using 6 μm , 3 μm diamond suspension, followed by final polishing using 0.5 μm colloidal silica suspension to achieve high indexing quality. The central region of the samples was examined for the selected conditions. All-Euler orientation maps were used with a step size of 1 μm for grain structure and 0.5 μm for the quantitative measurement of the misorientation distribution of boundaries. The low angle boundaries (2-5°), medium angle boundaries (5-15°), and high angle boundaries (>15°) were presented by white, green, and black lines, respectively. To exclude the microstructure noise caused by sample preparation, misorientation angles below 2° were not considered.

2.3. Results and Discussion

2.3.1. As cast and homogenized microstructures

Figure 2.1 shows backscattered SEM images of the as-cast microstructures for the base and 0.2Zr materials. The microstructures of both alloys were mainly composed of α -Al with

intermetallic phases distributed along interdendrite boundaries. Based on their morphologies and SEM-EDS analysis, these were identified as β -AlFeSi and primary Mg_2Si , appearing bright and dark, respectively (Fig. 2.1a and b). When comparing the grain structure (EBSD images, Fig. 2.1c and d), the base alloy exhibited a coarser grain structure with an average grain size of $211\pm 61\ \mu\text{m}$, while the 0.2Zr alloy possessed a more uniform grain structure with an average grain size of $133\pm 32\ \mu\text{m}$. The fine grain structure of the 0.2Zr alloy could be attributed to the primary crystals of Al_3Zr acting as nucleation sites for α -Al during solidification [26, 27]. The inset of Fig. 2.1b shows one of fine Al_3Zr primary particles formed in 0.2Zr alloy.

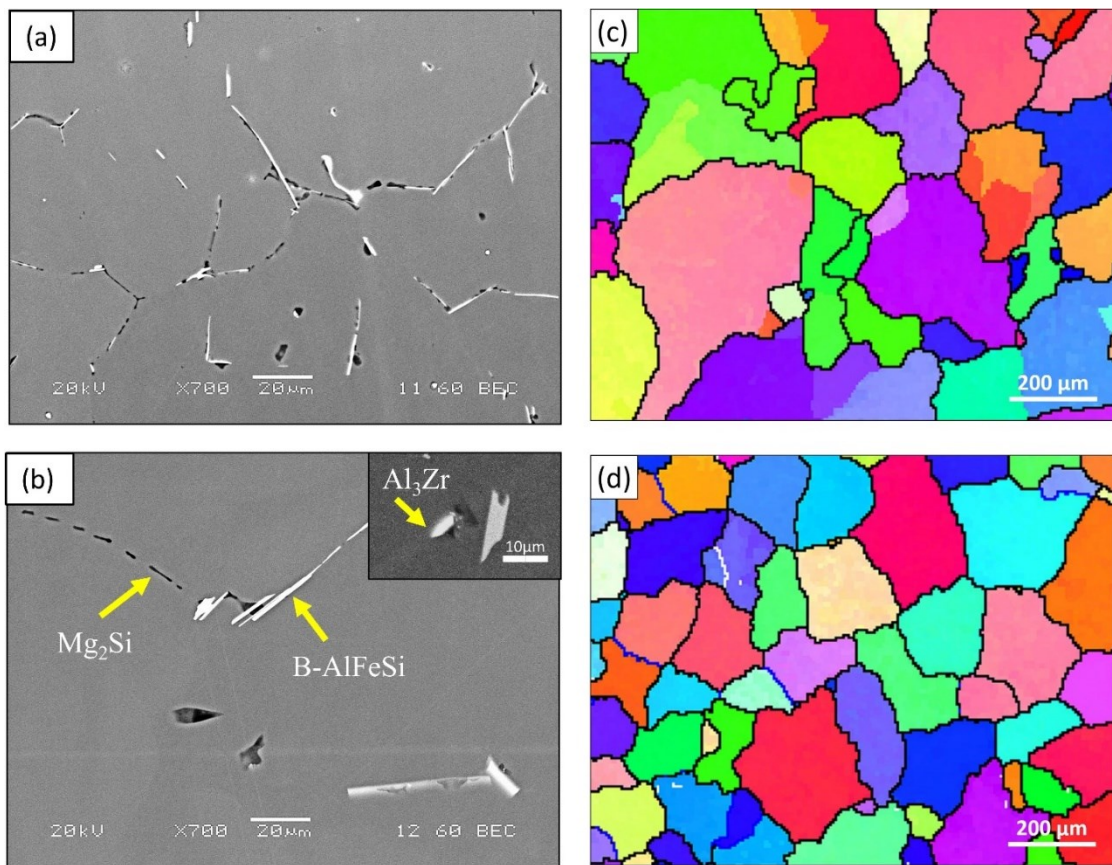


Figure 2.1 SEM images of as-cast microstructure and EBSD images of grain distribution for the base (a,c) and 0.2Zr (b,d) alloys.

Figure 2.2 shows the optical microstructures of the base alloy for different homogenization conditions. After homogenizing at 450 °C for 2 h (Fig. 2.2a), a significant amount of β -Mg₂Si (indicated by arrows) was precipitated out of the matrix in areas adjacent to the β -AlFeSi and the primary Mg₂Si phases. Such areas were enriched with high supersaturation levels of Mg and Si during solidification due to the high segregation tendency of these elements towards the grain boundaries and interdendritic regions [28]. Extending the homogenization time to 12 h at 450 °C promoted further precipitation of β -Mg₂Si, as shown in Fig. 2.2b. A reduced amount of β -Mg₂Si precipitate was observed when the temperature was increased to 500 °C compared to 450 °C for soak times up to 12 h, as shown in Figs. 2.2c and d. However, the primary Mg₂Si phase from the original cast structure was almost unaffected by increasing the homogenization temperature to 500 °C. Based on equilibrium calculations on the experimental compositions using ThermoCalc, a relatively high temperature of 560 °C was found to be required to dissolve the primary Mg₂Si phase in this alloy. Therefore, homogenizing at a temperature close to this temperature, namely at 550 °C, suppressed the precipitation of β -Mg₂Si precipitates and significantly dissolved the primary Mg₂Si phase into the α -Al matrix, as shown in Figs. 2.2e and f.

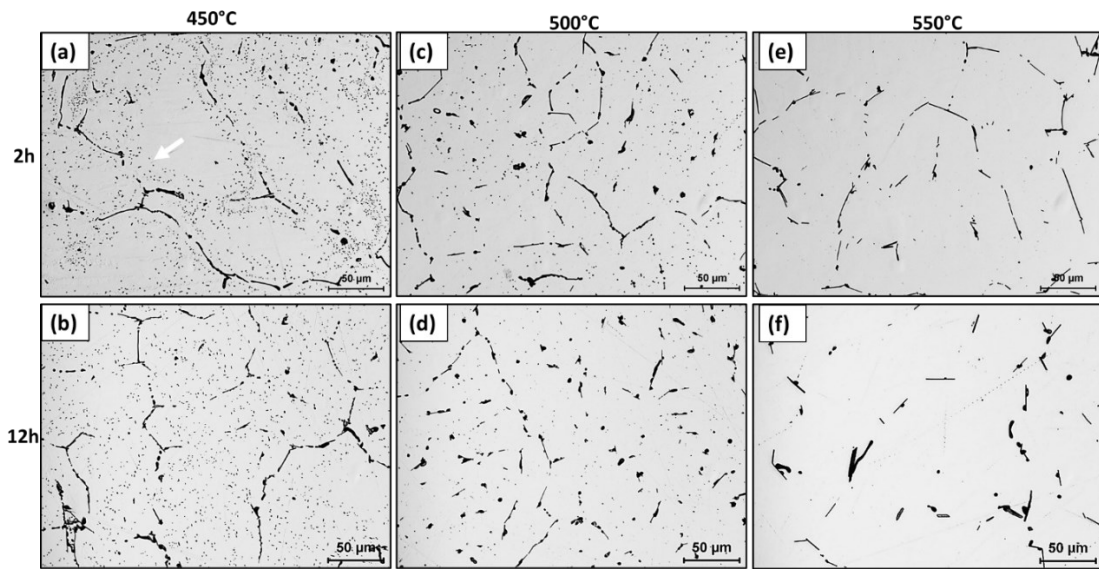


Figure 2.2 Optical micrographs showing the base alloy microstructure for different homogenization conditions.

In the case of the 0.2Zr alloy (Fig. 2.3), a generally higher amount of β -Mg₂Si precipitate was observed compared to the base alloy (Fig. 2.2). This can be related to the smaller grain size and consequently the larger total grain boundary area of the 0.2Zr alloy, where the segregation of Mg and Si typically occurs. Similar to the base alloy, the precipitation of β -Mg₂Si in the 0.2Zr alloy only occurred at 450 °C and 500 °C with a reduced amount at 500 °C. The most outstanding feature of the homogenized microstructure of the 0.2Zr alloy was the presence of a large amount of Zr-bearing dispersoids which were mainly precipitated at the dendrite centre at 500 °C (Fig. 2.3c and d) and 550 °C (Fig. 2.3e and f). In addition, much smaller dispersoids precipitated at 450 °C (Fig. 2.4a) that could not be observed by the optical microscope. The dispersoids were distinguished from the β -Mg₂Si precipitates based on the morphology and size using SEM, where the former (black arrow) were globular and much smaller in size, and the latter (white arrow) exhibited a needle-like morphology with a

larger size. It is worth noting that the amount and size of the dispersoids depended mainly on the homogenization condition as shown by SEM images in Fig. 2.4 and TEM images in Fig. 2.5.

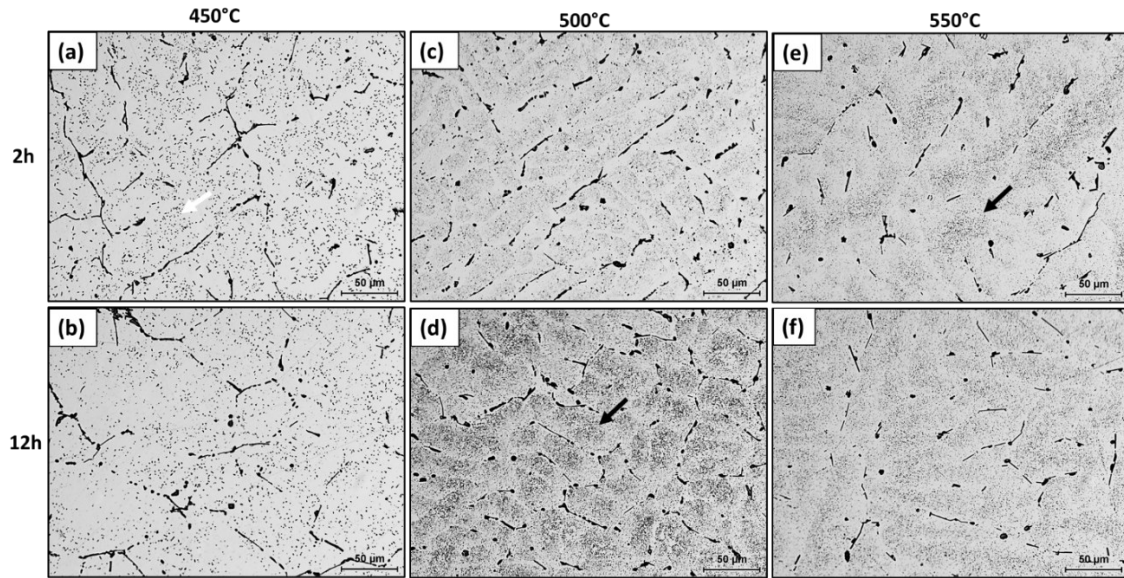


Figure 2.3 Optical micrographs showing the 0.2Zr alloy microstructure of for different homogenization conditions. The black arrows in (d) and (e) indicate dispersoid zones (DZs).

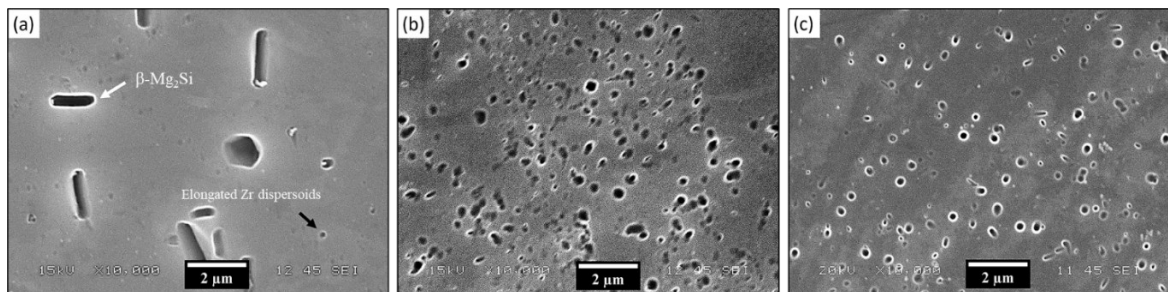


Figure 2.4 SEM images showing the Zr bearing dispersoids in the 0.2Zr alloy after homogenization at 450 °C (a), 500 °C (b), and 550 °C (c) for 12 h soaking time.

3.3.2. Evolution of Zr-bearing dispersoids

The evolution of the Zr-bearing dispersoids in the 0.2Zr alloy during homogenization was studied using TEM. Figures 2.5a-f show bright-field TEM images for the range of homogenization conditions investigated, where precipitation of two types of Zr-bearing dispersoids was observed. Homogenization at 450 °C for 2 h (Fig. 2.5a) resulted in the precipitation of nano-sized spherical Zr-dispersoids with a relatively high density. These were not detected with OM and SEM observations due to their small size which ranged between 8 and 10 nm. It is well known that at relatively low temperatures, the driving force for the precipitation of Zr dispersoids is higher due to the high level of Zr supersaturation in the matrix [27]. This supersaturation leads to the precipitation of nano-sized dispersoids with a homogeneous distribution.

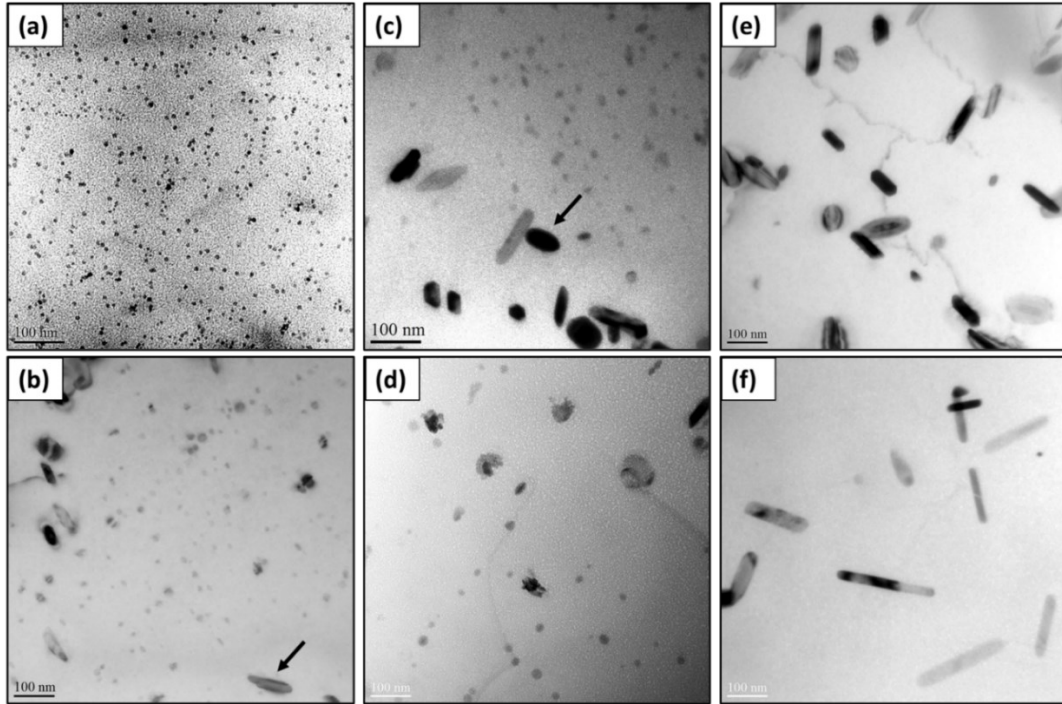


Figure 2.5 Bright field TEM images of 0.2Zr alloy for different homogenization conditions: (a,b) 450 °C for 2 and 12 h, (c,d) 500 °C for 2 and 12 h, and (e,f) 550 °C for 2 and 12 h.

When the holding time at 450 °C was increased to 12h (Fig. 2.5b), the density of the spherical dispersoids decreased and few elongated dispersoids (black arrows) were formed. Increasing the homogenization temperature to 500 °C (Figs. 2.5c and d), promoted the formation of the elongated dispersoids at the expense of the spherical dispersoids; the former were found to form after only 2 h, *i.e.*, more rapidly than they did at 450 °C. When the homogenization temperature was further increased to 550 °C (Figs. 2.5e and f), very few spherical dispersoids were present for both holding times, while the elongated dispersoids became dominant, displaying a lower density with a coarser morphology after 12 h compared with 2 h.

To better characterize both Zr-bearing dispersoid types, the dark field TEM imaging mode was used and selected area electron diffraction patterns (SAEDPs) were recorded together with TEM-EDS analysis. The fine spherical dispersoids formed after homogenization at 450 °C for 2 h can be clearly seen in Fig. 2.6a. The corresponding SAEDP shown in Fig. 2.6b was obtained at the $[001]_{\alpha}$ zone axis and revealed faint spots from the dispersoids between the strong spots of the α -Al. The orientation relationship between the dispersoids and α -Al was observed to be $([100] \text{ Al} // [100] \text{ dispersoid})$, indicating that these dispersoids were $L1_2\text{-Al}_3\text{Zr}$ [13, 29]. It was reported that due to the similarity of the lattice parameters between the aluminum matrix and $L1_2\text{-Al}_3\text{Zr}$ dispersoids, the interface with the matrix was coherent with a slight mismatch [7]. The higher magnification bright field TEM image shown in Fig. 2.6c displays typical coarse elongated Zr-bearing dispersoids formed after homogenization at 550 °C for 12 h. These were identified as $\text{DO}_{22}\text{-(Al,Si)}_3\text{Zr}$ according to their SAEDP (Fig. 2.6d), which are most likely incoherent or semi-coherent to the matrix [30]. This was also confirmed by TEM-EDS analysis, which revealed that they contained a considerable amount of Si besides Al and Zr, as shown in Fig. 2.6e. It was reported [13, 14, 30] that the $\text{DO}_{22}\text{-(Al,Si)}_3\text{Zr}$ phase can transform from the metastable $L1_2\text{-Al}_3\text{Zr}$ phase in the presence of Si, which substitutes for Al, increasing the stability of the $\text{DO}_{22}\text{-(Al,Si)}_3\text{Zr}$ phase.

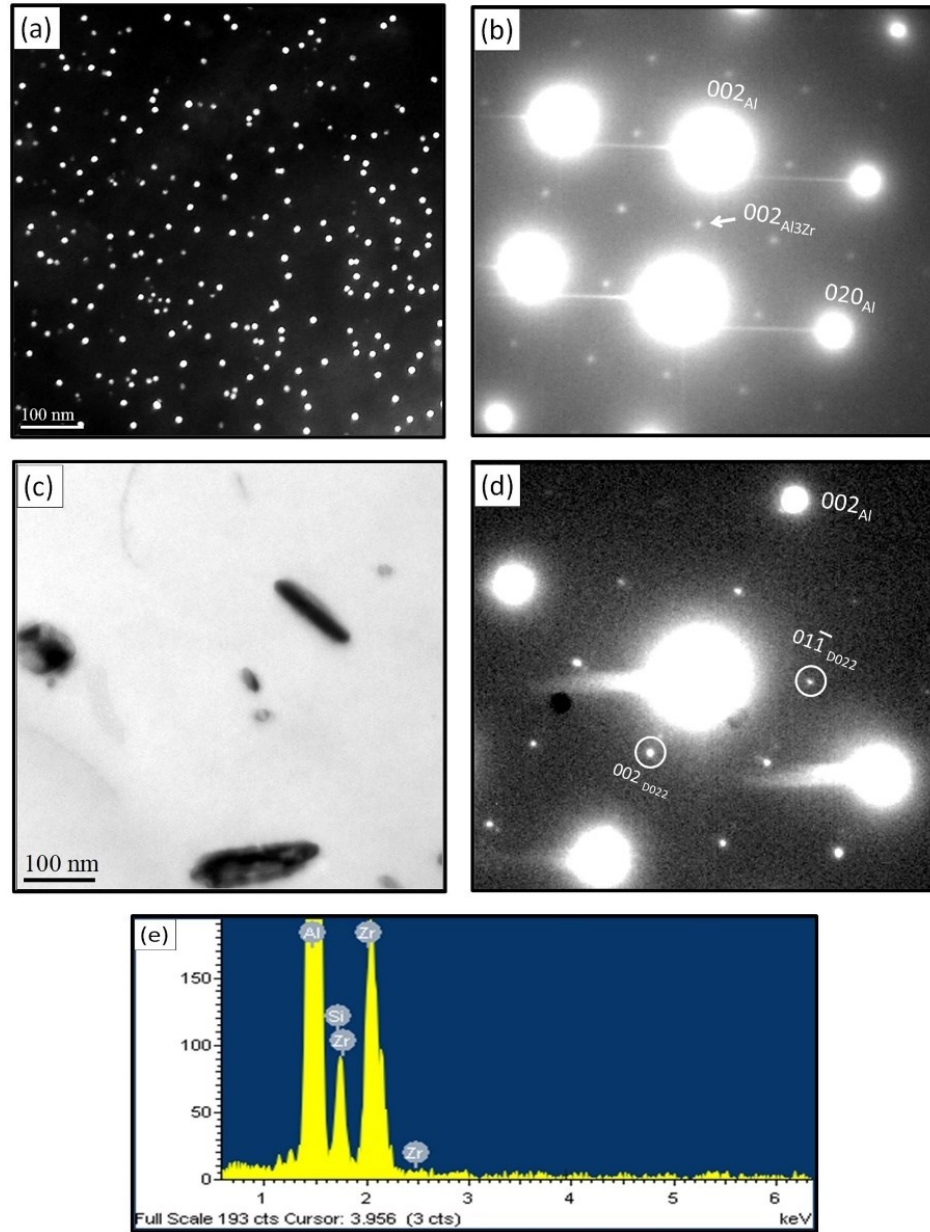


Figure 2.6 Identification of Zr-bearing dispersoids: (a) dark field TEM image showing $L1_2$ - Al_3Zr dispersoids after homogenization at 450 °C for 2 h; (b) SAEDP corresponding to (a); (c) bright field TEM image showing DO_{22} - $(Al,Si)_3Zr$ dispersoids after homogenization at 550 °C for 12 h; (d) SAEDP corresponding to (c); and (e) TEM-EDS analysis of DO_{22} - $(Al,Si)_3Zr$ dispersoids.

The number density and the average size of each dispersoid type were quantitatively measured based on image analysis of TEM images, and results are presented in Fig. 2.7. The L_{12} - Al_3Zr dispersoids exhibited their highest number density ($4300 \text{ 1}/\mu\text{m}^3$) and smallest average size (8.5 nm) after homogenization at $450 \text{ }^\circ\text{C}$ for 2 h. With increasing homogenization temperature or holding time, the number density decreased, while the average size increased, reaching the minimum and maximum values ($300 \text{ 1}/\mu\text{m}^3$ and 20 nm, respectively) after homogenization at $500 \text{ }^\circ\text{C}$ for 12 h. Almost no L_{12} - Al_3Zr dispersoids were detected in the samples homogenized at $550 \text{ }^\circ\text{C}$. The opposite trend was observed for the elongated DO_{22} - $(Al,Si)_3Zr$ dispersoids during homogenization. Their number density increased with higher temperature or longer time, reaching a maximum value of $155 \text{ 1}/\mu\text{m}^3$ with an average size of 96 nm when homogenized at $550 \text{ }^\circ\text{C}$ for 2 h. After extended time (12 h) at $550 \text{ }^\circ\text{C}$, the number density of the $(Al,Si)_3Zr$ dispersoids dropped to $50 \text{ 1}/\mu\text{m}^3$ while the size increased to 178 nm, revealing a significant coarsening effect (Fig. 2.5f). The opposite precipitation trends of the two types of Zr-bearing dispersoids suggest the progressive transformation of the L_{12} - Al_3Zr dispersoids to the DO_{22} - $(Al,Si)_3Zr$ dispersoids with increasing homogenization temperature and time.

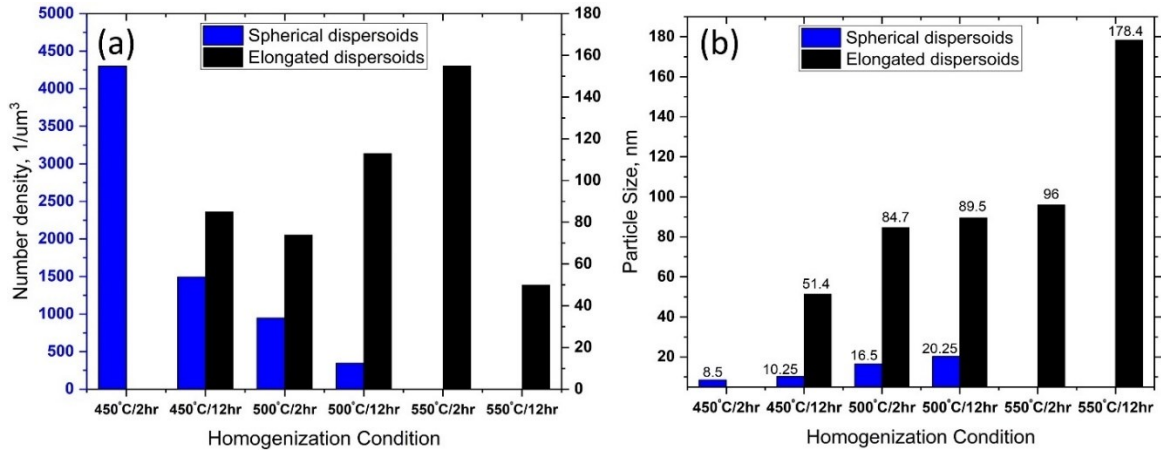


Figure 2.7 Number density (a) and average size (b) of $L1_2-Al_3Zr$ and $DO_{22}-(Al,Si)_3Zr$ dispersoids at different homogenization conditions.

At a relatively low temperature where the supersaturation level of Zr in the matrix is high, the diffusion rate of Zr atoms is sluggish. Therefore, the tendency for nucleation is higher than for growth which is evident by the high number density at 450 °C for 2 h. However, prolonging the soaking time allowed silicon diffusion and substitution for Al, which subsequently increased formation of $DO_{22}-(Al,Si)_3Zr$ at the expense of the metastable $L1_2-Al_3Zr$. This also suggests that 450 °C is too high to preserve the $L1_2-Al_3Zr$ phase for an extended soaking time. The other important factor is the available amount of Si in the matrix, which is essential for the transformation process. At low temperatures, the precipitation of Mg_2Si left less silicon available in the matrix for the transformation. In contrast, high temperature homogenization dissolved both primary and $\beta-Mg_2Si$, increasing the availability of the silicon in the matrix and promoting the transformation to $(Al,Si)_3Zr$.

3.3.3. Hot deformation behavior

Figure 2.8 shows typical flow curves for both base and 0.2Zr alloys at 400 °C and a strain rate of 1 s⁻¹ after different homogenized conditions. In all cases, the stress generally rose rapidly in the early stages of compression before reaching its peak value because of dislocation multiplication and the high rate of work hardening. Then, the flow stress continued to increase with increasing strain, but at a lower rate, indicating the occurrence of dynamic softening. However, work hardening was still dominant over softening due to the high deformation rate (1 s⁻¹), which leads to tangled dislocation structures [31]. The peak flow stress was defined as the tangent point on the flow curve by drawing a line along the steady-state region of the flow curve, as shown in Fig. 2.8a.

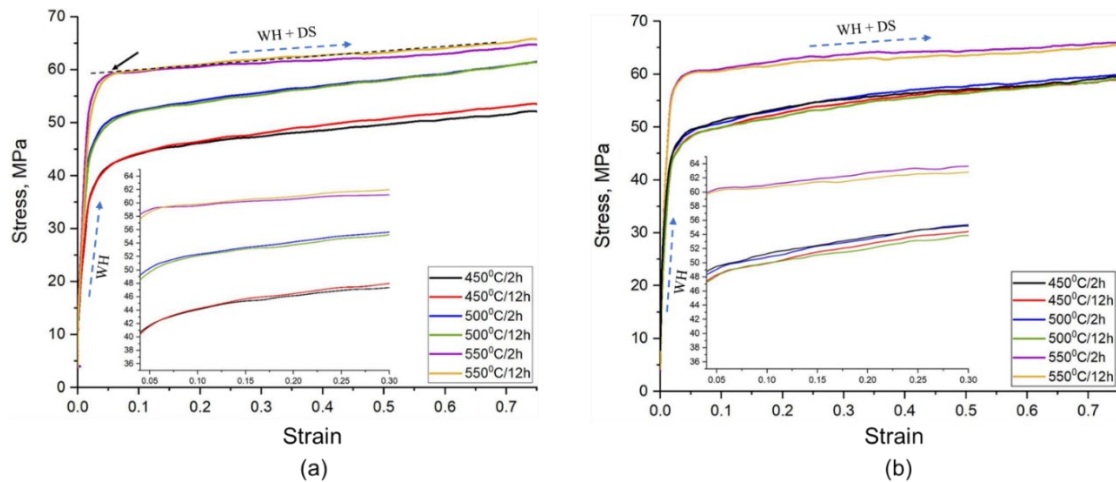


Figure 2.8 Typical flow curves at 400°C and 1 s⁻¹ strain rate: (a) base alloy and (b) 0.2Zr alloy. WH refers to the work hardening which mainly controls the flow behavior in the first stages of compression, while WH + DS refers to both the work hardening and the dynamic softening after reaching the peak flow stress.

For the base alloy (Fig. 2.8a), it was found that the peak flow stress increased progressively with increasing homogenization temperature, regardless of the holding time, attaining 43, 53, and 58 MPa at 450, 500, and 550 °C, respectively. Due to the absence of Zr-bearing dispersoids in the base alloy, solid solution strengthening was the major mechanism affecting the flow stress. Since the amount of equilibrium β -Mg₂Si precipitates decreased with increasing homogenization temperature (Fig. 2.2), which in turn enriched the α -Al solid solution with Mg and Si solutes, the solid solution strengthening was promoted, increasing the flow stress. In addition, homogenization at 550 °C dissolved the primary Mg₂Si phase in the α -Al, further increasing the solid solution strengthening and flow stress. For the 0.2Zr alloy (Fig. 2.8b), homogenizing at 500 or 550 °C resulted in no significant changes of the peak flow stress compared to the base alloy. However, the peak flow stress was increased by around 20 % compared to the base alloy (52 MPa vs. 46 MPa) after homogenization at 450 °C. This increase is attributed to the strengthening effect of the large amount of coherent Al₃Zr dispersoids, which were optimally precipitated at 450 °C. The pinning effect of such dispersoids on dislocation movement and dynamic recovery has been extensively reported in 7xxx alloys [8, 19, 32].

Two homogenization conditions for each alloy were selected for the investigation of the as-deformed microstructure, namely 450 °C for 2 h and 550 °C for 2 h, where the spherical Al₃Zr and elongated (Al,Si)₃Zr dispersoids attained their highest number densities, respectively. Figure 2.9 shows the corresponding EBSD Euler orientation maps, which reveal different features of the as-deformed microstructures, including low angle boundaries (2°-5°), medium angle boundaries (5°-15°), and high angle boundaries (>15°) represented by white, green, and black lines respectively. All maps showed elongated grains

perpendicular to the compression direction along with a large number of low and medium angle boundaries, indicating the presence of high densities of dislocations and subgrains [33]. It may be also noted that due to the deformation condition (high Z), the grain boundaries exhibited serrations and bulging for all conditions. For the base alloy, no significant differences were observed between the two homogenization conditions (Fig. 2.9a and b). Both conditions exhibited a recovered structure with a large amount of low and medium angle grain boundaries resulting from the high dislocation density generated during deformation.

EBSD mapping of the 0.2Zr alloy also revealed a recovered structure but with less homogenous deformation compared to the base alloy. This heterogenous deformation was evident by the grain subdivision (Fig. 2.9c) or the appearance of deformation bands (Fig. 2.9d). In addition, the samples homogenized at 450 °C (Fig. 2.9c) showed a significantly higher number density of dislocations and substructure compared to the base alloy. The high density of dislocation cells and subgrains observed at 450 °C was locally introduced due to the slow dynamic recovery with the piling-up of dislocations caused by fine Al_3Zr dispersoids [34]. However, homogenization at 550 °C resulted in a more recovered structure with a reduced level of low angle boundaries (Fig. 2.9d), indicating less inhibition of dynamic recovery associated with the coarse $(\text{Al,Si})_3\text{Zr}$ compared to the finer Al_3Zr dispersoids. The results are consistent with the flow curve trends in Fig. 2.8b, where the slope of the flow curve at 450 °C was higher than at 550 °C, corresponding to the higher inhibition of softening associated with Al_3Zr dispersoids compared to $(\text{Al,Si})_3\text{Zr}$. The increased coherency with the matrix and the smaller size of Al_3Zr dispersoids induced higher Zener-drag pinning effect on migrating subgrain boundaries during hot deformation [35, 36].

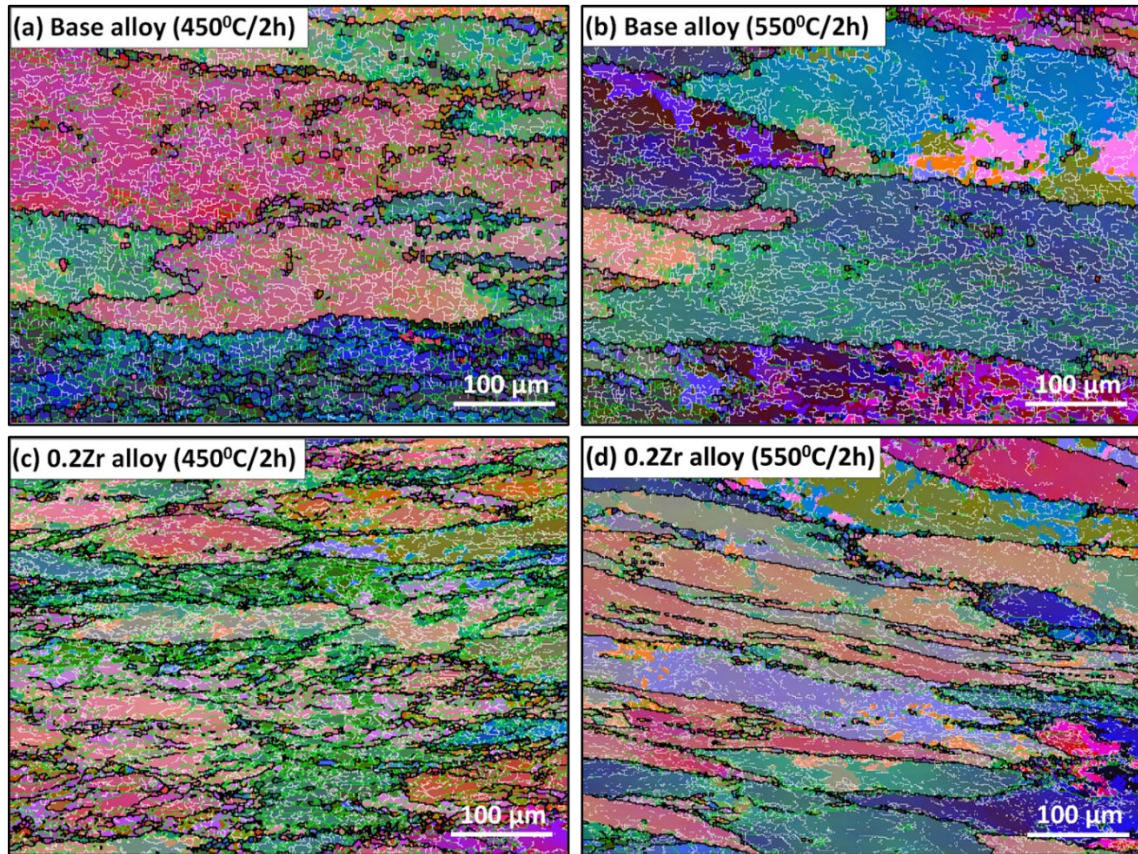


Figure 2.9 Euler orientation maps of as-deformed structures after hot deformation ($400\text{ }^{\circ}\text{C}$, 1 s^{-1}) for the base alloy (a, b) and 0.2Zr alloy (c, d) homogenized at $450\text{ }^{\circ}\text{C}/2\text{h}$ and $550\text{ }^{\circ}\text{C}/2\text{h}$, respectively. Low angle (2° - 5°), medium angle (5° - 15°), and high angle boundaries ($>15^{\circ}$) are represented by white, green, and black lines, respectively.

3.3.4. Recrystallization resistance

Figure 2.10 shows EBSD Euler orientation maps of the microstructures of the base and 0.2Zr alloys after annealing at $500\text{ }^{\circ}\text{C}$ for 4 h. The misorientation angle distribution and boundary fractions are presented in Fig. 2.11 and Table 2.2, respectively. The base alloy exhibited almost fully recrystallized grains after annealing regardless of the homogenization conditions, as shown in Figs. 2.10a and b. In contrast, the 0.2Zr alloy homogenized at

450°C/2h still retained the original elongated grains with a recovered structure (Fig. 2.10c), while the 550°C/2h treatment resulted in a partially recrystallized structure (Fig. 2.10d).

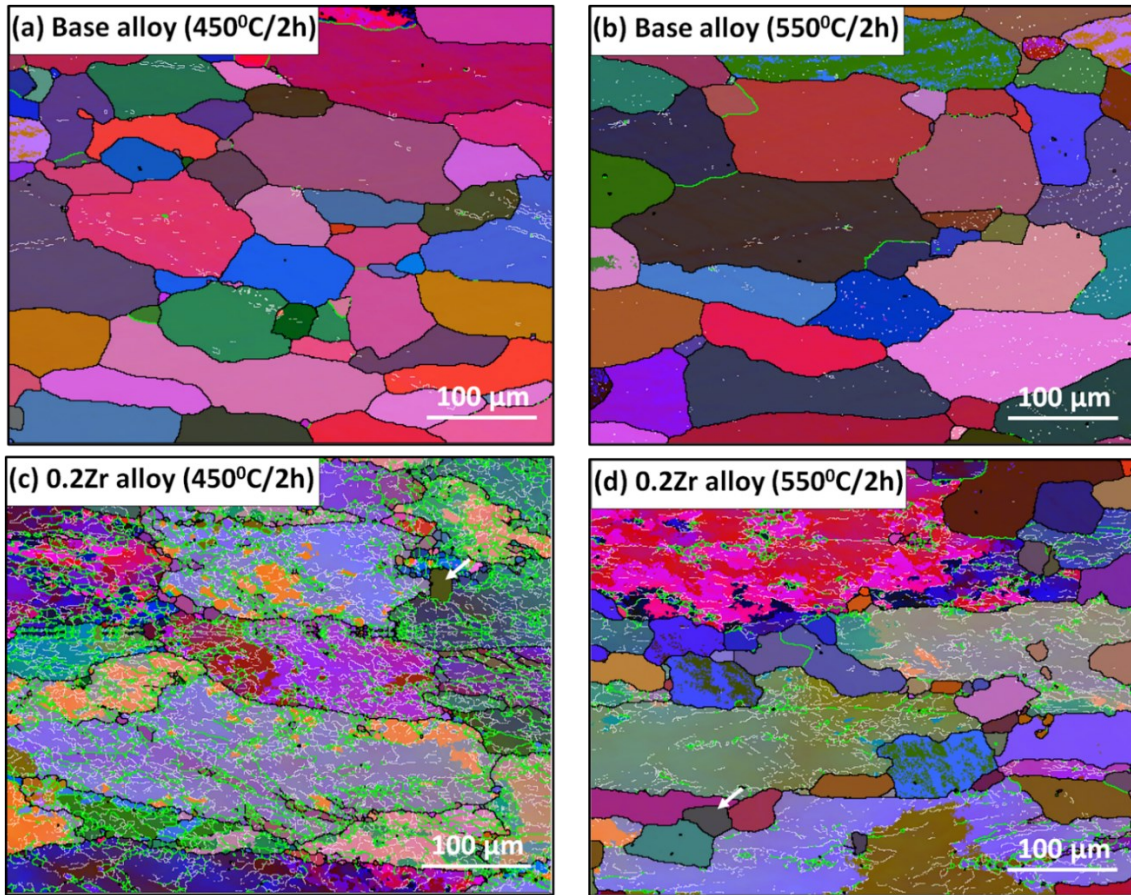


Figure 2.10 Euler orientation maps after annealing (500 °C for 4 h) for the base (a, b) and 0.2Zr alloys (c, d) for two homogenization conditions (450°C/2h and 550°C/2h). Low angle (2°-5°), medium angle (5°-15°), and high angle boundaries (>15°) are represented by white, green, and black lines, respectively.

The quantitative results in Fig. 2.11 and Table 2.2 show that the annealed base alloy possessed mostly high angle grain boundaries (HAB, > 90%) after both homogenization conditions, confirming a fully recrystallized grain structure. The low recrystallization resistance of the base alloy can be attributed to the absence of particles/dispersoids with a

sufficient pinning effect, which could retard the boundary migration. On the other hand, the majority of the grain boundaries in the 0.2Zr alloy after annealing were low angle boundaries (LAB). The grain structures observed in the annealed 0.2Zr alloy depended on the homogenization treatment applied. Homogenization at 450 °C for 2 h, resulted in a recovered structure with a high density of low angle boundaries, as shown in Figs. 2.10c and 2.11c. Only a very small number of recrystallized grains was observed near original grain boundaries (arrowed in Fig. 2.10c). The misorientation angle distribution in Fig. 2.11c showed a high fraction (82.3 %) of low angle boundaries (LAB) with a mean angle of 10.6°, indicating a strong inhibiting effect of fine spherical dispersoids Al₃Zr on the dislocation polygonization and subgrain coalescence. After homogenization at 550 °C for 2 h (Fig. 2.10d and 2.11d), the density of LAB was substantially reduced, and correspondingly HAB were increased. An increased number of coarse grains featuring no internal substructure were also observed along grain boundaries (arrowed in Fig. 2.10d), indicating a higher growth rate of recrystallized grains during annealing as compared to after homogenization at 450 °C for 2 h. The misorientation angle distribution (Fig. 2.11d and Table 2.2) also reflected a clear increase in the fractions of HAB for the higher temperature treatment (38.3 % at 550 °C for 2 h vs. 17.7% at 450 °C for 2 h) and an increase in mean misorientation angle (17.9° at 550 °C for 2 h vs. 10.6° at 450 °C for 2 h) relative to homogenization at 450 °C for 2 h. These results indicate that the elongated (Al, Si)₃Zr were less effective at inhibiting recrystallization than the fine Al₃Zr dispersoids.

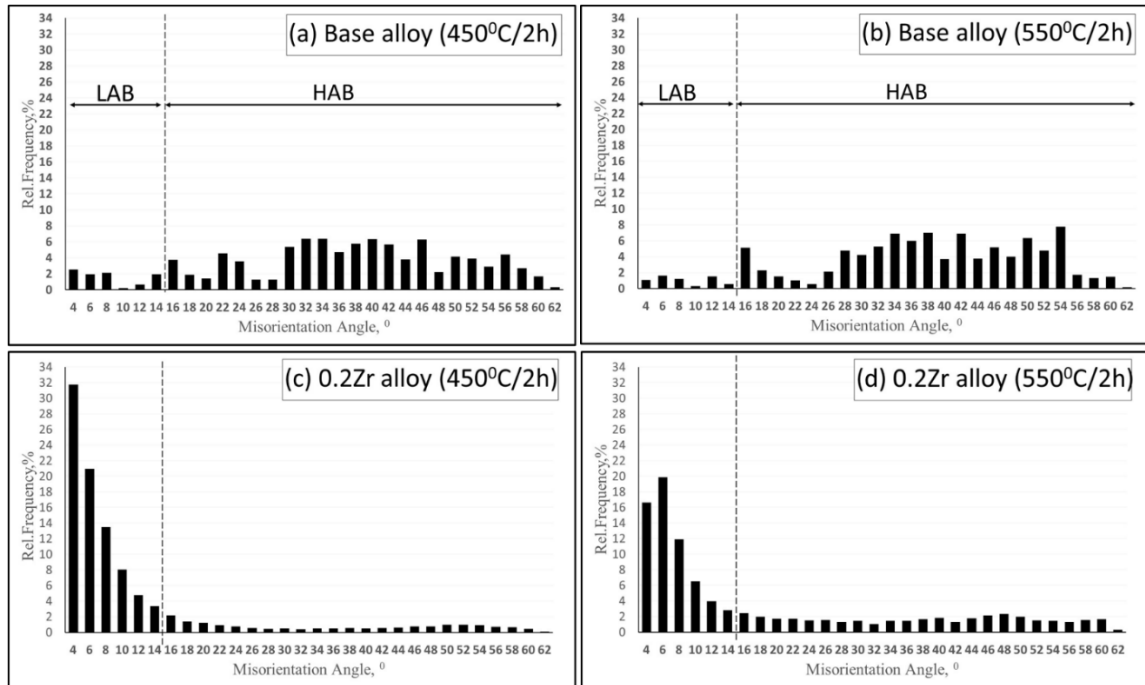


Figure 2.11 Misorientation angle distribution for base and 0.2Zr alloys for different homogenization conditions after annealing treatment at 500 °C for 4 h.

Table 2.2. Quantitative analysis of EBSD results.

Alloy	Homogenization condition	LAB (<15°) fraction, %	HAB (≥15°) fraction, %	Mean angle boundary, °
Base	450°C/2h	9.4	90.6	34.6
	550°C/2h	6.3	93.7	36.2
0.2Zr	450°C/2h	82.3	17.7	10.6
	550°C/2h	61.7	38.3	17.9

According to the expression for Zener pinning [8, 37], particles having a smaller size and higher volume fraction produce a higher pinning force. Moreover, there are two other essential particle features controlling the grain boundary pinning effect, namely the interface coherency and the uniformity of the particle distribution within the microstructure.

Regarding the coherency, the maximum pinning force associated with coherent dispersoids was reported by Liu [17] to be twice that produced by incoherent dispersoids of the same size. Therefore, the smaller, coherent Al_3Zr dispersoids in the present study were more effective at inhibiting boundary migration and consequently in increasing the recrystallization resistance compared to the coarse, incoherent $(\text{Al,Si})_3\text{Zr}$ dispersoids. The other important factor is the dispersoid free zones (DFZs) arising from the non-homogeneous distribution of Zr in the matrix during solidification, which leads to an uneven distribution of dispersoids [8, 19, 35]. During high temperature homogenization, more Si becomes available due to the dissolution of primary Mg_2Si into the matrix, promoting $(\text{Al,Si})_3\text{Zr}$ dispersoid formation in the dendrite centers. Figure 2.12a shows the distribution of $(\text{Al,Si})_3\text{Zr}$ dispersoids after homogenization at 550 °C for 2 h using a dark field optical micrograph. There was a high number density of dispersoids in the dendrite centers, but large DFZs were observed at interdendritic and grain boundaries up to 10 μm in width. Therefore, recrystallization during annealing was more likely to occur in DFZs along the grain boundaries. The DFZs associated with Al_3Zr dispersoids formed during low-temperature homogenization at 450 °C were significantly narrower (~ 450 nm, Fig. 2.12b), and this further contributed to the effectiveness of the Al_3Zr dispersoids at inhibition of recrystallization.

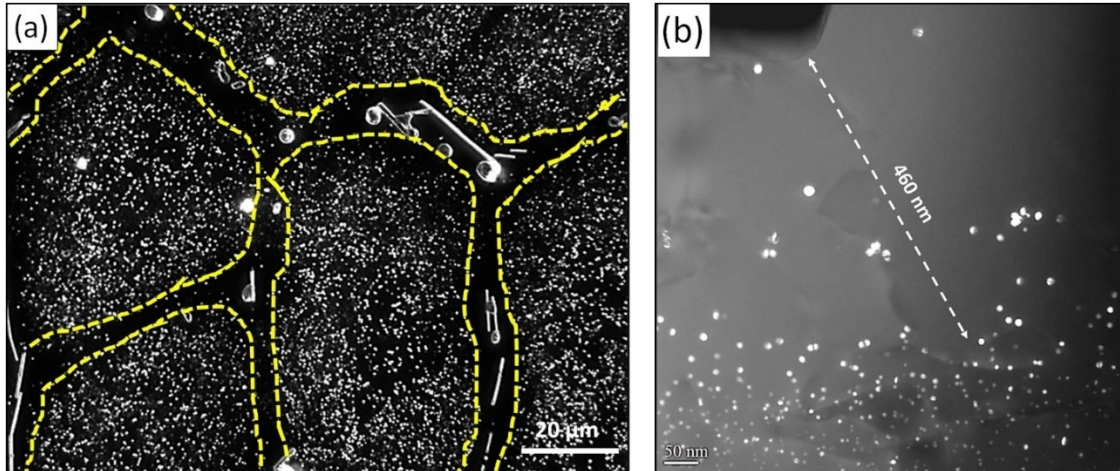


Figure 2.12 OM dark field image (a) and dark field TEM image (b) of 0.2Zr alloy homogenized at 550°C/2h (a) and 450°C/2h (b), respectively.

2.4. Conclusions

The evolution of Zr-bearing dispersoids in an Al-0.8%Mg-1.0%Si alloy and their effect on hot deformation and recrystallisation resistance were studied under different homogenization conditions. The following conclusions can be drawn:

- (1) Two types of Zr-bearing dispersoids can be precipitated in Al-0.8%Mg-1.0%Si alloy with an addition of 0.2 wt.% Zr, depending on the homogenization conditions. Homogenization at 450 °C for 2 h resulted in the precipitation of fine and coherent $L1_2$ - Al_3Zr dispersoids. With increasing homogenization temperature and/or time, elongated and incoherent DO_{22} - $(Al,Si)_3Zr$ dispersoids were formed, which dominated the microstructure when homogenized at 550 °C.
- (2) The addition of 0.2 wt.% Zr combined with homogenization at 450 °C produced a high density of fine Al_3Zr dispersoids (~10 nm) with a uniform distribution, increasing the high-temperature flow stress by 20% relative to the base alloy free of

Zr, and promoting a strong Zener pinning effect on dislocation movement and a high inhibiting effect on dynamic recovery.

- (3) The addition of 0.2 wt.% Zr combined with homogenization at a conventional temperature of 550 °C produced a low density of coarser (AlSi)₃Zr dispersoids (100-200 nm), which had a minimal effect on high-temperature flow stress and a moderate effect on the retardation of dynamic recovery.
- (4) Both dispersoid types were found to increase the recrystallization resistance during post-deformation annealing. However, the pinning effect of the Al₃Zr dispersoids and hence the corresponded recrystallization resistance was significantly higher than that associated with (Al,Si)₃Zr. As a result, selection of the homogenisation treatment is critical to control the Zr dispersoid type and the microstructure evolution during thermomechanical treatment.

References

1. HIRSCH, J., *Recent development in aluminium for automotive applications*, in *Transactions of Nonferrous Metals Society of China*. 2014. p. 1995-2002.
2. Ren, J., et al., *An initial report on achieving high comprehensive performance in an Al-Mg-Si alloy via novel thermomechanical processing*, in *Journal of Alloys and Compounds*. 2018. p. 679-683.
3. Guemini, R., A. Boubertakh, and G.W. Lorimer, *Study of the recrystallization process of AlMgSi alloys containing transition elements*, in *Journal of Alloys and Compounds*. 2009. p. 451-457.
4. Dong, Q., et al., *Precipitation-induced mitigation of recrystallization in ultra-thin, cold-rolled AlScZrMn(Mg) sheets at brazing temperatures: The critical effect of alloy composition and thermal processing route*, in *Acta Materialia*. 2020. p. 308-323.
5. Hichem, F. and G. Rebai, *Study of dispersoid particles in two Al-Mg-Si aluminium alloys and their effects on the recrystallization*. *Applied Physics A*, 2015. **119**(1): p. 285-289.
6. Kahrıman, F. and M. Zeren, *The effect of Zr on aging kinetics and properties of as-cast AA6082 alloy*, in *International Journal of Metalcasting*. 2017, Springer. p. 216-222.
7. Mikhaylovskaya, A.V., et al., *Precipitation behavior of L12 Al₃Zr phase in Al-Mg-Zr alloy*. *Materials Characterization*, 2018. **139**: p. 30-37.
8. Guo, Z., G. Zhao, and Chen, X.G, *Effects of two-step homogenization on precipitation behavior of Al₃Zr dispersoids and recrystallization resistance in 7150 aluminum alloy*. *Materials Characterization*, 2015. **102**: p. 122-130.
9. Zakharov, V.V., *About Alloying of Aluminum Alloys with Transition Metals*, in *Metal Science and Heat Treatment*. 2017, Springer New York LLC. p. 67-71.

10. Cassell, A.M., et al., *Dispersoid composition in zirconium containing Al-Zn-Mg-Cu (AA7010) aluminium alloy*, in *Acta Materialia*. 2019. p. 135-146.
11. Shi, C. and Chen, X.G, *Evolution of activation energies for hot deformation of 7150 aluminum alloys with various Zr and V additions*, in *Materials Science and Engineering A*. 2016, Elsevier Ltd. p. 197-209.
12. Kahrman, F. and M. Zeren, *Microstructural and Mechanical Characterization of Al-0.80Mg-0.85Si-0.3Zr Alloy*. *Archives of Foundry Engineering*, 2017. **17**: p. 73-78.
13. Litynska, L., et al., *TEM and HREM study of Al₃Zr precipitates in an Al-Mg-Si-Zr alloy*. *J Microsc*, 2006. **223**(Pt 3): p. 182-4.
14. Himuro, Y., K. Koyama, and Y. Bekki, *Precipitation Behaviour of Zirconium Compounds in Zr-Bearing Al-Mg-Si Alloy*. *Materials Science Forum*, 2006. **519-521**: p. 501-506.
15. Kahrman, F. and M. Zeren, *Mechanical and Fractographical Characterization of Extruded Al-Mg-Si-Zr Alloys*, in *MATEC Web of Conferences*, S. Pantelakis and S. Koubias, Editors. 2018. p. 02017.
16. Poletti, C., et al., *Microstructure development in hot deformed AA6082*, in *Materials Science and Engineering: A*. 2011. p. 2423-2430.
17. Liu, S., et al., *Effects of Combined Additions of Mn and Zr on Dispersoid Formation and Recrystallization Behavior in Al-Zn-Mg Alloys*. *Metallurgical and Materials Transactions A*, 2019. **50**(10): p. 4877-4890.
18. Eivani, A.R., et al., *An experimental and theoretical investigation of the formation of Zr-containing dispersoids in Al-4.5Zn-1Mg aluminum alloy*, in *Materials Science and Engineering: A*. 2010. p. 2418-2430.
19. Morere, B., et al., *The influence of Al₃Zr dispersoids on the recrystallization of hot-deformed AA 7010 alloys*. *Metallurgical and Materials Transactions A*, 2001. **32**(3): p. 625-632.

20. Shi, C. and Chen, X.G, *Effect of Zr addition on hot deformation behavior and microstructural evolution of AA7150 aluminum alloy*, in *Materials Science and Engineering: A*. 2014. p. 183-193.
21. Li, H., et al., *Effects of Er and Zr additions on precipitation and recrystallization of pure aluminum*. Scripta Materialia, 2013. **68**(1): p. 59-62.
22. MENG, Y., Z.-h. ZHAO, and J.-z. CUI, *Effect of minor Zr and Sc on microstructures and mechanical properties of Al–Mg–Si–Cu–Cr–V alloys*, in *Transactions of Nonferrous Metals Society of China*. 2013. p. 1882-1889.
23. Zou, L., et al., *Microstructures and tensile properties of Al-Zn-Cu-Mg-Zr alloys modified with scandium*, in *Materials Science*. 2008, Springer. p. 120.
24. Birol, Y., *Effect of Cr and Zr on the grain structure of extruded EN AW 6082 alloy*. Metals and Materials International, 2016. **20**(4): p. 727-732.
25. Cowley, J.M., *Electron Microdiffraction*, in *Advances in Electronics and Electron Physics*. 1978, Springer Science & Business Media. p. 1-53.
26. Wang, F., et al., *The grain refinement mechanism of cast aluminium by zirconium*. Acta Materialia, 2013. **61**(15): p. 5636-5645.
27. Clouet, E., J.M. Sanchez, and C. Sigli, *First-principles study of the solubility of Zr in Al*. Physical Review B, 2002. **65**(9): p. 094105.
28. Samaras, S.N. and G.N. Haidemenopoulos, *Modelling of microsegregation and homogenization of 6061 extrudable Al-alloy*, in *Journal of Materials Processing Technology*. 2007. p. 63-73.
29. Farh, H., et al., *Nucleation of dispersoids study in some Al-Mg-Si alloys*. Annales de chimie Science des Matériaux, 2010. **35**(5): p. 283-289.

30. Sato, T., A. Kamio, and G.W. Lorimer, *Effects of Si and Ti Additions on the Nucleation and Phase Stability of the L12-Type Al₃Zr Phase in Al-Zr Alloys*. Materials Science Forum, 1996. **217-222**: p. 895-900.
31. Rokni, M.R., et al., *An investigation into the hot deformation characteristics of 7075 aluminum alloy*, in *Materials & Design*. 2011. p. 2339-2344.
32. LI, D.-f., et al., *Dynamic recrystallization behavior of 7085 aluminum alloy during hot deformation*, in *Transactions of Nonferrous Metals Society of China*. 2016. p. 1491-1497.
33. Shakiba, M., N. Parson, and Chen, X.G, *Hot deformation behavior and rate-controlling mechanism in dilute Al-Fe-Si alloys with minor additions of Mn and Cu*, in *Materials Science and Engineering: A*. 2015. p. 572-581.
34. Shi, C. and Chen, X.G, *Effect of vanadium on hot deformation and microstructural evolution of 7150 aluminum alloy*, in *Materials Science and Engineering: A*. 2014. p. 91-102.
35. Jia, Z., et al., *Effect of homogenization and alloying elements on recrystallization resistance of Al-Zr-Mn alloys*. Materials Science and Engineering A, 2007. **444**(1-2): p. 284-290.
36. Wu, Y., et al., *Joint effect of micro-sized Si particles and nano-sized dispersoids on the flow behavior and dynamic recrystallization of near-eutectic Al-Si based alloys during hot compression*. Journal of Alloys and Compounds, 2021. **856**: p. 158072.
37. Lai, J., C. Shi, and Chen, X.G, *Effects of V addition on recrystallization resistance of 7150 aluminum alloy after simulative hot deformation*. Materials Characterization, 2014. **96**: p. 126-134.

CHAPTER 3 : Effect of Si Level on the Evolution of Zr-bearing Dispersoids and the Related Hot Deformation and Recrystallization Behaviors in Al-Si-Mg 6xxx Alloys

(Published in the Journal of Advanced Engineering Materials)

Abstract

The precipitation behavior of Zr-bearing dispersoids is investigated in Al-Si-Mg 6xxx alloys with different Si levels (0.4, 0.7, and 1.0 wt%) at three homogenization temperatures (450, 500, and 550 °C). The hot deformation behavior is studied using uniaxial compression tests at different Zener-Hollomon parameters. The microstructure evolution during hot deformation and post-deformation annealing is evaluated using the electron backscatter diffraction technique. The results show a significant influence of the Si level and homogenization temperature on the precipitation of two types of Zr-bearing dispersoids. Si promotes the precipitation of both spherical L_{12} - Al_3Zr and elongated DO_{22} - $(Al,Si)_3(Zr,Ti)$ dispersoids during low-temperature homogenization. However, it accelerates the transformation of Zr dispersoids from L_{12} to DO_{22} at high homogenization temperature. The flow stress is more influenced by the solid solution level and hot deformation parameters rather than by the dispersoid distribution. The fine dense L_{12} - Al_3Zr dispersoids provide higher recrystallization resistance during post-deformation annealing compared to the large elongated DO_{22} - $(Al,Si)_3(Zr,Ti)$ dispersoids. Owing to the uniform distribution of dispersoids and limited dispersoid free zones, the high Si alloy (1.0%) exhibits the best recrystallization resistance among the three alloys studied.

Keywords: Al-Mg-Si 6xxx alloys, Zr-bearing dispersoids, Hot Deformation, Recrystallization Resistance

3.1. Introduction

Owing to the variety of mechanical properties offered by Al-Mg-Si 6xxx alloys, they are used in a wide range of applications, from light architectural uses to high-stress structural components in the automobile, construction, and marine industries[1, 2]. These alloys are commonly used in the form of extruded profiles acquiring nearly 90% of all aluminum extrusion products since they can be extruded at higher speeds than other alloy series with less surface quality problems [3]. Hence, hot extrusion is one of the main plastic deformation processes for 6xxx alloys to achieve the desirable and complex geometric profiles. However, maintaining a fibrous grain structure is desirable to improve strength, fatigue, and toughness properties[4]. Also, controlling the grain structure is of great importance for adequate performance during post-deformation heat treatment such as annealing or solution treatment [5]. In this regard, adjusting the alloy chemistry, homogenization treatment, and hot deformation parameters are the main approaches.

The addition of transition elements that have limited solubility and diffusivity in the aluminum matrix is one of the effective methods to control the grain structure during and after hot deformation in 6xxx alloys [6, 7]. Among those elements, Zr has received much attention in recent years as an addition to aluminum alloys [4, 8, 9] , due to its very low diffusivity and excellent lattice mismatch with the aluminum matrix [10]. It has been proven to positively affect the flow stress and recrystallization resistance for several aluminum alloys [8, 11, 12]. This can be achieved by introducing a high density of coherent $L1_2$ -Al₃Zr dispersoids that precipitated during homogenization at relatively low-temperature [8].

However, Zr alone has not been widely used in 6xxx alloys to inhibit the recrystallization, and it is often combined with other elements such as Cr or Sc. For instance, Meng et al. [13] observed a strong inhibition effect on dynamic recrystallization after adding 0.15wt% Zr into Al-Mg-Si-Cu-Cr alloy. Also, Birol reported that the combined addition of Zr and Cr had a positive impact on the recrystallization resistance of 6082 alloys [4]. Moreover, better recrystallization resistance was reported in Al-Mg-Si-Sc-Zr alloy compared to Al-Mg-Si-Mn-Cr [14].

The presence of a considerable amount of silicon could influence the nucleation rate and structure of Al_3Zr at high temperatures. The nucleation of $\text{L}_{12}\text{-Al}_3\text{Zr}$ was reported to be enhanced by Si, and the silicon-vacancy clusters that form by attractive binding energy may act as heterogeneous sites for Zr dispersoids [15]. Si was also reported to reduce the peak-aging time of Al_3Zr dispersoids by improving the Zr diffusion kinetics in the Al matrix in the temperature range of 300 to 400 °C [16, 17]. In addition, Si was reported to stabilize $\text{DO}_{22}\text{-(Al,Si)}_3\text{Zr}$ at the expense of the metastable $\text{L}_{12}\text{-Al}_3\text{Zr}$ via phase transformation during high-temperature homogenization [13, 17, 18]. This transformation occurs by substituting Al by a small amount of Si and changing the crystal structure of L_{12} to DO_{22} instead of the stable DO_{23} that forms in the absence of Si [18]. $\text{L}_{12}\text{-Al}_3\text{Zr}$ has spherical morphology with a small diameter ranging from 8 to 60 nm. On the other side, the tetragonal DO_{22} has a rod-like morphology with a much larger size, around 1.5 μm long and 0.5 μm wide [13, 17].

Dynamic recovery (DRV) and dynamic recrystallization (DRX) are the common softening mechanisms in aluminum alloys during thermomechanical processing. DRV is the most frequently encountered due to aluminum's high stacking fault energy, high dislocation mobility, and low grain boundary mobility [19]. While DRX can occur by the formation of

new grains at particular deformation conditions (i.e., deformation temperature and strain rate). The Zener-Hollomon parameter (Z) describes the combined effect of the temperature and strain rate on the flow stress and the microstructure evolution during hot deformation [20]. On the other hand, 6xxx alloys are usually subjected to a post-deformation heat treatment (annealing or solutionizing and ageing) to achieve the appropriate mechanical properties. Static recrystallization can occur during post-deformation heat treatment by migration of grain boundaries and the formation of new grains [21]. However, recrystallization can be significantly inhibited by the interaction between the thermally stable dispersoids and grain boundaries, which is commonly described by the Zener drag force (P_z) [22].

As mentioned above, Si plays a substantial role in the precipitation of Zr-bearing dispersoids in 6xxx alloys, which, in turn, can significantly influence the hot deformation and recrystallization resistance. However, there is a lack of literature on how and at which level Si affects the precipitation of Zr-bearing dispersoids in 6xxx alloys. The present work was undertaken to study the evolution of Zr-bearing dispersoids in 6xxx alloys at different levels of Si (0.4 -1.0 wt%) during homogenization. In addition, the effects of this evolution on the hot deformation behavior and recrystallization resistance during post-deformation heat treatment were investigated.

3.2. Experimental procedures

Three 6xxx alloys with different Si levels (0.4, 0.7 and 1.0 wt%) were prepared. The chemical compositions of the experimental alloys analyzed by optical emission spectroscopy are listed in Table 3.1. Because the major hardening precipitates in the 6xxx alloys are β'' -Mg₅Si₆ precipitates with a Mg:Si atomic ratio of around 1:1[23, 24], the Mg level was adjusted to

maintain the atomic ratio between Mg and Si at 1:1 for the three alloys. The alloys were prepared using pure Al (99.7 wt%) and pure Mg (99.8 wt%) as well as Al-50 wt% Si, Al-25 wt% Fe, and Al-15 wt% Zr master alloys. The materials were melted using an electrical resistance furnace and cast into a permanent steel mold preheated to 250 °C to obtain rectangular ingots with a dimension of 30 mm × 40 mm × 80 mm. The cast ingots were homogenized at three temperatures (450, 500, and 550 °C) with a heating ramp rate of 100°C/h and soaked for 5 h followed by water quenching to room temperature.

For microstructural investigation, samples were cut from the homogenized ingots and prepared using standard metallographic procedures. The dispersoids were observed using optical microscopy (Nikon, Eclipse ME600) and scanning electron microscopy (SEM, JEOL-6480LV) after etching with 0.5% HF for 60 s. A transmission electron microscope (TEM, JEM-2100) operated at 200 kV was used to examine the Zr-bearing dispersoids in detail. The TEM samples were electropolished using a twin-jet electropolisher operated at 20V and -20 °C with 30 vol.% nitric acid and 70 vol.% methanol. The samples were observed in the bright field mode near $\langle 001 \rangle$ zone axis of α -Al matrix, while the dark field mode was used for the observation of L_{12} structured dispersoids using their superlattice reflection. The TEM foil thickness was measured by the Kossel-Kossel-Möllenstedt (K-M) fringes with the convergent electron beam diffraction method [25]. By Using an Image analyzer, the average size and number density of tiny Al_3Zr dispersoids were measured based on TEM images, whereas SEM images were used in the case of large elongated dispersoids (>100 nm). In order to estimate the solid solution level in the aluminum matrix after homogenization, electrical conductivity measurements were performed using a Simgascope SMP 10 device at

room temperature. Six measurements were recorded on each sample, and the mean value was reported.

Table 3.1. Chemical composition (wt.%) of the experimental alloys

Alloy ID	Si	Mg	Fe	Zr	Ti	Al
0.4Si	0.39	0.35	0.16	0.15	0.13	Bal.
0.7Si	0.71	0.64	0.15	0.14	0.12	Bal.
1.0Si	0.99	0.89	0.18	0.15	0.14	Bal.

Uniaxial hot compression tests were performed on a Gleeble 3800 thermomechanical simulator using cylindrical samples with a diameter of 10 mm and length of 15 mm. The compression tests involved heating the samples up to the deformation temperature with a heating rate of 2 °C/s and then holding for 3 minutes to ensure a uniform temperature. Three deformation conditions (350°C, 1.0 s⁻¹, 400°C, 0.1 s⁻¹ and 450°C, 0.001 s⁻¹) were selected representing high-, medium- and low-Z conditions, respectively. The samples were deformed to a true strain of 0.7, followed by water quenching to retain the deformed microstructure. Post-deformation annealing was performed at 500 °C and 540 °C for 1 h for selected homogenization conditions to study the static recrystallization resistance.

The microstructures after deformation and after annealing were characterized using the electron backscatter diffraction (EBSD) technique. The EBSD samples were sectioned parallel to the deformation axis along the centerline direction and then carefully polished to obtain high indexing quality. For an accurate comparison, the central region of the samples was examined for all conditions. All-Euler orientation maps were used with a step size of 1 μm for grain structure. The low angle boundaries (2-5°), medium angle boundaries (5-15°), high angle boundaries (>15°), and the original grain boundaries (>30°) were presented by

white, green, thin black, and solid black lines respectively. Sub-grain boundaries are characterized with misorientations of 2–15°, while the grain boundaries are those with misorientation angles above 15°. All misorientation angles below 2° were not considered to avoid the noise caused by the sample surface condition.

3.3. Results and discussion

3.3.1. As-cast microstructure

Figure 3.1 shows the as-cast microstructure of the studied alloys. The three studied alloys showed similar microstructures which consists of the α -Al matrix, Fe-rich intermetallics (grey phase) and the primary eutectic Mg_2Si (dark phase) adjacent to the intermetallics. Increasing the content of Si and Mg leads to an increase in the amount and size of eutectic Mg_2Si as they have strong segregation tendencies towards the interdendritic regions [26]. In addition, some equilibrium β - Mg_2Si particles were found to be precipitated close to the interdendritic regions. The high level of supersaturation of Mg and Si along these regions may promote the precipitation of β - Mg_2Si during cooling down after solidification. Therefore, the highest precipitation of such particles was observed in 1.0Si alloy. It is worth mentioning that no Zr-dispersoids were found in the as-cast conditions.

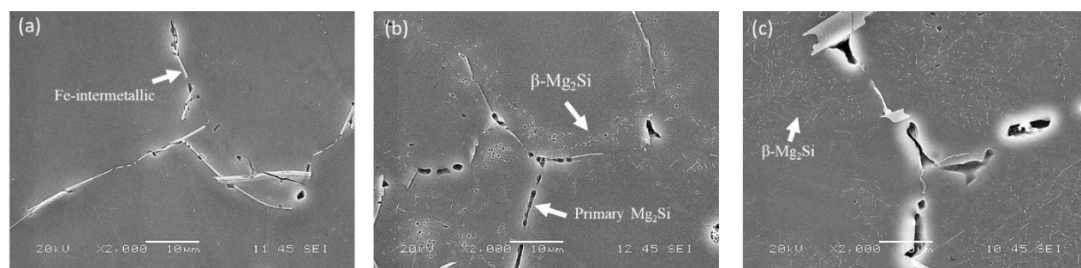


Figure 3.1 SEM images of As-cast condition for (a) 0.4Si, (b) 0.7Si and (c) 1.0Si alloys.

3.3.2. Evolution of Zr-bearing dispersoids during homogenization

Figure 3.2 shows the evolution of Zr-bearing dispersoids after different homogenization conditions for the 0.4Si, 0.7Si and 1.0Si alloys, which were significantly affected by the homogenization temperature and alloy composition. With increasing homogenization temperature, the size and number density of dispersoids increased for all three alloys. However, at a given homogenization temperature, the number density of dispersoids varied with the Si content. For the 0.4Si alloy (Figure 3.2a-c), the precipitation of dispersoids was relatively weak, resulting in a low number density. In the case of 0.7Si alloy (Figure 3.2d-f), a higher number density of dispersoids was generally observed compared to the 0.4Si alloy. With increasing Si to 1.0% (Figure 3.2g-i), a further significant increase in the number density of dispersoids was observed at all homogenization temperatures. At low homogenization temperature (450 °C), the equilibrium β -Mg₂Si particles were also precipitated and co-existed with dispersoids, as shown in the SEM images (white arrows) in Figure 3.3. In general, the β -Mg₂Si particles were larger and less dense than Zr-bearing dispersoids. However, the amount of β -Mg₂Si particles was significantly reduced with increasing the homogenization temperature and they were almost completely dissolved at 550 °C (Figure 3.3d-f).

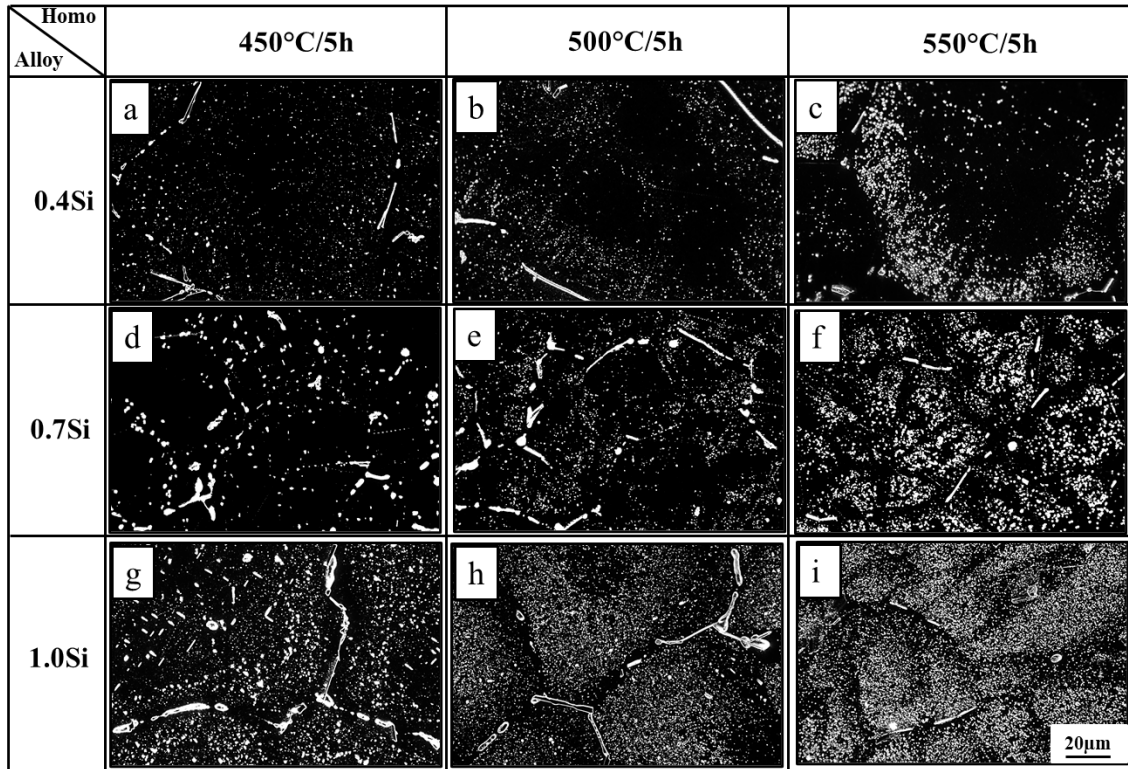


Figure 3.2 Dark-field optical micrographs showing the distribution of Zr-bearing dispersoids for different Si levels and homogenization temperatures.

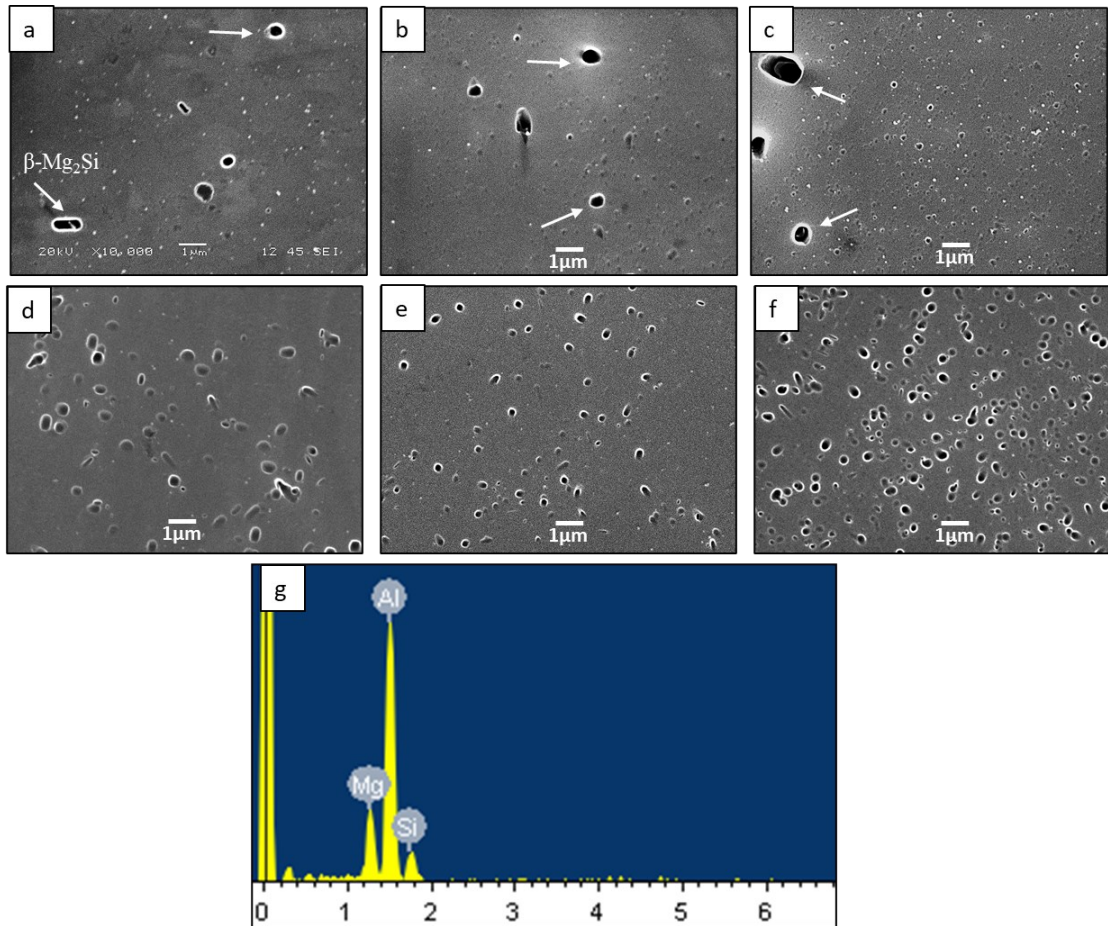


Figure 3.3 SEM micrographs showing Zr-dispersoids and β -Mg₂Si (large particles indicated by white arrows) after homogenization at 450°C/5h (a-c) and 550°C/5h (d-f) for 0.4Si, 0.7Si and 1.0Si alloys, and (g) SEM-EDS analysis of β -Mg₂Si particle.

TEM was used to characterize the morphology and the type of Zr-bearing dispersoids. Figure 3.4 shows typical bright-field TEM images obtained after 550 °C homogenization. Two types of dispersoids were observed in the case of 0.4Si alloy (Figure 3.4a): large elongated dispersoids indicated by black arrows and spherical dispersoids with a much smaller size shown in the inset of Figure 3.4a. The same two types of dispersoids were also observed in 0.7Si alloy but with a higher density (Figure 3.4b). The elongated dispersoids were mainly located near grain boundaries, as shown in Figure 3.2c and f, while the spherical

ones were located at the grain centers. Only elongated dispersoids were observed in the 1.0Si alloy (Figure 3.4c), with a uniform distribution (Figure 3.2i). Furthermore, The corresponding selected area diffraction pattern (SADP) taken along $\langle 001 \rangle_{Al}$ zone axis (the inset of Figure 3.4c) indicates that the crystal structure of the elongated dispersoids is DO_{22} , which was also reported by Litynska et al. [18].

The TEM-EDS analysis of spherical dispersoids (Figure 3.4d) showed that they contain only Zr, and they could therefore be identified as Al_3Zr dispersoids. However, considerable amounts of Si and Ti were detected beside Zr in the case of elongated dispersoids (Figure 3.4e). It has been reported that Si and Al can replace each other in Al_3Zr , resulting in a transformation from cubic $L1_2-Al_3Zr$ to tetragonal $DO_{22}-(Al, Si)_3Zr$ dispersoids[18]. In addition, Ti has been proven to have a certain degree of solubility in $(Al, Si)_3Zr$ [27, 28]. Therefore, it is reasonable to define the elongated dispersoids observed in this study as $DO_{22}-(Al, Si)_3(Zr, Ti)$ dispersoids [29]. It is worth noting that due to the relatively large size, only $DO_{22}-(Al, Si)_3(Zr, Ti)$ dispersoids and $\beta-Mg_2Si$ particles were revealed by OM and SEM (Figure 3.2 and 3.3), while the spherical dispersoids were too small to be detected, and they could only be observed with TEM (Figure 3.4 and 3.5).

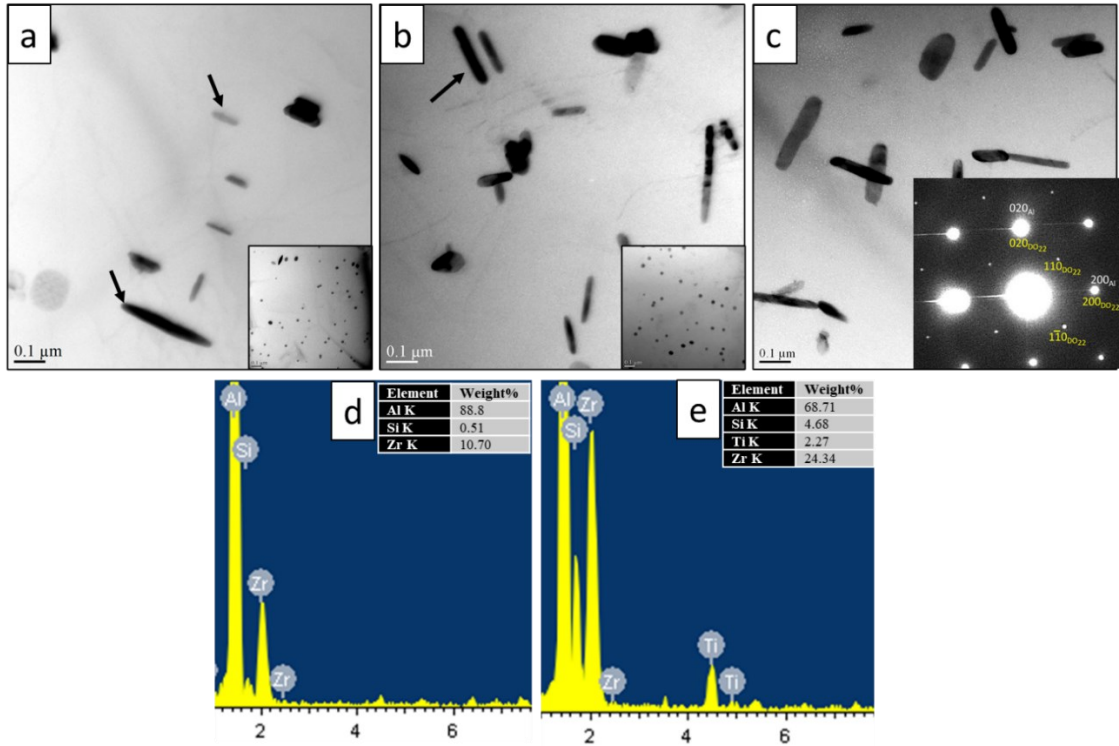


Figure 3.4. Bright-Field TEM images of (a) 0.4Si, (b) 0.7Si, and (c) 1.0Si alloys after homogenization at 550°C/5h and TEM-EDS analysis of (d) spherical and (e) elongated dispersoids.

TEM dark-field images were used to observe the evolution of spherical Al_3Zr dispersoids (Figure 3.5). This type of dispersoid was reported to precipitate with a large number density during low-temperature homogenization due to the high level of supersaturation of Zr in the matrix after solidification [30]. The SADP given in the inset of Figure 3.5c shows that this type of dispersoid has L_{12} cubic structure. It commonly exhibits a cube-to-cube orientation relationship with the aluminum matrix [31], and is coherent with the matrix [32]. While the elongated DO_{22} dispersoids are typically semi-coherent or incoherent with the matrix [33]. The precipitation behavior of the L_{12} dispersoids was obviously different from that of the DO_{22} dispersoids. While the smallest number density of

DO₂₂ was observed after homogenization at 450 °C (Figure 3.2), the largest number density of L₁₂-Al₃Zr was observed at the same temperature. With increasing the homogenization temperature, the number density of L₁₂ dispersoids significantly decreased, reaching a minimum value at 550 °C, while the dispersoid size increased. However, the change in the dispersoids number density with the temperature was dependent on the alloy composition. For instance, the 0.4Si alloy (Figure 3.5a) exhibited a lower number density after low-temperature homogenization (450 °C) as compared to the other two alloys (0.7Si (Figure 3.5d) and 1.0Si (Figure 3.5g)), indicating the positive effect of Si on promoting the precipitation of Al₃Zr. However, increasing the Si level resulted in reduced dispersoid stability at high-temperature homogenization. After homogenization at 550 °C, the 1.0Si alloy contained almost no spherical Al₃Zr dispersoids (Figure 3.5i), while the 0.4Si alloy still exhibited a reasonable number density of Al₃Zr dispersoids (Figure 3.5c).

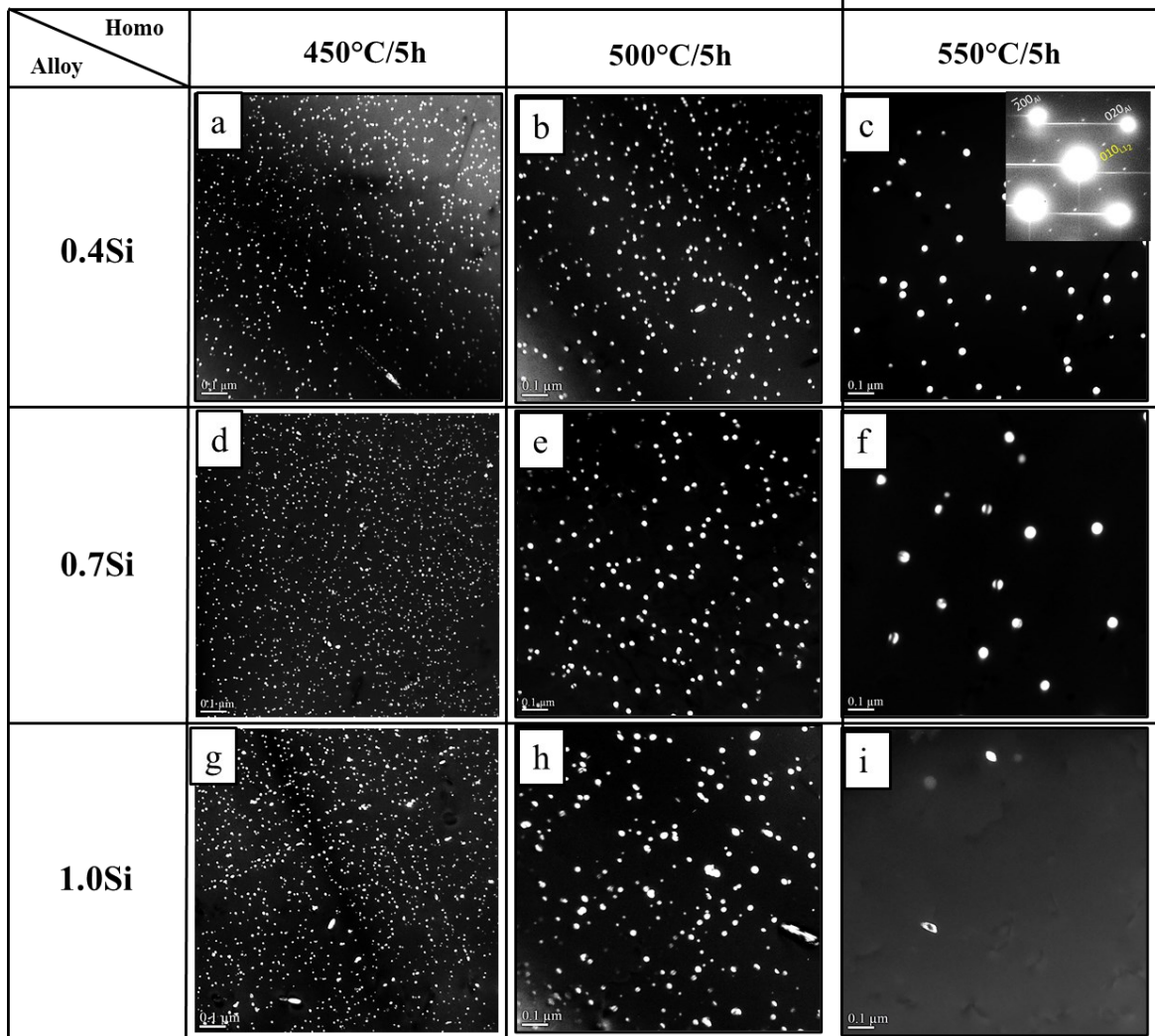


Figure 3.5 Dark-field TEM images for the spherical Al_3Zr dispersoids at different Si levels and homogenization temperatures.

From TEM and SEM observations, it is clear that at a given homogenization temperature, each alloy exhibits a different combination of spherical L_{12} and elongated DO_{22} dispersoids. Figure 3.6 shows the quantitative results in terms of the number density of both spherical and elongated dispersoids in each alloy for different homogenization conditions. Due to the spatial distribution of the dispersoids, the number densities of both spherical and elongated dispersoid were measured in the dispersoid zones where the majority of the

dispersoids were present. At 450°C, the number density of the spherical Al₃Zr increased from 3918 μm⁻³ for 0.4Si to 8880 μm⁻³ for 0.7Si but decreased to 5092 μm⁻³ for 1.0Si (Figure 3.6a). Increasing the homogenization temperature to 500 °C significantly decreased the number densities of the spherical Al₃Zr in all three alloys and decreased the differences between these densities. After homogenization at 550 °C, the number densities further decreased and reached their minimum values (240 μm⁻³ and 144 μm⁻³) for 0.4Si and 0.7Si, respectively, and there were almost no spherical dispersoids for 1.0 Si. In the case of the elongated DO₂₂-(Al,Si)₃(Zr,Ti) dispersoids (Figure 3.6b), at 450°C both 0.4Si and 0.7Si exhibited a low number density (~0.8 μm⁻²), but 1.0Si alloy almost doubled the number density (1.5 μm⁻²). This indicates that the transformation of spherical Al₃Zr to elongated DO₂₂-(Al,Si)₃(Zr,Ti) already occurred at low temperature, especially with 1.0Si. With increasing the temperature to 550 °C, the number densities of elongated dispersoids in 0.4Si and 0.7Si alloys slightly increased, while the number density in 1.0Si alloys remarkably increased, reaching its highest value of ~2.8 μm⁻² at the expense of Al₃Zr in both 500 °C and 550 °C, indicating that the high Si level (1.0%Si) strongly promoted the transformation from Al₃Zr to DO₂₂-(Al,Si)₃(Zr,Ti). In addition, the high homogenization temperature also favors this transformation.

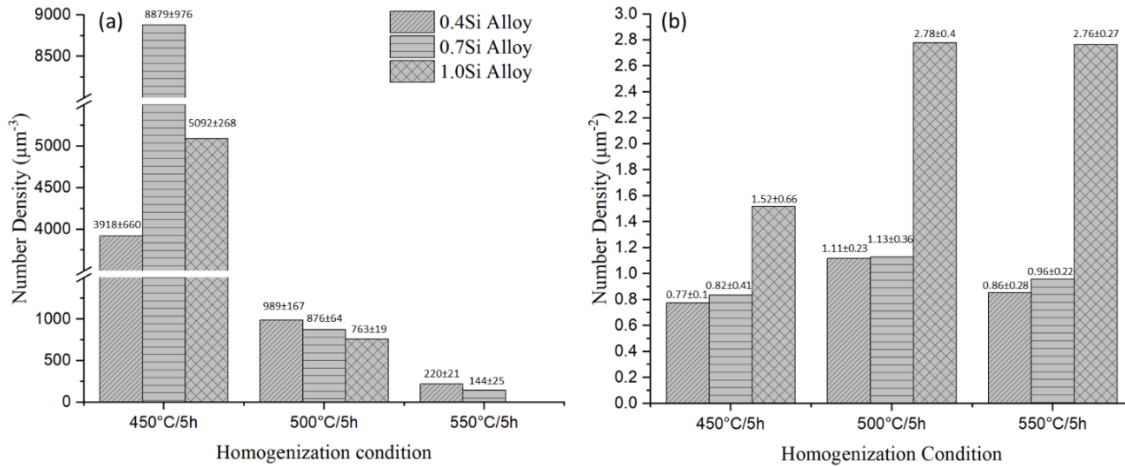


Figure 3.6 Number density of spherical dispersoids (a) and elongated dispersoids (b) for Si and homogenization variants

Figure 3.7 presents a schematic overview of the evolution of all precipitates across the range of Si contents. For a fixed Zr content, it is clear that Si can significantly affect the precipitation behavior of Zr-bearing dispersoids. It is reported that Si can enhance the Zr diffusion kinetics in the aluminum matrix [16], and hence accelerate the precipitation and transformation of Zr-bearing dispersoids. In addition, Mg was reported to increase the supersaturation of Zr in Al matrix which could enhance the nucleation of Zr-dispersoids [34]. At the lowest homogenization temperature (450 °C), large β - Mg_2Si and DO_{22} - $(\text{Al},\text{Si})_3(\text{Zr},\text{Ti})$ particles precipitated at the cell and grain boundaries where a high level of Si and Mg exist because of their segregation behavior. While fine Al_3Zr precipitated at cells/grain centers, forming dispersoid free zones (DFZs) close to cell and grain boundaries. For the 0.4Si alloy, the precipitation of spherical Al_3Zr dispersoids was quite sluggish, so the number density of Al_3Zr was relatively low with large DFZs. With increasing the Si to 0.7%, a remarkable increase in the precipitation of Al_3Zr dispersoids was observed, which was driven by the strong nucleation provided by Si atom clusters [35], resulting in a much higher number

density of Al_3Zr (Figure 3.6a) and narrow DFZs. At the highest level of Si (1.0%), the Al_3Zr dispersoids co-existed with a large number density of $\text{DO}_{22}\text{-(Al, Si)}_3\text{(Zr, Ti)}$ dispersoids inside the cell/grain due to the transformation of dispersoids. In addition, the high concentration of Si and Mg promoted the nucleation rate near the boundary areas where Zr concentration is lowest, resulting in the narrowest DFZs.

During high-temperature homogenization (550 °C), $\beta\text{-Mg}_2\text{Si}$ particles in the cell/grain boundaries were completely dissolved, which provided more silicon to promote the precipitation of $\text{DO}_{22}\text{-(Al, Si)}_3\text{(Zr, Ti)}$. In 0.4Si and 0.7Si alloys, the elongated DO_{22} dispersoids were mainly concentrated at the cell/grain boundaries, while Al_3Zr dispersoids were located inside grains. Because of the increased Zr diffusion rate and associated coarsening at high temperatures, the Al_3Zr dispersoids were coarser with a lower number density than those formed after low-temperature homogenization. For the high Si alloy (1.0Si), a complete transformation of dispersoids was observed, resulting in the disappearance of $\text{L1}_2\text{-Al}_3\text{Zr}$ and a uniform distribution of 100% elongated DO_{22} dispersoids in the matrix. In general, the nonhomogeneous distribution of each precipitate (Figure 3.7) is mainly related to the different segregation behavior of Zr, Si and Mg during solidification. For instance, Zr tends to be segregated and enriched inside the aluminum cell and grain as a consequence of the peritectic reaction in the Al-Zr system [36]. Therefore, the $\text{L1}_2\text{-Al}_3\text{Zr}$ dispersoids tend to be localized at such regions where a high level of Zr supersaturation exists. Conversely, the depletion of Zr towards the boundary results in DFZ formation. On the other hand, Si and Mg tends to segregate near grain boundaries during solidification and has a relatively high diffusion rate [26]. Hence, $\beta\text{-Mg}_2\text{Si}$ particles and $\text{DO}_{22}\text{-(Al, Si)}_3\text{(Zr, Ti)}$ dispersoids precipitate preferentially near grain boundaries. However, at the highest Si level

and highest homogenization temperature (1.0%Si at 550 °C), DO₂₂ dispersoids were predominant, producing a uniform distribution of elongated dispersoids in the matrix.

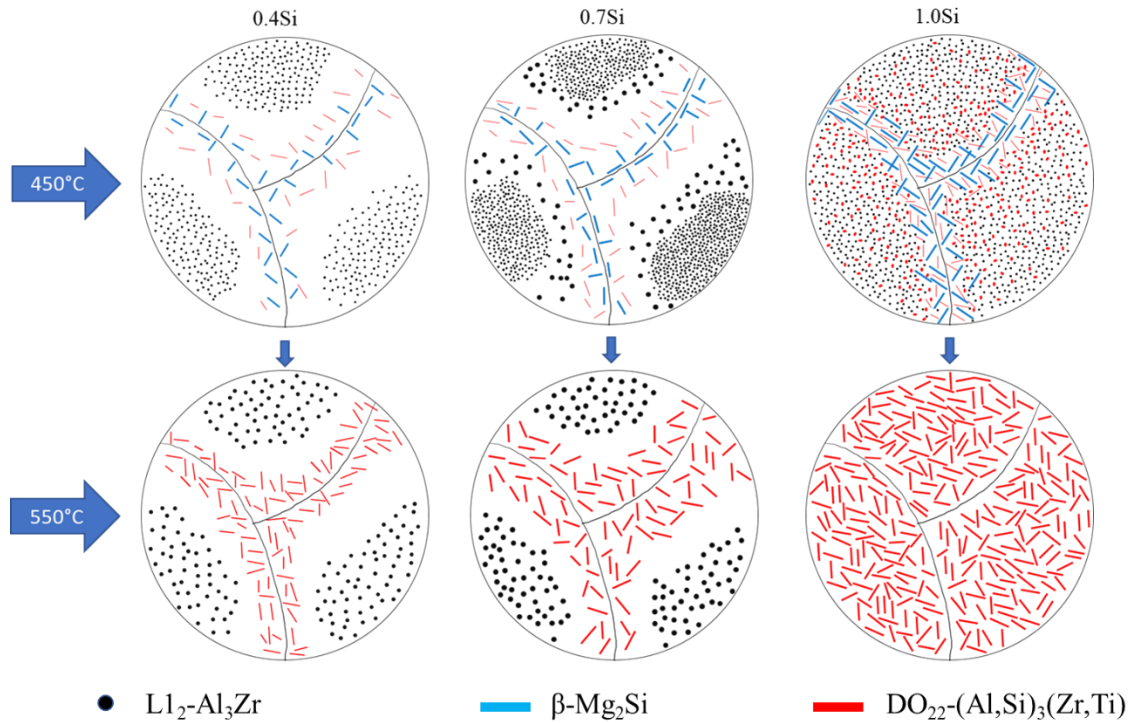


Figure 3.7 Schematic illustration of the evolution of Zr-bearing dispersoids, β-Mg₂Si and DFZs in different alloys during low- and high-temperature homogenization.

3.3.3. Hot deformation behavior

3.3.3.1. Flow stress

Figure 3.8 shows typical true stress-strain curves obtained in different Z conditions for the three alloys under different homogenization conditions. For all conditions, there is a sharp increase in the flow stress in the initial stage of compression until reaching the peak flow stress owing to strong work hardening. Subsequently, the softening mechanisms affected the flow stress curves with further deformation, which are dependent on the deformation

condition, alloy composition and homogenization condition. The flow stress curves exhibited three trends: (1) a slow but continuous increase of the flow stress with increasing strain (arrow A), indicating the dominant effect of work hardening; (2) a steady-state (arrow B) where a plateau in the flow stress occurred, which is attributed to a dynamic balance between the work hardening and softening; (3) a decline of the flow stress with increasing strain (arrow C), indicating the dominant effect of softening mechanisms. The 0.4Si alloy exhibited a continuous increase of the flow stress during high Z deformation (350 °C, 1.0 s⁻¹), indicating the dominant effect of work hardening rather than softening, while it exhibited steady state flow stress curves in the medium and high Z conditions regardless of the homogenization conditions. On the other hand, 0.7Si and 1.0Si alloys showed a slight dependency on the homogenization condition. For example, homogenization at 450 °C resulted in more work hardening as compared to higher temperatures, particularly at 550 °C. This effect was more apparent at high Z (350 °C, 1.0 s⁻¹) but reduced significantly at low Z (450 °C, 0.001s⁻¹). Such different behaviors are mostly related to the interactions between the dislocations and dispersoids during hot deformation. The high density of fine nanoscale Al₃Zr dispersoids that precipitated at low homogenization temperature appeared to be more effective to hinder the dislocation movement compared to large elongated DO₂₂-(Al, Si)₃(Zr,Ti) dispersoids that precipitated at 550°C.

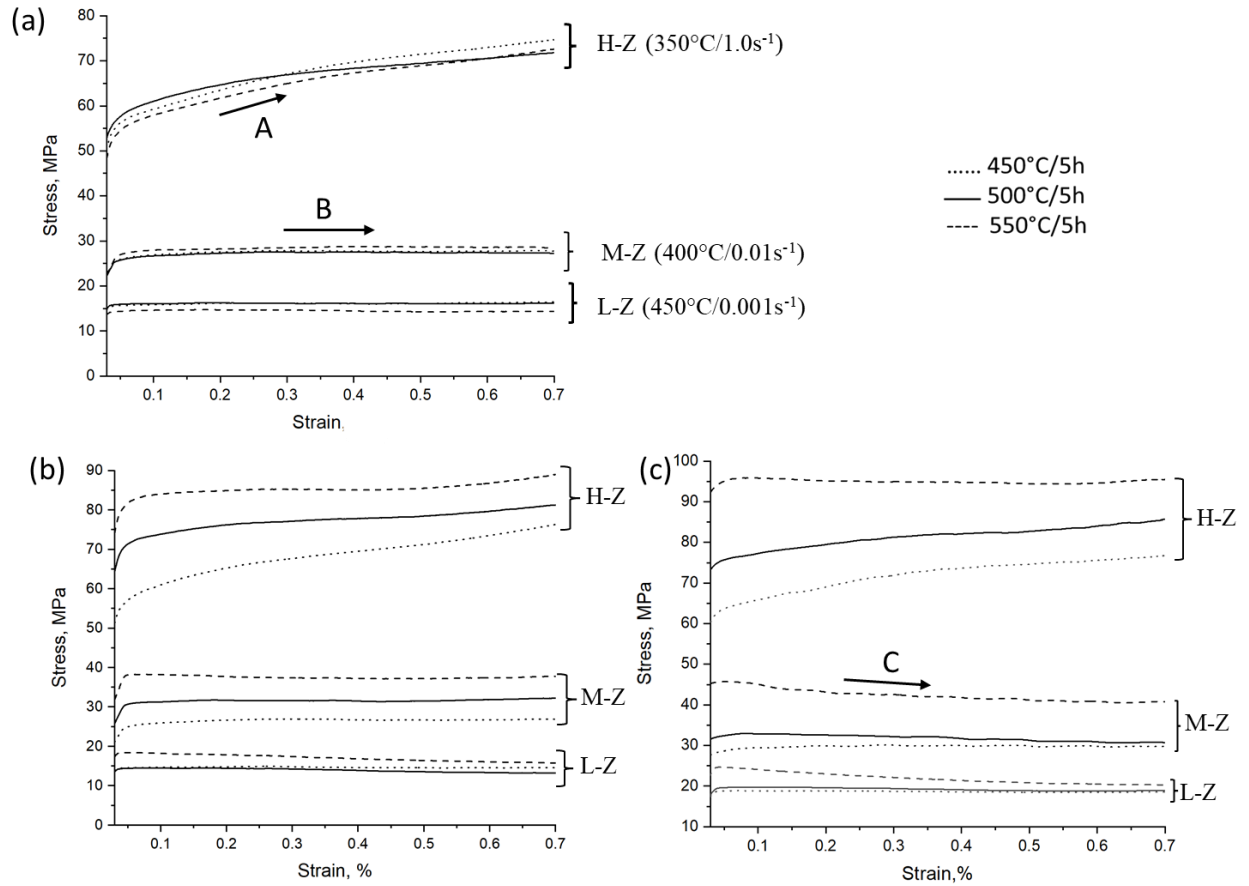


Figure 3.8 Typical flow curves in different Z conditions for (a) 0.4Si, (b) 0.7Si and (c) 1.0Si alloys under different homogenization conditions.

It can be seen from Figure 3.8 that the flow stress was primarily dependent on the hot deformation conditions (Z parameter). The higher the Z value, the higher is the flow stress. The highest flow stress was achieved in the high Z condition, where the temperature is relatively low (350 °C), and the strain rate is high (1.0 s⁻¹). By increasing the temperature to 450 °C and decreasing the strain rate to 0.001S⁻¹ (low Z), the flow stresses significantly decreased. This is because the higher temperature facilitates the movement and annihilation of dislocations, while the lower strain rate provides sufficient time for the accumulation of activation energy [37, 38]. Figure 3.9 shows the flow stress values at high Z for the three

alloys under different homogenization conditions, demonstrating the effect of alloy composition on the flow stress. For the samples homogenized at 450 °C, the flow stress slightly increased with increasing Si from 0.4% to 1.0%. With increasing homogenization temperature, a significant increase in the flow stress could be observed from 0.4%Si to 1.0%Si. Notably, after homogenization at 550 °C, the flow stress increased from 73 MPa (0.4Si alloy) to 89 MPa (0.7Si alloy) and further to 95.6 MPa for the 1.0Si alloy. Figure 3.10 shows the results of electrical conductivity (EC) measurements, which indicated the solid solution level of alloying elements (mainly Si and Mg) for each alloy. The EC decreases considerably with increasing Si content. A higher electrical conductivity corresponds to a lower solid solution level and vice-versa. By Comparing Figure 3.9 with Figure 3.10, it is reasonable to assume that the flow stress increase is closely related to the solid solution level of Si and Mg in the aluminum matrix. It is clear that the 0.4Si alloy has the lowest solid solution level, while the 1.0Si alloy exhibits the highest solid solution level for all homogenization conditions. Correspondingly, the 0.4Si alloy exhibited the lowest flow stress, while the 1.0Si alloy produced the highest flow stress (Figure 3.9).

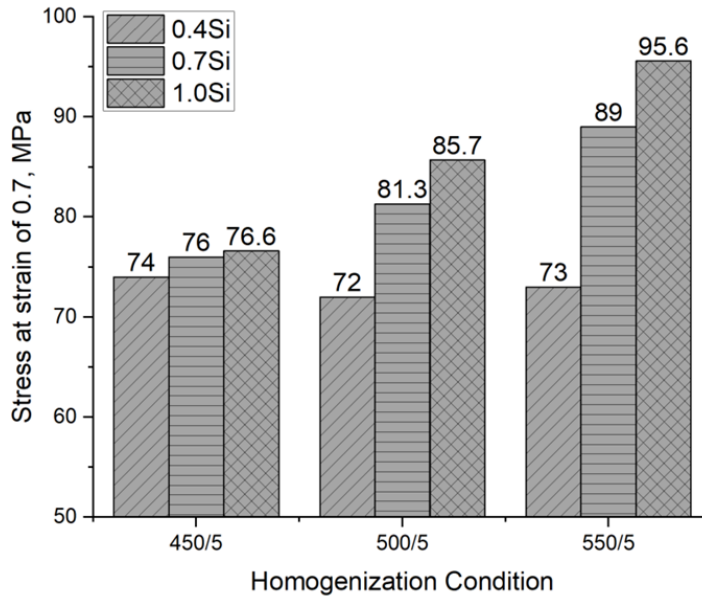


Figure 3.9 Flow stress at a strain of 0.7 in the high Z condition for the Si and homogenization variants.

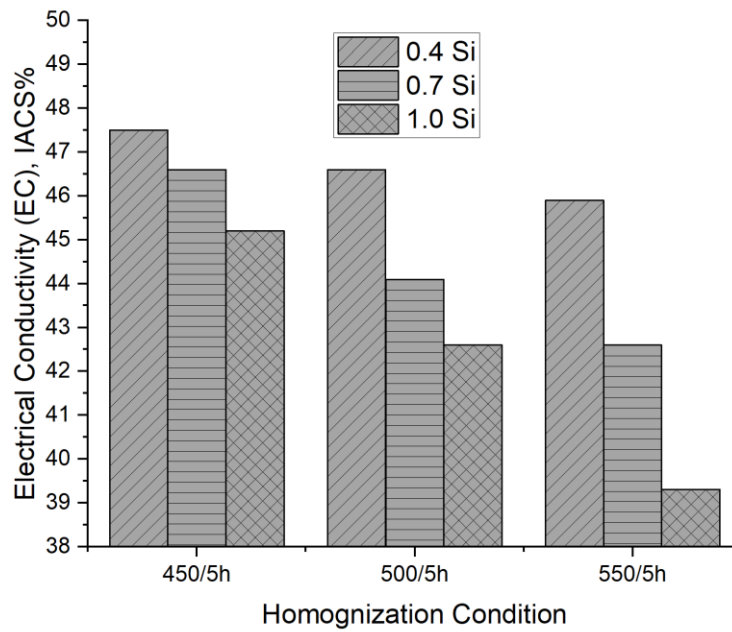


Figure 3.10 Electrical conductivity for the Si and homogenization variants.

3.3.3.2. *Microstructure evolution during deformation*

To study the microstructure evolution during deformation, samples homogenized at 450 °C, and 550 °C were selected for investigation by the EBSD technique. Figure 3.11 shows All-Euler maps for the three Si contents after compression testing in the high Z condition, while Figure 3.12 displays All-Euler maps obtained in the low Z condition. A quantitative analysis of misorientation angle fractions was also performed, and the results are presented in Figure 3.13. In general, the three alloys showed quite similar deformed microstructures, exhibiting elongated grains perpendicular to the deformation direction.

In the high Z condition, a high number density of low and medium angle boundaries inside the elongated grains was observed, indicating a low dynamically recovered structure. The samples homogenized at high temperature (550 °C) exhibited a higher fraction of low angle boundaries for all alloys (Figure 3.13). This is more apparent in the case of 1.0Si, which showed a low angle boundary fraction of 54% for 450 °C against 62% for 550 °C. Such results agree with the flow stress values shown in Figure 3.9, where higher flow stress at high-Z condition was observed for the samples homogenized at 550 °C. The high level of solutes at 550 °C may hinder the dislocation movement and create pile-ups [39], which in turn reduces the rate of dynamic recovery and increases the fraction of low angle boundaries. On the other hand, no significant difference was observed between the low- and high-temperature homogenization conditions for the 0.4Si alloy. In addition, some tiny, recrystallized grains (white arrows) were observed in the 0.7Si and 1.0Si alloys shown in Figure 3.11b and C, respectively. These newly grains were observed close to the grain boundaries where large intermetallic particles that may cause unstable deformation in the surrounding area. The homogenization at a low temperature (450 °C) was insufficient to

dissolve large primary Mg_2Si particles, especially for 1.0Si, which has a large amount of these particles. the existence of large intermetallic particles and DFZs along grain boundaries promote the recrystallization to occur [40]

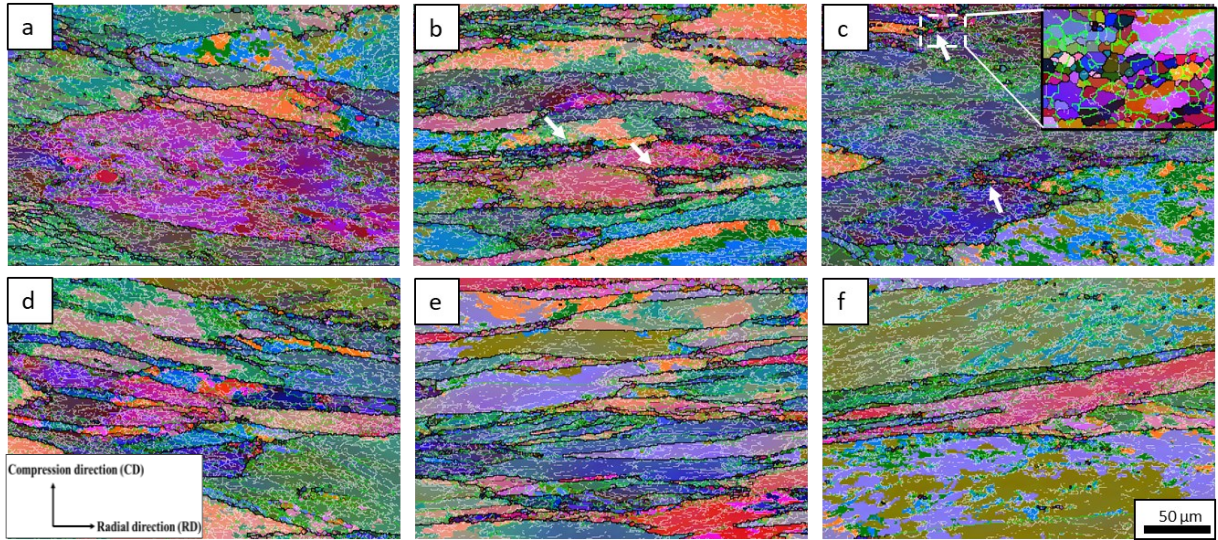


Figure 3.11 All-Euler orientation maps of as-deformed structures in the high Z condition ($350\text{ }^{\circ}\text{C}, 1.0\text{ s}^{-1}$) for: (a, d) 0.4Si, (b, e) 0.7Si and (c, f) 1.0Si alloys homogenized at (a-c) $450\text{ }^{\circ}\text{C}/5\text{h}$ and (d-f) $550\text{ }^{\circ}\text{C}/5\text{h}$. Low angle (2° - 5°), medium angle (6° - 15°), and high angle boundaries ($>15^{\circ}$) were represented by white, green, and black lines, respectively.

On the other hand, in the low Z deformation condition ($450\text{ }^{\circ}\text{C}, 0.001\text{ s}^{-1}$), the substructure densities were significantly reduced with neatly organized boundaries within the elongated grains as an indication of an increasing level of DRV (Figure 3.12). A significant reduction of low angle boundaries was observed along with a significant increase in the fraction of medium and high angle boundaries relative to those at high Z (Figure 3.13). It is known that high deformation temperature facilitates the migration of sub-grain and grain boundaries by accelerating the dislocation annihilation and rearrangement through climb and glide, resulting in a high rate of DRV [41]. Also, the lower strain rate allows more time for

subgrain coalescence and growth. In the same deformation condition, the 0.4Si and 0.7Si exhibited similar fractions of low and medium angle boundaries, while the 1.0Si showed higher fractions of low and medium angle boundaries, indicating more restriction for boundary migration, and hence a lower DRV rate.

Regarding the effect of the homogenization temperature, 0.4Si showed almost the same structure in terms of the fraction of different grain boundaries for homogenization at 450 °C and 550 °C. Meanwhile, a slight difference was observed in 0.7Si alloy with a fraction of low and medium angle boundaries of 80% and 84% for homogenization at 450 °C and 550 °C, respectively. However, an apparent difference between the different homogenization conditions was exhibited by 1.0Si with a fraction of low and medium angle boundaries of 83% vs. 92% for homogenization at 450 °C and 550 °C, respectively. Such results are also in conformity with the flow stress obtained at low Z, where the highest values were achieved by the samples homogenized at 550 °C, particularly for 1.0Si.

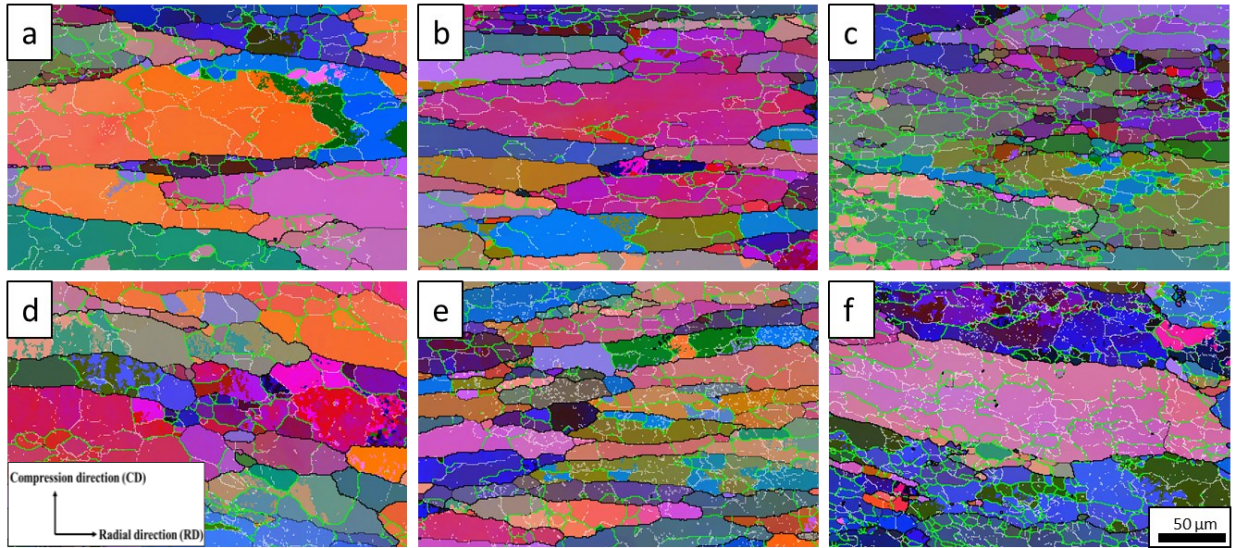


Figure 3.12 All-Euler orientation maps of as-deformed structures in the low Z condition ($450^{\circ}\text{C}, 0.001\text{ s}^{-1}$) for: (a, d) 0.4Si, (b, e) 0.7Si and (c, f) 1.0Si alloys homogenized at (a-c) $450^{\circ}\text{C}/5\text{h}$ and (d-f) $550^{\circ}\text{C}/5\text{h}$. Low angle (2° - 5°), medium angle (6° - 15°), and high angle boundaries ($>15^{\circ}$) were represented by white, green, and black lines, respectively.

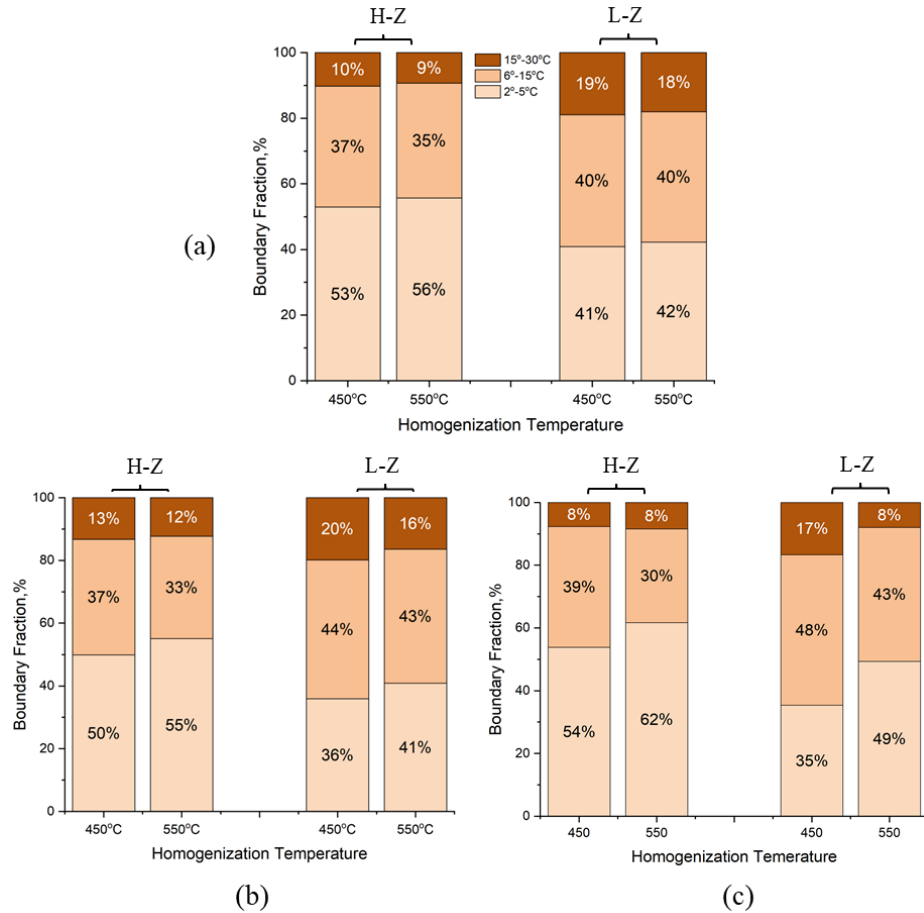


Figure 3.13 Misorientation angle fractions after deformation at high Z and low Z (a) 0.4Si, (b) 0.7Si and (c) 1.0Si alloys homogenized at different temperatures.

3.3.3.3 Recrystallization resistance during post-deformation annealing

The samples homogenized at 450 °C and 550 °C and deformed in the high Z condition (350 °C, 1.0 s⁻¹) were selected to evaluate the recrystallization resistance at two different annealing temperatures 500 °C and 540 °C for 1h holding time because such samples possessed similar microstructure (deformed and less recovered) as the starting microstructure (Figure 3.10). Figures 3.14 and 3.15 show All-Euler EBSD maps after annealing at 500 °C and 540 °C, respectively. In addition, the recrystallized area fractions for each condition were quantitatively analyzed, and the results are shown in Figure 3.16. After 500 °C annealing, a

partially recrystallized microstructure with some newly formed grains was observed in all alloys (Figure 3.14). These new grains were characterized by high angle boundaries and were free of internal substructures. The recrystallized grains were found to be preferentially nucleated and grown along grain boundaries where the dispersoid-free zones are located. In general, the samples homogenized at 450 °C (Figure 3.14a-c) exhibited much lower recrystallized fractions compared to the samples homogenized at 550 °C (Figure 3.14d-f), for instance, 8-30% recrystallized fraction at 450 °C homogenization vs. 28-63% recrystallized fraction at 550 °C homogenization (Figure 3.16). Furthermore, at a given homogenization temperature, the 1.0Si exhibited the highest recrystallization resistance compared to the other two alloys (0.4Si and 0.7Si). For instance, only 8.3% and 28% recrystallized area fractions were measured for homogenization at 450 °C and 550 °C respectively, while the other two alloys (0.4Si and 0.7Si) exhibited much higher values (Figure 3.16).

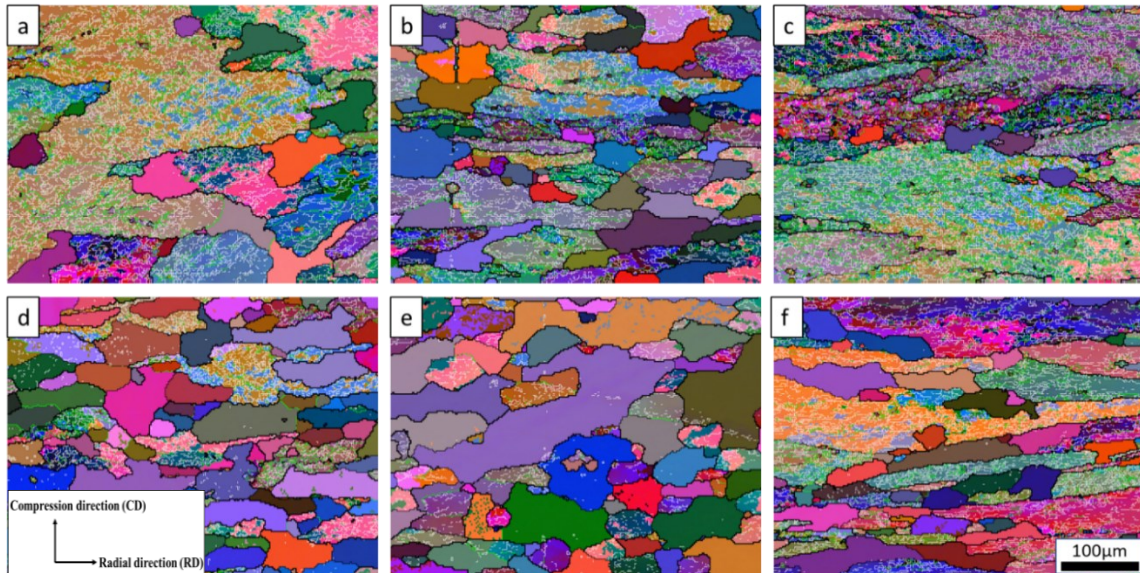


Figure 3.14 All-Euler orientation maps after annealing at 500°C/1h for: (a, d) 0.4Si, (b, e) 0.7Si and (c, f) 1.0Si alloys homogenized at (a-c) 450°C/5h and (d-f) 550°C/5h.

Increasing the annealing temperature to 540 °C resulted in a significant increase in the recrystallized fraction (>50%) for all conditions, as shown in Figure 3.15. The high annealing temperature provides more thermal activation energy for dislocations to move and bypass the obstacles, and hence the recrystallization can easily propagate. Compared to annealing at 500 °C, the samples homogenized at 450 °C (Figure 3.15a-c) still had lower recrystallized fractions relative to the samples homogenized at 550°C (Figure 3.15d-f), but the difference in recrystallization fractions was reduced (Figure 3.16). Again, the 1.0Si exhibited the lowest recrystallization fraction among the three alloys under both homogenization conditions.

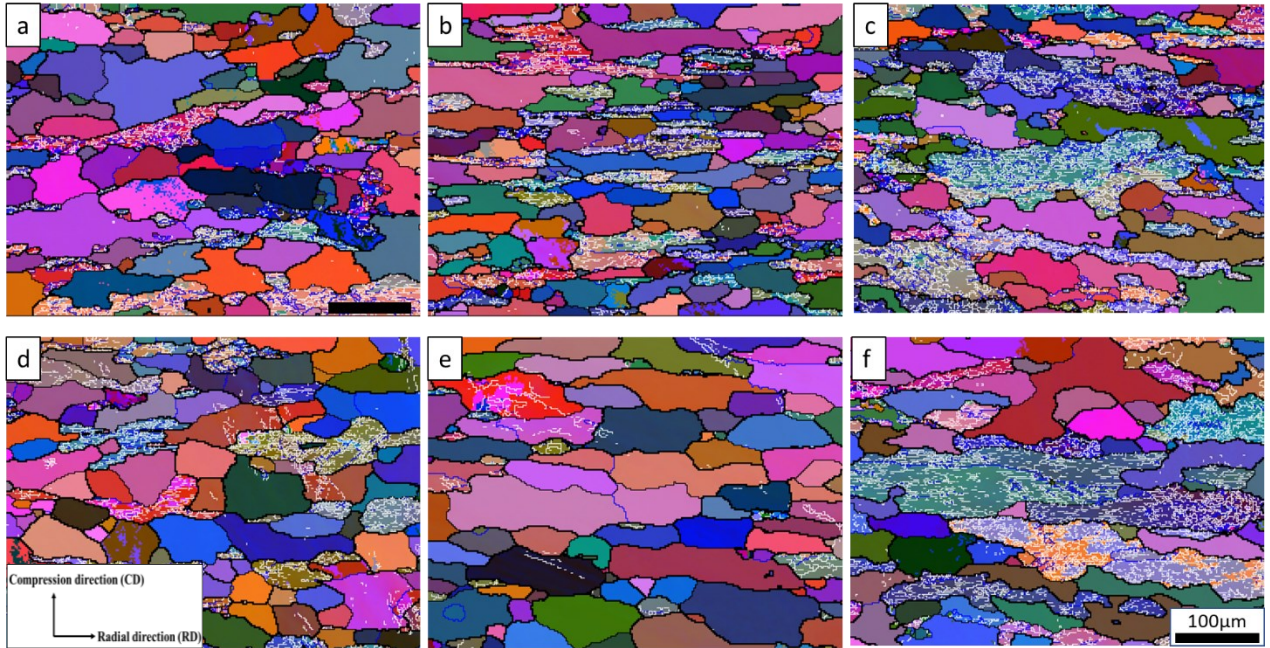


Figure 3.15 All-Euler orientation maps after annealing at 540°C/1h for: (a, d) 0.4Si, (b, e) 0.7Si and (c, f) 1.0Si alloys homogenized at (a-c) 450°C/5h and (d-f) 550°C/5h.

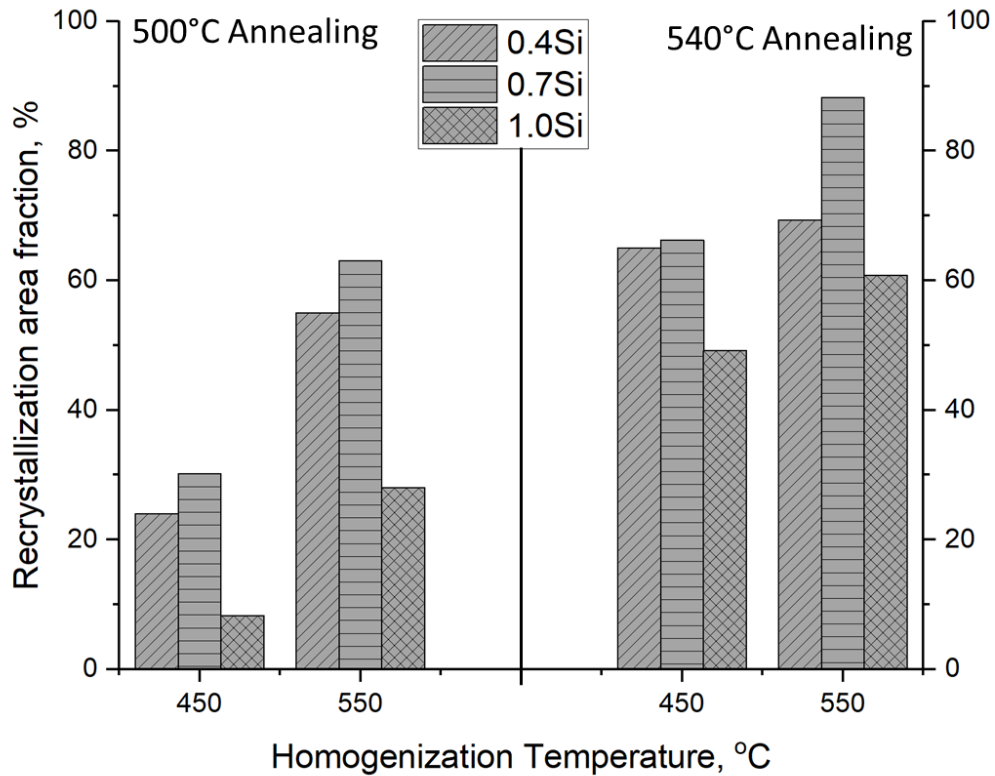


Figure 3.16 Recrystallization area fractions after annealing at 500°C/1h and 540°C/1h for Si and homogenization variants.

The EBSD results show that both alloy composition and homogenization condition have a significant impact on the static recrystallization during post-deformation annealing. These mainly relate to the precipitation of Zr-bearing dispersoids (L_{12} and DO_{22}) during homogenization which affects the migration of grain boundaries through the Zener drag forces. The pinning efficiency of such dispersoids is determined by their size, number density, and distribution. After annealing at 500 °C, the samples homogenized at 450 °C exhibited low recrystallized fractions (Figure 3.16). The fine dense L_{12} - Al_3Zr dispersoids precipitated during low-temperature homogenization were reported to have better

performance on static recrystallization inhibition compared to the large elongated DO₂₂ dispersoids [42].

On the other hand, the distribution of dispersoids and the dispersoids free zone (DFZ) are critical to provide an even pinning effect across the grains [43]. The 0.4Si and 0.7Si alloys exhibited a non-uniform distribution of Al₃Zr dispersoids and large DFZs with limited large elongated dispersoids (Figure 3.7). Therefore, some areas were adjacent to grain boundaries without dispersoids, giving a locally reduced pinning effect. In contrast, the 1.0Si alloy showed a uniform distribution of Al₃Zr and/or DO₂₂-(Al,Si)₃(Zr,Ti) dispersoids within the grain interior and very limited DFZs at grain boundaries, resulting in an efficient and uniform pinning effect across the microstructure. Consequently, it exhibited the best recrystallization resistance among the three alloys studied.

By increasing the annealing temperature to 540 °C, higher thermal activation energy was provided, resulting in a higher level of recrystallization in all conditions. Similar to annealing at 500 °C, less recrystallization occurred in the case of low-temperature homogenization (450 °C). However, the difference between low and high-temperature homogenization for the same alloy was significantly reduced (Figure 3.16). One reason is that the high-temperature annealing could also promote the transformation of the dispersoids from L1₂ to DO₂₂. A part of L1₂-Al₃Zr dispersoids formed during low-temperature homogenization (450 °C) would transform to DO₂₂-(Al,Si)₃(Zr,Ti). This would result in a similar pinning effect to that produced at high temperature (550 °C).

3.4. Conclusions

The evolution of Zr-bearing dispersoids in 6xxx alloys with a range of Si levels and the effect of these dispersoids on the hot deformation and recrystallization resistance have been studied under different homogenization conditions. The following conclusions can be drawn:

- (1) Two types of Zr-bearing dispersoids were mainly observed depending on the alloy composition and homogenization condition: fine spherical $L1_2\text{-Al}_3\text{Zr}$ and large elongated $\text{DO}_{22}\text{-(Al,Si)}_3\text{(Zr,Ti)}$ dispersoids.
- (2) The precipitation of $L1_2\text{-Al}_3\text{Zr}$ dispersoids occurred primarily at low homogenization temperatures. Increasing Si content and homogenization temperature promoted the transformation of $L1_2\text{-Al}_3\text{Zr}$ to $\text{DO}_{22}\text{-(Al,Si)}_3\text{(Zr,Ti)}$. For the highest Si content and temperature (1.0%Si at 550 °C), the elongated DO_{22} dispersoids were predominant.
- (3) The flow stress was controlled by the solid solution level of major alloy addition (Mg,Si) and hot deformation parameters rather than by the dispersoid characteristics, and hence the flow stress increased with the Si level.
- (4) The fine $L1_2\text{-Al}_3\text{Zr}$ dispersoids with a high number density formed during low-temperature homogenization resulted in higher recrystallization resistance during post-deformation annealing compared to the large $\text{DO}_{22}\text{-(Al,Si)}_3\text{(Zr,Ti)}$ dispersoids.
- (5) The high Si alloy (1.0%) exhibited superior recrystallization resistance during post-deformation annealing as compared to the low silicon alloys (0.4-0.7%), regardless of the homogenization condition. This was attributed to the more uniform distribution of dispersoids and minimal dispersoid-free zones.

References

1. Reiso, O., *Extrusion of AlMgSi alloys*. Materials Forum, 2004. **28**: p. 32-46.
2. Poznak, A., D. Freiberg, and P. Sanders, *Chapter 10 - Automotive Wrought Aluminium Alloys*, in *Fundamentals of Aluminium Metallurgy*, R.N. Lumley, Editor. 2018, Woodhead Publishing. p. 333-386.
3. Cai, M. and G.J. Cheng, *Microstructure-properties relationship in two Al-Mg-Si alloys through a combination of extrusion and aging*. Jom, 2007. **59**(8): p. 58-61.
4. Birol, Y., *Effect of Cr and Zr on the grain structure of extruded EN AW 6082 alloy*. Metals and Materials International, 2016. **20**(4): p. 727-732.
5. Poletti, C., T. Wójcik, and C. Sommitsch, *Hot Deformation of AA6082 Containing Fine Intermetallic Particles*. Metallurgical and Materials Transactions A: Physical Metallurgy and Materials Science, 2012. **44**(3): p. 1577-1586.
6. Li, C., K. Liu, and Chen, X.G, *Improvement of elevated-temperature strength and recrystallization resistance via Mn-containing dispersoid strengthening in Al-Mg-Si 6082 alloys*. Journal of Materials Science & Technology, 2020. **39**: p. 135-143.
7. Zhang, G.W., et al., *Effects of Mn and Cr Additions on the Recrystallization Behavior of Al-Mg-Si-Cu Alloys*. Materials Science Forum, 2017. **877**: p. 172-179.
8. Guo, Z., G. Zhao, and Chen, X.G, *Effects of two-step homogenization on precipitation behavior of Al₃Zr dispersoids and recrystallization resistance in 7150 aluminum alloy*. Materials Characterization, 2015. **102**: p. 122-130.
9. Ding, Y., et al., *The recrystallization behavior of Al-6Mg-0.4Mn-0.15Zr-xSc (x = 0.04–0.10 wt%) alloys*. Materials Characterization, 2019. **147**: p. 262-270.
10. Knipling, K.E., D.C. Dunand, and D.N. Seidman, *Precipitation evolution in Al-Zr and Al-Zr-Ti alloys during aging at 450–600°C*. Acta Materialia, 2008. **56**(6): p. 1182-1195.

11. Deng, Y.-l., et al., *Three-Stage Homogenization of Al-Zn-Mg-Cu Alloys Containing Trace Zr*. Metallurgical and Materials Transactions A: Physical Metallurgy and Materials Science, 2013. **44**(6): p. 2470-2477.
12. Guo, Z., G. Zhao, and Chen, X.G, *Effects of homogenization treatment on recrystallization behavior of 7150 aluminum sheet during post-rolling annealing*. Materials Characterization, 2016. **114**: p. 79-87.
13. Meng, Y., et al., *Effect of Zr on microstructures and mechanical properties of an AlMgSiCuCr alloy prepared by low frequency electromagnetic casting*. Materials Characterization, 2014. **92**: p. 138-148.
14. Babaniaris, S., et al., *Effect of Al₃(Sc,Zr) dispersoids on the hot deformation behaviour of 6xxx-series alloys: A physically based constitutive model*. Materials Science and Engineering A, 2020. **793**.
15. Wolverton, C., *Solute–vacancy binding in aluminum*. Acta Materialia, 2007. **55**(17): p. 5867-5872.
16. Vo, N.Q., D.C. Dunand, and D.N. Seidman, *Role of silicon in the precipitation kinetics of dilute Al-Sc-Er-Zr alloys*. Materials Science and Engineering A, 2016. **677**: p. 485-495.
17. Gao, T., et al., *Precipitation behaviors of cubic and tetragonal Zr-rich phase in Al-(Si-)Zr alloys*. Journal of Alloys and Compounds, 2016. **674**: p. 125-130.
18. Litynska, L., et al., *TEM and HREM study of Al₃Zr precipitates in an Al-Mg-Si-Zr alloy*. J Microsc, 2006. **223**(Pt 3): p. 182-4.
19. Chamanfar, A., et al., *Analysis of flow stress and microstructure during hot compression of 6099 aluminum alloy (AA6099)*. Materials Science and Engineering A, 2019. **743**: p. 684-696.
20. Liu, S., et al., *Characterization of hot deformation behavior and constitutive modeling of Al–Mg–Si–Mn–Cr alloy*. Materials Science, 2019. **54**(5): p. 4366-4383.

21. McQueen, H.J., et al., *Hot Deformation and Processing of Aluminum Alloys*. 2016: CRC Press. 1-564.
22. Rollett, A., G.S. Rohrer, and J. Humphreys, *Recrystallization and related annealing phenomena*. 2017: Newnes.
23. Andersen, S., H. Zandbergen, and J. Jansen, *Tr holt C, Tundal U, Reiso O*. Acta Mater, 1998. **46**: p. 3283.
24. Marioara, C.D., et al., *The influence of temperature and storage time at RT on nucleation of the β'' phase in a 6082 Al–Mg–Si alloy*. Acta Materialia, 2003. **51**(3): p. 789-796.
25. Allen, S.M., *Foil thickness measurements from convergent-beam diffraction patterns*. Philosophical Magazine A, 1981. **43**(2): p. 325-335.
26. Seo, H., et al., *Solidification and segregation behaviors in 6061 aluminum alloy*. Metals and Materials International, 2013. **19**: p. 433-438.
27. Tsunekawa, S. and M.E. Fine, *Lattice parameters of Al_3 (Zr_xTi_{1-x}) vs. x in Al-2 at.% (Ti + Zr) alloys*. Scripta Metallurgica, 1982. **16**: p. 391-392.
28. Jia, Z.-H., et al., *Precipitation behaviour of Al_3Zr precipitate in Al–Cu–Zr and Al–Cu–Zr–Ti–V alloys*. Transactions of Nonferrous Metals Society of China, 2012. **22**(8): p. 1860-1865.
29. Sato, T., A. Kamio, and G.W. Lorimer, *Effects of Si and Ti Additions on the Nucleation and Phase Stability of the L12-Type Al_3Zr Phase in Al-Zr Alloys*. Materials Science Forum, 1996. **217-222**: p. 895-900.
30. Mikhaylovskaya, A.V., et al., *Precipitation behavior of L12 Al_3Zr phase in Al-Mg-Zr alloy*. Materials Characterization, 2018. **139**: p. 30-37.
31. Zupanič, F., et al., *Quasicrystalline and L12 precipitates in a microalloyed Al-Mn-Cu alloy*. Materials Today Communications, 2020. **22**: p. 100809.

32. Ashby, M.F. and L.M. Brown, *Diffraction contrast from spherically symmetrical coherency strains*. Philosophical Magazine A, 2006. **8**(91): p. 1083-1103.
33. Schmid, F., et al., *Synergistic alloy design concept for new high-strength Al–Mg–Si thick plate alloys*. Materialia, 2021. **15**: p. 100997.
34. Robson, J.D. and P.B. Prangnell, *Modelling Al₃Zr dispersoid precipitation in multicomponent aluminium alloys*. Materials Science and Engineering: A, 2003. **352**(1-2): p. 240-250.
35. Wu, S.H., et al., *Effect of Si addition on the precipitation and mechanical/electrical properties of dilute Al–Zr–Sc alloys*. Materials Science and Engineering: A, 2021. **812**: p. 141150.
36. Jia, Z., et al., *Effect of homogenization and alloying elements on recrystallization resistance of Al–Zr–Mn alloys*. Materials Science and Engineering A, 2007. **444**(1-2): p. 284-290.
37. Kai, X., et al., *Hot deformation behavior and optimization of processing parameters of a typical high-strength Al–Mg–Si alloy*. Materials and Design, 2016. **90**: p. 1151-1158.
38. Ezatpour, H.R., et al., *Investigation of work softening mechanisms and texture in a hot deformed 6061 aluminum alloy at high temperature*. Materials Science and Engineering A, 2014. **606**: p. 240-247.
39. Qian, X., N. Parson, and Chen, X.G, *Effect of post-homogenisation cooling rate and Mn addition on Mg₂Si precipitation and hot workability of AA6060 alloys*. Canadian Metallurgical Quarterly, 2020. **59**(2): p. 189-200.
40. Qian, X., N. Parson, and Chen, X.G, *Effects of Mn content on recrystallization resistance of AA6082 aluminum alloys during post-deformation annealing*. Journal of Materials Science & Technology, 2020. **52**: p. 189-197.

41. Liu, S.H., et al., *Microstructure evolution and physical-based diffusion constitutive analysis of Al-Mg-Si alloy during hot deformation*. Materials and Design, 2019. **184**: p. 108181.
42. Elasheri, A., et al., *Evolution of Zr-Bearing Dispersoids during Homogenization and Their Effects on Hot Deformation and Recrystallization Resistance in Al-0.8%Mg-1.0%Si Alloy*. Journal of Materials Engineering and Performance, 2021. **30**(10): p. 7851-7862.
43. Wu, L.-M., et al., *Effects of homogenization treatment on recrystallization behavior and dispersoid distribution in an Al-Zn-Mg-Sc-Zr alloy*. Journal of Alloys and Compounds, 2008. **456**(1): p. 163-169.

CHAPTER 4: Improving the dispersoid distribution and recrystallization resistance of a Zr-containing 6xxx alloy using two-step homogenization

(Published in the Journal of Philosophical Magazine)

Abstract

Two-step homogenization was applied to a 6xxx alloy containing Zr to enhance the characteristics of Zr-bearing dispersoids and recrystallization resistance. The two-step homogenization treatments were composed of a first step at 400 °C for 48 h and a second step at 500 °C for 2 and 5 h and compared with single-step homogenization conducted at 500 °C for 2 and 5 h. The dispersoid microstructure was characterized using optical microscopy and scanning and transmission electron microscopies. The thermomechanical simulator Gleeble 3800 was used to conduct the hot compression tests at 350°C/1.0s⁻¹. To study the recrystallization resistance, post-deformation annealing at 500 °C for 1 h was performed on the deformed samples. The grain structure after deformation and annealing was characterized based on the EBSD technique. The results showed that compared to single-step homogenization, the dispersoid characteristics were significantly improved using two-step homogenization, where the number density of L1₂-Al₃Zr dispersoids increased by 75 to 145% while their size decreased by 9 to 25% and the distribution of the DO₂₂-(Al, Si)₃(Zr, Ti) dispersoids became more uniform. The improved characteristics of Zr-bearing dispersoids and the narrower dispersoid-free zones produced by the two-step homogenization significantly improved the recrystallization resistance with a reduction in the recrystallized area fraction reached 85% when compared with single-step homogenization.

Keywords

Al-Mg-Si 6xxx alloy; homogenization treatment; Zr-bearing dispersoids; flow stress; recrystallization resistance.

4.1. Introduction

The homogenization treatment is a primary thermal process applied after the direct chill (DC) casting in Al-Mg-Si 6xxx aluminum alloys. The purposes of this treatment are the re-distribution of the alloying elements to overcome the microsegregation, dissolve the low-melting eutectic phases and refine the large intermetallic particles. Therefore, a high-temperature homogenization (500 - 550 °C) is commonly used to achieve such purposes. Subsequently, the homogenized materials undergo a thermo-mechanical process (rolling, extrusion and forging) to achieve the desired shape and mechanical properties. However, the recrystallization in the deformed structure may occur, which negatively affects the mechanical and corrosion resistance properties [1, 2]. Therefore, maintaining the fibrous deformed structure is desirable during the thermo-mechanical process and its subsequent heat treatment (solutionizing or annealing) [3].

Introducing thermally stable dispersoids during homogenization is an effective way to retard the dislocation motion and sub-grain boundary migration and therefore to inhibit the recrystallization. Zirconium is a common microalloying element among the other transition elements with limited solubility and extremely low diffusivity in the aluminum matrix [4, 5]. During homogenization Zr can form nano-sized Al₃Zr dispersoids, which are thermally stable and coherent with the aluminum matrix, and therefore effectively retard the

recrystallization [6, 7]. However, the homogenization temperature significantly affects the dispersoids characteristics. The high temperature leads to precipitation of large dispersoids with low number density, while denser dispersoids with smaller sizes could be achieved by low-temperature homogenization. Therefore, adjusting the homogenization parameters is crucial for optimizing the dispersoids characteristics in terms of number density and size to achieve an adequate inhibition effect of recrystallization.

According to Zener drag force and its pinning effect [8], the larger volume fraction and smaller dispersoids lead to a higher retarding effect on the recrystallization. In addition, the uniform distribution is also important to apply an even pinning effect in the aluminum matrix [9]. Due to the segregation of Zr to the dendrite centers during solidification, only few dispersoids with relatively large sizes are precipitated in the interdendritic regions. Thus, these regions are highly prone to be recrystallized more readily than dendrite centers. The two-step homogenization is a promising approach that effectively improves the precipitation and the distribution of the Al_3Zr dispersoids [6, 10-14]. The first step is commonly conducted at a low temperature for a relatively long soaking time to encourage the nucleation of dispersoids, while the second step is conducted at a high temperature to complete the homogenization conventionally but for a short soaking time to prevent the excessive growth of the dispersoids. It was reported [6] that finer Al_3Zr dispersoids with higher density were observed in AA7150 alloys when applying the two-step homogenization compared to the single-step homogenization. As consequence, a much better recrystallization resistance was achieved in 7xxx alloys after two-step homogenization due to the denser Al_3Zr dispersoids [5, 6, 11-13]. It was also found in Al-Cu 2xxx alloys [14] that improved recrystallization

resistance and strength were achieved due to the fine and dense Al_3Zr after two-step homogenization.

Although a number of studies applied the multi-step homogenization to improve the characteristics of Zr-bearing dispersoids in certain aluminum alloy systems, such as 2xxx and 7xxx, there is a lack of research works in Al-Mg-Si 6xxx series. In addition, static recrystallization may occur during post-deformation heat treatment by migration of grain boundaries and nucleation and growth of new grains [15]. Therefore, this study aimed at studying the effect of two-step homogenization treatment on the precipitation of Zr-bearing dispersoids and recrystallization resistance in an Al-0.3Mg-0.4Si-0.15Zr alloy in comparison with the single-step treatment. The dispersoids were characterized using optical microscopy and scanning and transmission electron microscopies. Hot compression tests were conducted at $350^\circ\text{C}/1.0\text{s}^{-1}$ on homogenized samples using Gleeble 3800 thermomechanical simulator. In order to evaluate the recrystallization resistance, a high-temperature annealing ($500^\circ\text{C}/1\text{h}$) was carried out on the deformed samples, and the resulting microstructures were investigated using EBSD techniques.

4.2. Experimental procedures

An Al-Mg-Si alloy containing Zr was prepared using pure Al (99.7 wt.%) and pure Mg (99.8 wt.%) as well as Al-50 wt.% Si, Al-25 wt.% Fe, and Al-15 wt.% Zr master alloys. The actual chemical composition of the alloy analysed using optical emission spectroscopy is listed in Table 4.1. The material was melted using an electrical resistance furnace and maintained at $\sim 750^\circ\text{C}$ for 30 min. Then, 0.13 wt.% Ti in the form of Al-5Ti-1B master alloy

was added into the melt as a grain refiner. The melt was poured into a rectangular permanent steel mold with dimensions of 30 mm × 40 mm × 80 mm.

Table 4.1: Chemical composition of the studied 6xxx alloy (wt.%).

Mg	Si	Fe	Zr	Ti	Al
0.40	0.35	0.18	0.15	0.13	Bal.

The cast ingots were then subjected to single-step and two-step homogenization treatments, as shown by the schematic diagrams in Fig. 4.1. The single-step treatments were performed at 500 °C for 2 h and 5 h. The two-step treatments included a first step at 400 °C for 48 h and a second step at 500 °C for 2 h and 5 h. The samples were subjected to direct water quenching to room temperature after homogenization. In addition, a few samples were water quenched after the first step (400°C/48h).

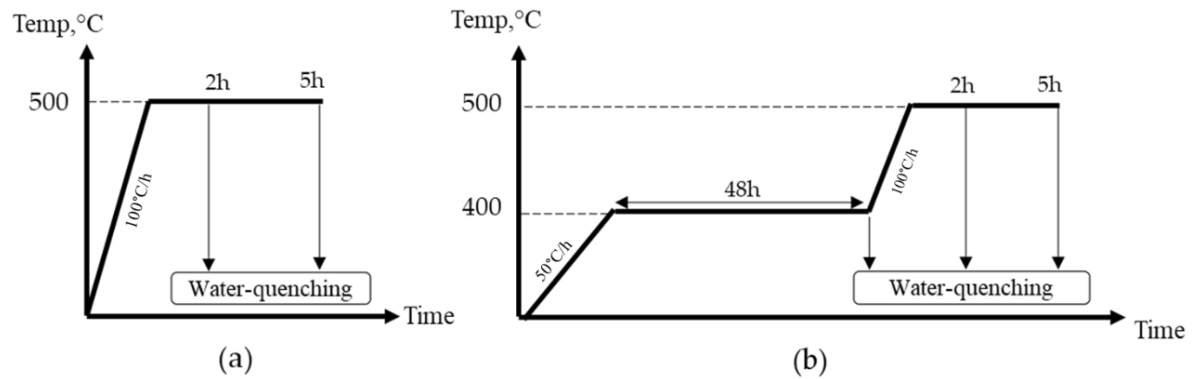


Figure 4.1 Schematic diagrams of the homogenization treatments, (a) single-step and (b) two-step treatments.

Uniaxial hot compression tests were performed on a Gleeble 3800 thermomechanical simulator using cylindrical samples with a diameter of 10 mm and a length of 15 mm. The compression tests involved heating the samples to the deformation temperature of 350 °C at

a heating rate of 2 °C/s and then holding for 3 minutes to ensure a uniform temperature distribution. The samples were deformed with a constant strain rate of 1.0 s⁻¹ to a true strain of 0.7, followed by water quenching to room temperature to retain the deformed microstructure. To study the recrystallization process after the post-deformation heat treatment, the deformed samples were annealed at 500 °C for 1 h, followed by water quenching to room temperature.

To study the microstructure, the homogenized samples were polished using standard metallographic methods. The intermetallic phases and dispersoids were observed using an optical microscope (Nikon, Eclipse ME600) and a scanning electron microscope (SEM, JEOL-6480LV) after etching by 0.5% HF for 30 seconds. In addition, a transmission electron microscope (TEM, JEM-2100) operated at 200 kV was used to observe the fine Zr-bearing dispersoids in detail. The TEM samples were mechanically ground and then electropolished using a twin-jet electropolisher operated at 20 V and -20°C in a 30 vol.% nitric acid and 70 vol.% methanol solution. The samples were observed in the dark and bright field modes along <001> zone axis of the Al matrix to reveal the dispersoids. The average dispersoid size and number density were measured based on image analysis of TEM images and foil thickness. The microstructures after deformation and after post-deformation annealing were characterized using EBSD analysis. The EBSD samples were sectioned parallel to the deformation axis along the centerline and then carefully polished to obtain high indexing quality. For an accurate comparison, the central region of the samples was examined for all conditions. Orientation maps were produced with a step size of 3 µm for grain structure and a fine step size of 0.5 µm to reveal more details on the grain and subgrain structures and to measure the misorientation distribution. The low angle (2-5), medium angle (5-15°), high

angle ($>15^\circ$), and original grain boundaries ($>30^\circ$) were presented by white, green, thin black, and solid black lines, respectively. Misorientation angles below 2° were not considered to avoid the microstructure noise caused by sample preparation. In addition, grain orientation spread (GOS) maps were plotted to reveal any recrystallized grains using MTEX, a comprehensive open-source freely available MATLAB toolbox. A threshold value of 2° was used to distinguish between recrystallized and deformed grains.

4.3. Results and discussion

5.3.1. Dispersoid Microstructure

5.3.1.1. Precipitation of $L1_2$ - Al_3Zr dispersoids

The dark field TEM images in presented Fig. 4.2 show the dispersoid microstructure for different homogenization conditions. The dispersoids appeared in these images were identified to be $L1_2$ - Al_3Zr dispersoids based on their morphology and the crystal structure, as was confirmed by corresponding selected area electron diffraction patterns (SAEDPs) [16]. As an example, the SAEDP corresponding to the image shown in Fig. 4.2a is given in its inset. The characteristics of the Al_3Zr dispersoids in terms of the number density and size varied from one homogenization condition to another. As can be seen in Fig. 4.2a, the first step at 400°C for 48 h resulted in a dense distribution of dispersoids with a very fine size. On the other hand, the single-step homogenization at 500°C , whether after holding for 2 or 5 h (Fig. 4.1b and c), resulted in a lower density of coarser dispersoids. The two-step homogenization treatments, however, improved the dispersoid characteristics as compared with the single-step homogenization at 500°C (Fig. 4.2d and e vs. Fig. 4.2b and c).

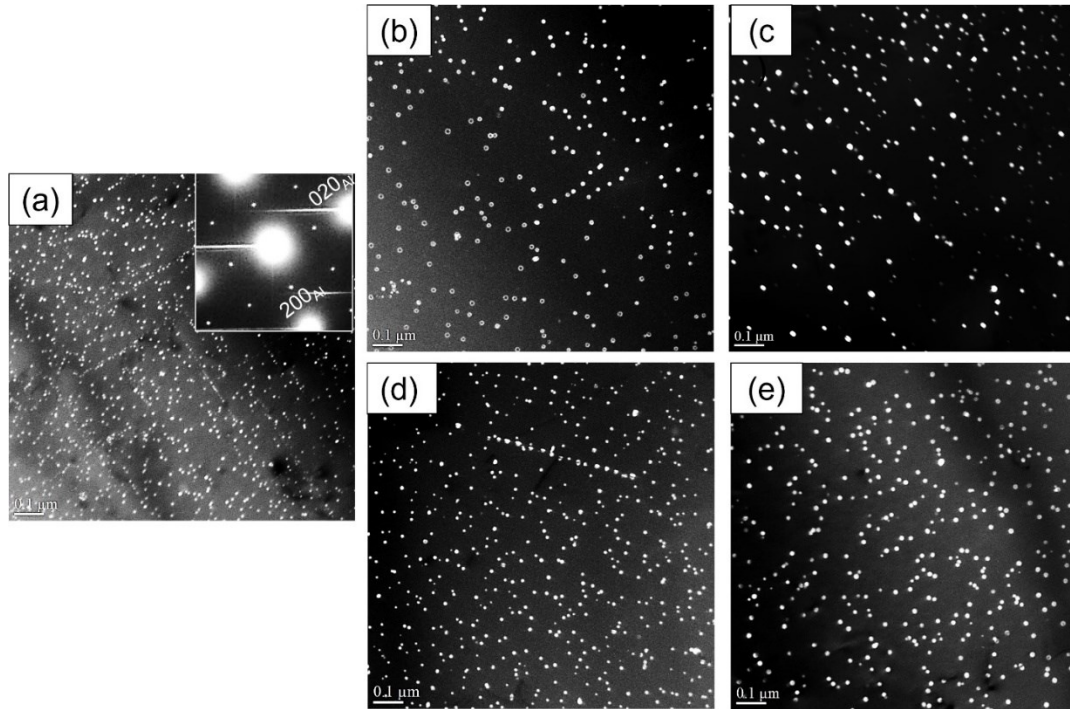


Figure 4.2 TEM dark-field images of Al_3Zr dispersoids formed after different homogenization treatments: (a) $400^\circ\text{C}/48\text{h}$ (first step), (b) $500^\circ\text{C}/2\text{h}$, (c) $500^\circ\text{C}/5\text{h}$, (d) $400^\circ\text{C}/48\text{h} + 500^\circ\text{C}/2\text{h}$ and (e) $400^\circ\text{C}/48\text{h} + 500^\circ\text{C}/5\text{h}$.

The number density and the size of Al_3Zr dispersoids were measured for all homogenization conditions and are listed in Table 4.2 for comparison. A high number density of $2841 \mu\text{m}^{-3}$ with a size of 9 nm was obtained by the first step of $400^\circ\text{C}/48\text{h}$. The number density decreased significantly to $\sim 950 \mu\text{m}^{-3}$ while the size increased to 14 nm for both single-step 500°C treatments. On the other hand, the two-step homogenization of $400^\circ\text{C}/48\text{h} + 500^\circ\text{C}/2\text{h}$ resulted in much better dispersoid characteristics compared to the single-step homogenization of $500^\circ\text{C}/2\text{h}$ by increasing the number density to $2315 \mu\text{m}^{-3}$ and decreasing the size to 9.2 nm. In comparison, increasing the holding time to 5 h in the second step coarsened the dispersoids and decreased their number density. However, the dispersoid

characteristics in this condition were still remarkably better relative to the single-step homogenization of 500°C/5h (Table 4.2).

Table 4.2. Characteristics of Al₃Zr dispersoids after different homogenization treatments.

Homogenization	Number Density, μm^{-3}	Average diameter, nm
400°C/48h (first step)	2841	9.1
500°C/2h	944	13.7
500°C/5h	954	14.1
400°C/48h + 500°C/2h	2316	10.3
400°C/48h + 500°C/5h	1661	12.9

In general, during homogenization, the Al₃Zr dispersoids precipitate out of the α -Al solid solution enriched with Zr solutes during solidification [17]. The variation of the Al₃Zr characteristics is mainly controlled by the homogenization temperature and time. The relatively low homogenization temperature of 400 °C promoted the formation of abundant dispersoid nuclei. Prolonging the holding time at this temperature up to 48 h allowed the growth of these nuclei progressively to dense and fine Al₃Zr dispersoids. The growth of these dispersoids was, however, restricted owing to the low diffusion rate of Zr at 400 °C. On the other hand, the higher homogenization temperature of 500 °C diminished the dispersoid nucleation rate but increased the Zr diffusion rate and consequently the growth rate, leading to a sparse dispersion of coarse Al₃Zr dispersoids. Thus, by conducting the first step of the two-step homogenization at 400 °C for 48 h, the nucleation of fine Al₃Zr dispersoids was enhanced compared to the single-step homogenization at 500 °C, resulting in a higher number density of Al₃Zr dispersoids with a smaller size for both two-step homogenization conditions.

Conducting the second step at 500 °C, whether for 2 or 5 h, coarsened the fine dispersoids formed during the first step. However, it could, on the other hand, satisfy the industrial requirements of 6xxx alloys prior to hot deformation processes by dissolving the eutectic phases and decreasing the microsegregation.

Due to the peritectic reaction during solidification, Zr segregates towards the dendrite centers, resulting in the appearance of dispersoid free zones (DFZs) adjacent to the dendrite/grain boundaries, where the supersaturation level of Zr is lower and consequently the precipitation of Al₃Zr dispersoids is more difficult. Fig. 4.3a and b show the DFZs for the single-step (500°C/2h) and two-step (400°C/48h + 500°C/2h) homogenization conditions, respectively. As can be seen, generally wide DFZs (> 2 μm) were observed in the case of the single-step homogenization (Fig. 4.3a), while the two-step homogenization resulted in much narrower DFZs (< 1 μm, Fig. 4.3b). The first step at 400 °C provides a high driving force for the nucleation of dispersoids [18, 19], especially for the regions adjacent to grain boundaries with a low Zr concentration. Therefore, a higher number density of dispersoids was found close to grain boundaries after the two-step homogenization, resulting in narrower DFZs and an overall improvement in the dispersoid distribution.

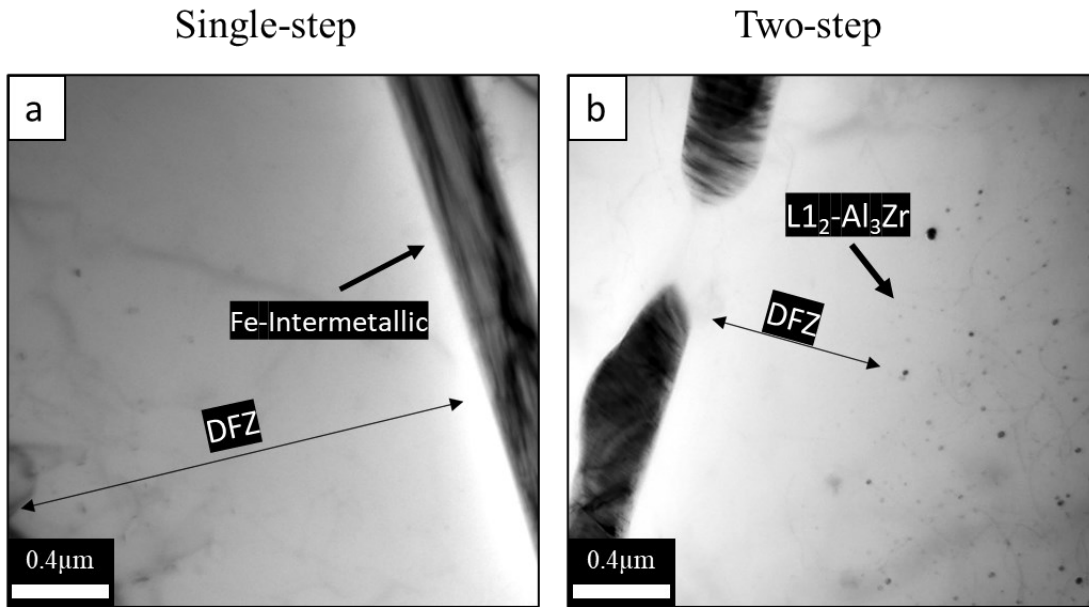


Figure 4.3 Bright field TEM images near grain boundaries showing the width of DFZs in, (a) single- step 500°C/2h, and (b) two-step 400°C/48 h + 500°C/2h homogenization conditions.

5.3.1.2. Precipitation of $DO_{22}-(Al,Si)_3(Zr,Ti)$ dispersoids

In addition to the fine spherical $L1_2-Al_3Zr$ dispersoids, much larger elongated dispersoids (~ 100 nm) were also detected in the single-step and two-step homogenization conditions (Fig. 4.4a), containing Al, Zr and Si as well as a trace of Ti (Fig. 4.4b). Based on the TEM-EDS analysis, these dispersoids were identified as $DO_{22}-(Al,Si)_3(Zr,Ti)$ dispersoids [20], which were reported to form in the presence of Si and Ti [21, 22]

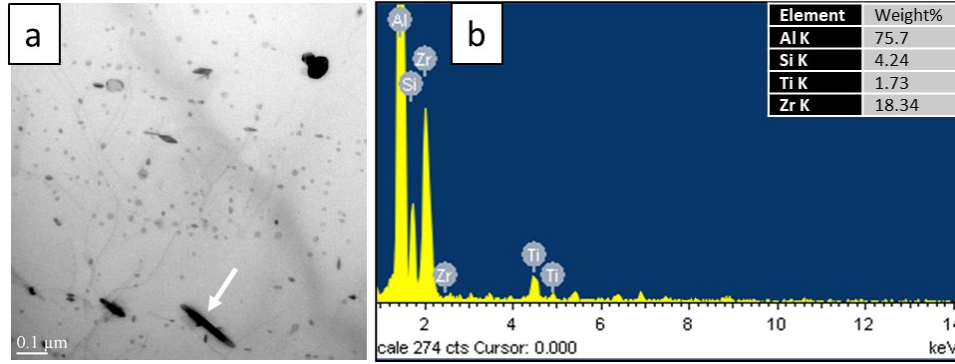


Figure 4.4 (a) Bright field TEM image showing the elongated DO_{22} - $(\text{Al,Si})_3(\text{Zr,Ti})$ dispersoids and (b) the corresponding TEM-EDS spectrum.

The distribution of the DO_{22} - $(\text{Al,Si})_3(\text{Zr,Ti})$ dispersoids could not be properly observed by TEM due to their relatively large size and interspaces. However, contrary to the nanoscale $\text{L}_{12}\text{-Al}_3\text{Zr}$ dispersoids, the distribution of DO_{22} dispersoids could be revealed after etching by optical microscopy in the dark-field mode and SEM (Fig. 4.5). As can be seen, the precipitation of DO_{22} dispersoids occurred near grain boundaries with the single-step $500^\circ\text{C}/5\text{h}$ homogenization (Fig. 4.5a-c), but occurred in the grain cores with a more uniform distribution with the two-step $400^\circ\text{C}/48\text{h} + 500^\circ\text{C}/5\text{h}$ homogenization (Fig. 4.5d-f). This can be attributed to the initial distribution of Si, which promotes the DO_{22} dispersoids [20]. For the single-step 500°C homogenization, a large amount of Si was initially segregated at grain boundaries after casting [23], thereby promoting the precipitation of DO_{22} dispersoids in the grain boundary areas. On the other hand, the first step of $400^\circ\text{C}/48\text{h}$ as part of the two-step treatment enhanced the diffusion of Si inside the grains, resulting in a more uniform distribution of DO_{22} dispersoids in the grain cores.

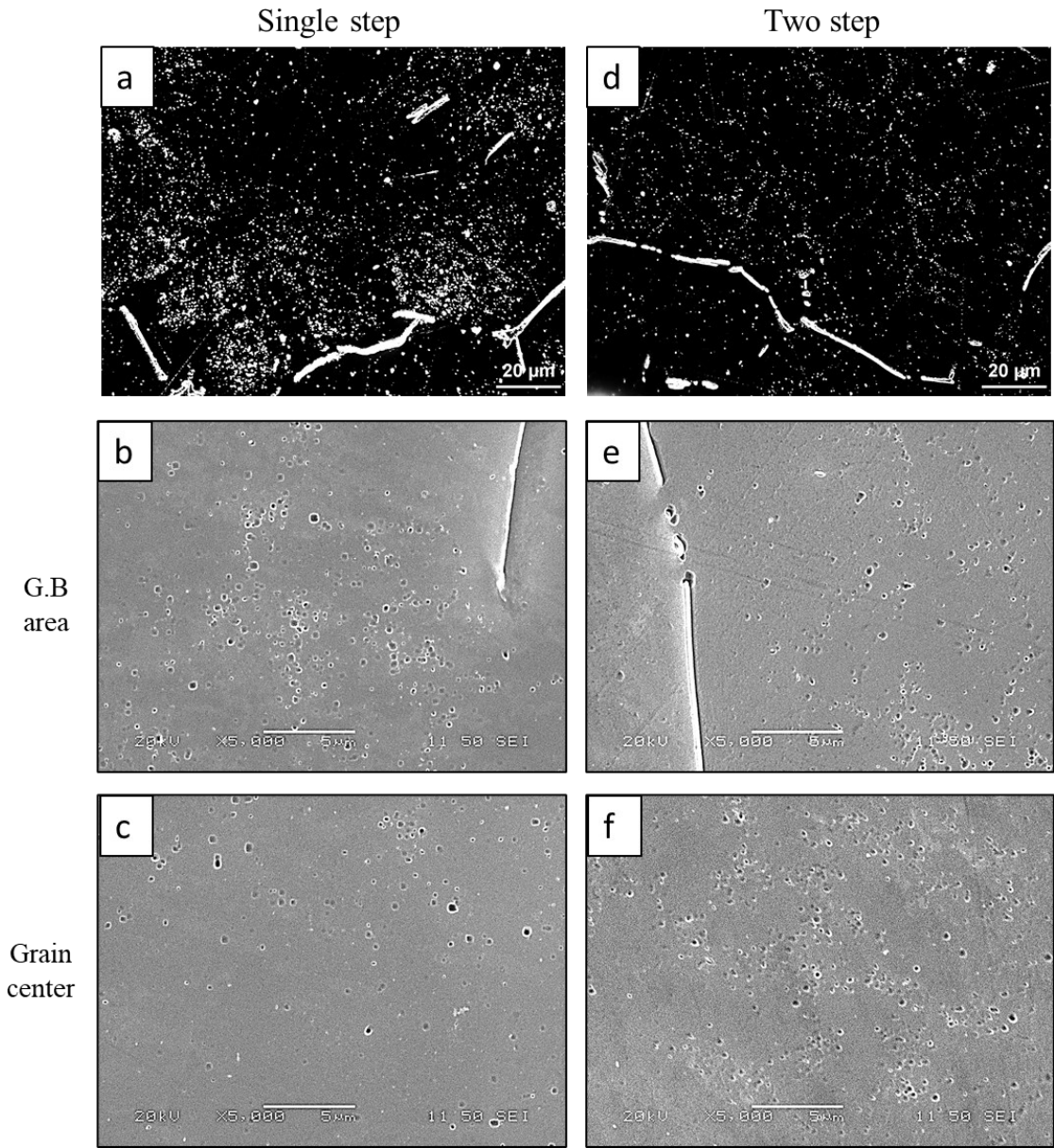


Figure 4.5 Optical dark field and SEM images showing the distribution of the DO₂₂-(Al,Si)₃(Zr,Ti) dispersoids for single-step 500°C/5h (a-c) and two-step 400°C/48h + 500°C/5h (d-f) treatments.

5.3.2. Flow stress

Fig. 4.6 shows the compression flow curves at 350 °C and a strain rate of 1.0 s⁻¹ for different homogenization treatments. For all conditions, the flow stress increased sharply by the intense work hardening at the beginning of compression, and then continued to rise at a lower rate with increasing strain, indicating the domination of the work hardening over the effect of softening mechanisms.

Generally, the flow stress was controlled by both dispersoid and solid solution strengthening effects and the latter was more dominant. The first step of 400°C/48h produced fine, dense L1₂-Al₃Zr dispersoids. However, the relatively low temperature did not allow the dissolution of the equilibrium β-Mg₂Si precipitates, which decreased the supersaturation levels of Mg and Si in the α-Al and consequently the solid solution strengthening, leading to the lowest flow stress in this condition. In comparison, the single-step homogenization at 500 °C for 2 or 5 h moderately increased the flow stress, where the solid solution strengthening was increased by the enhanced dissolution of β-Mg₂Si precipitates at the higher temperature, while a reduced amount of fine L1₂ dispersoids was precipitated in combination with large DO₂₂ dispersoids. Both two-step homogenization treatments, which combined between enhanced dispersoid characteristics and high solid solution strengthening, exhibited the highest flow stresses.

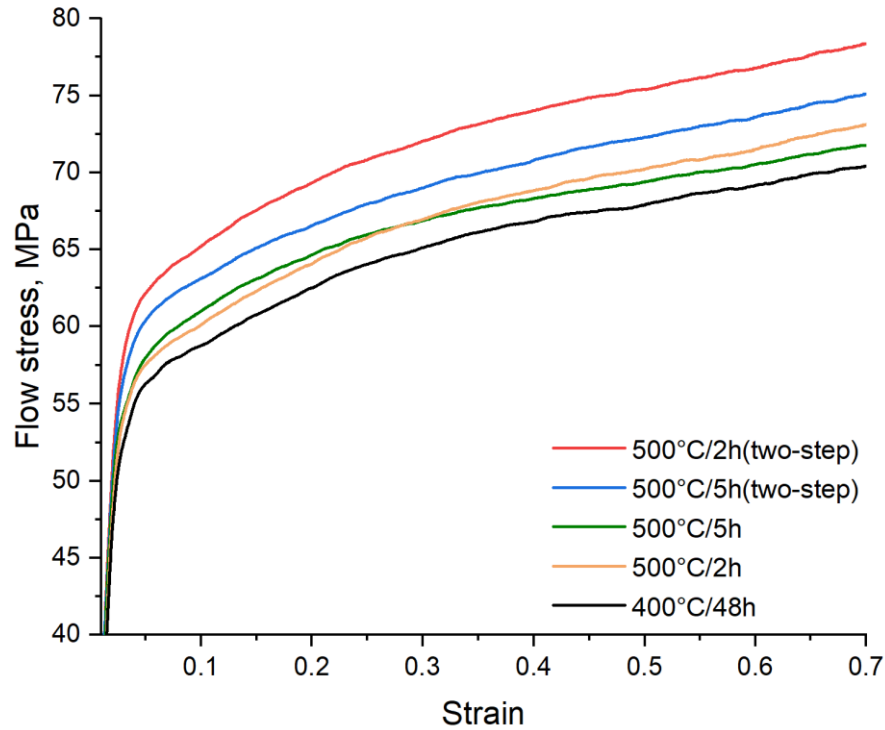


Figure 4.6. Typical flow stress curves after deformation at 350 °C and 1.0 s⁻¹ in different homogenization conditions.

5.3.3. Recrystallization resistance

After the hot compression tests, deformed samples were annealed at 500 °C for 1 h to evaluate the recrystallization resistance. Fig. 4.7 shows the grain spread orientation maps (GOS) for the single-step and two-step homogenization conditions as well as the as-cast condition (no prior homogenization before deformation). In addition, the recrystallized area fractions were measured and plotted in Fig. 4.8. The determination of recrystallized grains was based on the GOS parameter, which can be considered as an indication of the dislocation densities and strain level in the individual grain [24]. The grain structures with a GOS value less than 2° have a lower strain level and are considered recrystallized structures [25, 26]. On the other hand, the deformed structure usually possesses higher GOS values (> 5°). After

annealing, the samples exhibited different degrees of recrystallization depending on the material condition before deformation. For the as-cast material, the microstructure was highly recrystallized (Fig. 4.7a) with an area percentage of 70.4% due to the absence of dispersoids. Moreover, the majority of the remaining deformed structure showed low GOS values (less than 4°). In contrast, much lower degrees of recrystallization were observed in the homogenized samples, depending on the homogenization condition, due to the precipitation of thermally stable dispersoids that could hinder the dislocation motion. A low degree of recrystallization was exhibited by the $400^\circ\text{C}/48\text{h}$ first step treatment (Fig. 4.7b) with a recrystallized area fraction of only 14.1%. In contrast, single-step homogenization at 500°C resulted in higher degrees of recrystallization (Fig. 4.7c and d) with recrystallized area fractions of 28.9 and 26.6% after holding for 2 and 5 h, respectively. On the other hand, the recrystallization process was almost completely inhibited by the two-step homogenization of $400^\circ\text{C}/48\text{h} + 500^\circ\text{C}/2\text{h}$ (Fig.4.7e) with only 4% recrystallized area fraction. In addition, most of the deformed regions showed high GOS values ($> 8^\circ$), indicating a less recovered structure. However, increasing the holding time of the second step to 5 h negatively affected the recrystallization resistance, increasing the recrystallized area fraction to 20.2% but with high GOS values (>10 , Fig. 4.7f). The recrystallization resistance in this case was still, however, better than that obtained after single-step homogenization at 500°C whether for 2 or 5 h (20.2% vs. 28.9% and 26.6% recrystallized area fraction).

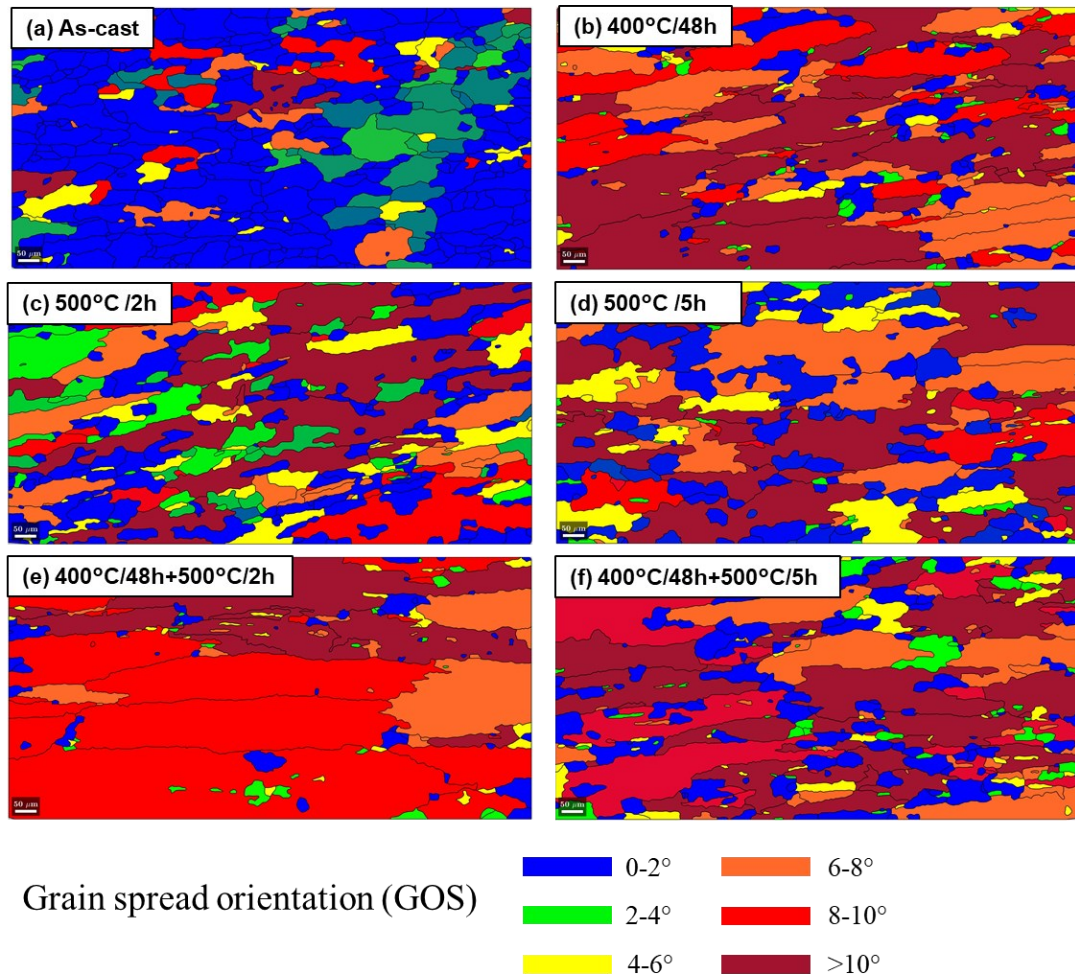


Figure 4.7. Grain spread orientation maps for different alloy conditions after deformation at 350 °C and 1.0 s^{-1} and annealing at 500 °C for 1 h.

The samples homogenized by the single-step 500°C/2h and two-step 400°C/48h + 500°C/2h treatments were selected for further microstructural analysis. All-Euler maps shown in Fig. 4.9 reveal the evolution of different grains and their boundaries for both samples before and after annealing. In addition, the distribution and the quantitative analysis of the misorientation angles are presented in Fig. 4.10. The as-deformed structure in both homogenization cases (Fig. 4.9a and b) showed typically elongated fibrous grains with high densities of low and medium angle boundaries, indicating a dynamically recovered structure.

However, as shown in Fig. 4.10a and b, a much higher fraction of low-angle boundaries (LAB) with a lower mean misorientation angle was associated with the two-step homogenization compared with the single-step homogenization (84.6 % vs. 65.8 % and 9.6° vs. 15.4°, respectively). Such results indicate that dynamic recovery during hot deformation was slower after two-step homogenization. Moreover, some small equiaxed grains were observed along grain boundaries in the case of the single-step homogenization (arrowed in Fig. 4.9a).

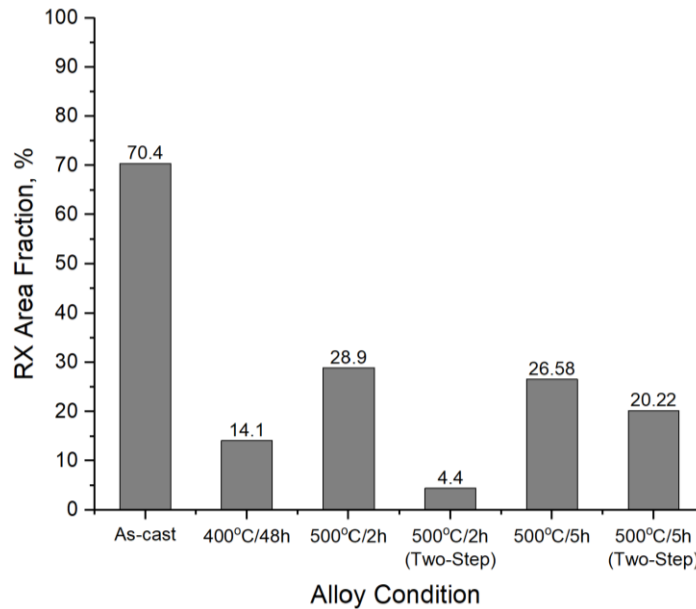


Figure 4.8 Recrystallization area fraction for different alloy conditions after deformation at 350 °C and 1.0 s⁻¹ and annealing at 500 °C for 1 h.

After annealing, a significant difference in the microstructure was observed between the single-step and two-step treatments. Single-step homogenization (Fig. 4.9c) resulted in some large recrystallized grains along grain boundaries, indicating severe growth of the pre-existing grains observed after deformation. In contrast, the two-step homogenization only exhibited a dynamically recovered structure with some development of low angle boundaries

(white lines) into medium-angle boundaries (green lines). The high annealing temperature (500 °C) facilitates dislocation motion and annihilation and, subsequently, dynamic recovery. These results are confirmed by the distribution of the misorientation angles (Fig. 4.10c and d), showing a higher fraction of LAB after two-step homogenization compared with the single-step homogenization (74.6 % vs. 60.1 %).

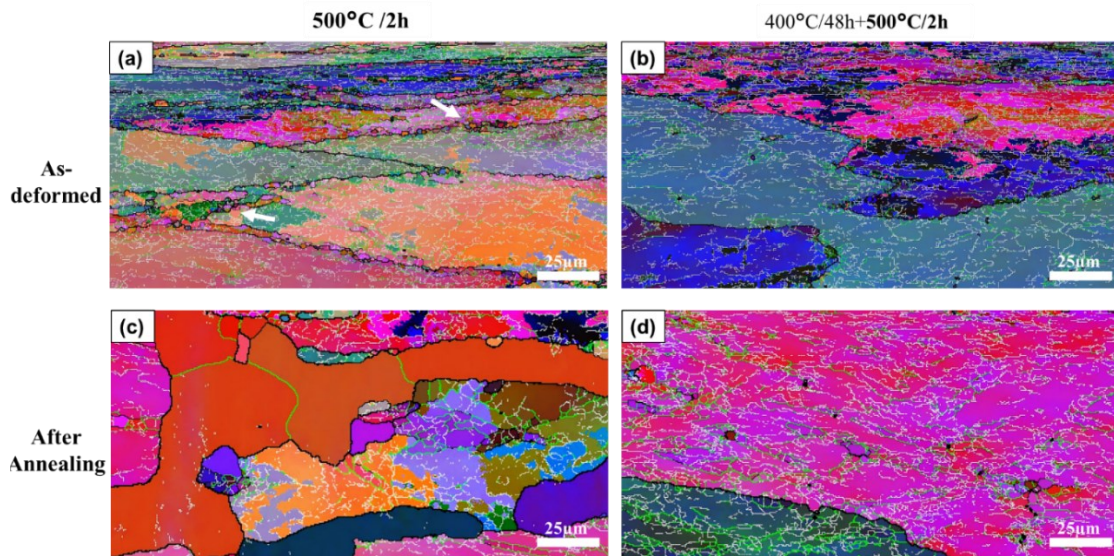


Figure 4.9 All-Euler orientation maps of as-deformed (a, b) and annealed (c, d) grain structures for the single-step homogenization of 500°C/2h (a, c) and the two-step homogenization of 400°C/48h + 500°C/2h (b, d). Low angle (2°-5°), medium angle (6°-15°), and high angle boundaries (>15°) are represented by white, green, and black lines, respectively.

It has been demonstrated that the coherent Al₃Zr dispersoids can substantially retard dislocation movement and subgrain boundary migration during thermal treatments [27]. The volume fraction and size of dispersoids determine the amount of the Zener pinning pressure on the grain boundaries [8]. The pinning pressure can be increased by maximizing the

volume fraction of dispersoids and minimizing their size. The two-step homogenization could achieve such a combination due to the higher number density of fine Al_3Zr dispersoids. Consequently, a less recovered structure, which was represented by a higher fraction of low angle boundaries, was obtained after deformation with the two-step homogenization compared with the single-step homogenization. Moreover, static recovery was also limited during annealing, in the case of the two-step homogenization.

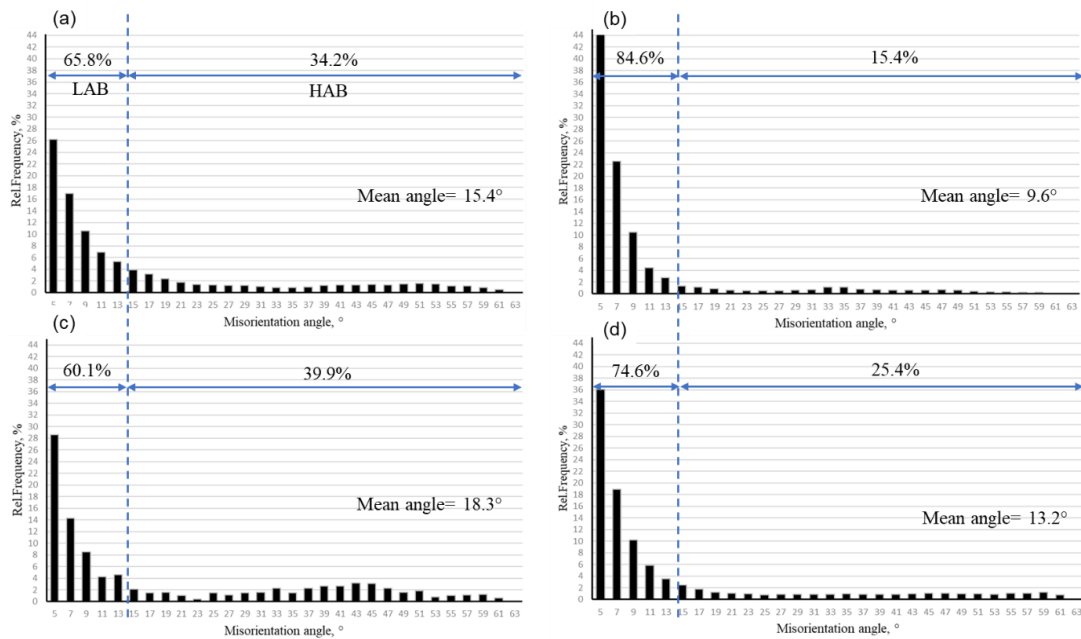


Figure 4.10 The misorientation angle distribution of as-deformed (a, b) and annealed (c, d) grain structures for the single-step homogenization of $500^{\circ}C/2h$ (a, c) and the two-step homogenization of $400^{\circ}C/48 h + 500^{\circ}C/2h$ (b, d).

The distribution of dispersoids also plays a crucial role in recrystallization resistance. The nonuniform distribution of dispersoids leads to the formation of dispersoid-free zones adjacent to grain boundaries (Fig. 4.3). In addition, the large intermetallic particles formed along the grain boundaries after solidification could promote the recrystallization via particle

stimulated nucleation mechanism [28]. Such microstructural features lead to more rapid recrystallization in these regions compared to the grain interiors. The single-step homogenization exhibited wide DFZs depleted of $L1_2$ - Al_3Zr dispersoids, as shown in Fig. 4.3a. In addition, a nonuniform distribution of DO_{22} - $(Al,Si)_3(Zr,Ti)$ dispersoids was observed (Fig. 4.5a to c), though this dispersoid-type was reported to have less effect on recrystallization compared to the $L1_2$ type [29]. As a result, some small, recrystallized grains were observed after deformation along the grain boundaries (Fig. 4.9a). Later, these small grains were able to grow and coarsen during annealing due to the insufficient pinning force in the DFZs. In contrast, the two-step homogenization provided a more uniform distribution of both $L1_2$ - Al_3Zr and DO_{22} - $(Al,Si)_3(Zr,Ti)$ dispersoids, resulting in narrower DFZs. As a result, a significant improvement in the recrystallization resistance was observed after hot deformation or after annealing.

4.4. Conclusions

A two-step homogenization practice was applied to improve the dispersoid distribution and recrystallization resistance of a Zr-containing 6xxx alloy. From the results obtained, the following conclusions could be drawn:

- (1) The characteristics of Zr-bearing dispersoids were significantly improved by the two-step homogenization. The number density of $L1_2$ - Al_3Zr dispersoids increased by 75 to 145%, while their size decreased by 9 to 25% compared with the single-step homogenization.
- (2) Large DO_{22} - $(Al,Si)_3(Zr,Ti)$ dispersoids were precipitated near the grain boundaries after the single-step homogenization. However, the distribution of such dispersoids was more uniform in the aluminium matrix after the two-step homogenization.
- (3) Two-step homogenization resulted in a higher flow stress relative to single-step treatments due to the enhanced characteristics of Al_3Zr dispersoids and the more uniform distribution of $(Al,Si)_3(Zr,Ti)$ dispersoids.
- (4) The improved distribution of Zr-bearing dispersoids and the narrower dispersoid-free zones produced by two-step homogenization significantly improved the recrystallization resistance during post-deformation annealing, resulting in a reduction in the recrystallized area fraction reached 85% when compared with the single-step homogenization.

References

1. Peng, G.S., et al., *The effect of recrystallization on corrosion and electrochemical behavior of 7150 Al alloy*. Materials and Corrosion, 2011. **62**(1): p. 35-40.
2. Birol, Y., *Effect of Cr and Zr on the grain structure of extruded EN AW 6082 alloy*. Metals and Materials International, 2016. **20**(4): p. 727-732.
3. Poletti, C., T. Wójcik, and C. Sommitsch, *Hot Deformation of AA6082 Containing Fine Intermetallic Particles*. Metallurgical and Materials Transactions A: Physical Metallurgy and Materials Science, 2012. **44**(3): p. 1577-1586.
4. Knipling, K.E., D.C. Dunand, and D.N. Seidman, *Precipitation evolution in Al–Zr and Al–Zr–Ti alloys during aging at 450–600°C*. Acta Materialia, 2008. **56**(6): p. 1182-1195.
5. Jia, Z., et al., *Enhancement of recrystallization resistance of Al–Zr–Mn by two-step precipitation annealing*. Materials Science and Engineering A, 2008. **483-484**: p. 195-198.
6. Guo, Z., G. Zhao, and X.G. Chen, *Effects of two-step homogenization on precipitation behavior of Al₃Zr dispersoids and recrystallization resistance in 7150 aluminum alloy*. Materials Characterization, 2015. **102**: p. 122-130.
7. Li, H., et al., *Effects of Er and Zr additions on precipitation and recrystallization of pure aluminum*. Scripta Materialia, 2013. **68**(1): p. 59-62.
8. Nes, E., N. Ryum, and O. Hunderi, *On the Zener drag*. Acta Metallurgica, 1985. **33**(1): p. 11-22.
9. Xie, Z., et al., *Microstructure Evolution and Recrystallization Resistance of a 7055 Alloy Fabricated by Spray Forming Technology and by Conventional Ingot Metallurgy*. Metallurgical and Materials Transactions A: Physical Metallurgy and Materials Science, 2020. **51**(10): p. 5378-5388.

10. Deng, Y., et al., *Effect of double-step homogenization treatments on the microstructure and mechanical properties of Al–Cu–Li–Zr alloy*. *Materials Science and Engineering: A*, 2020. **795**.
11. Guo, Z., G. Zhao, and Chen, X.G, *Effects of homogenization treatment on recrystallization behavior of 7150 aluminum sheet during post-rolling annealing*. *Materials Characterization*, 2016. **114**: p. 79-87.
12. LÜ, X.-y., et al., *Effect of one-step and two-step homogenization treatments on distribution of Al₃Zr dispersoids in commercial AA7150 aluminium alloy*. *Transactions of Nonferrous Metals Society of China*, 2012. **22**(11): p. 2645-2651.
13. Robson, J.D., *Optimizing the homogenization of zirconium containing commercial aluminium alloys using a novel process model*. *Materials Science and Engineering: A*, 2002. **338**(1-2): p. 219-229.
14. Liu, Q., et al., *Precipitation of Al₃Zr by two-step homogenization and its effect on the recrystallization and mechanical property in 2195 Al–Cu–Li alloys*. *Materials Science and Engineering: A*, 2021. **821**: p. 141637.
15. McQueen, H.J., et al., *Hot Deformation and Processing of Aluminum Alloys*. 2016: CRC Press. 1-564.
16. Li, Y., et al., *Two-stage homogenization of Al–Zn–Mg–Cu–Zr alloy processed by twin-roll casting to improve L12 Al₃Zr precipitation, recrystallization resistance, and performance*. *Journal of Alloys and Compounds*, 2021. **882**: p. 160789.
17. Knipling, K.E., D.C. Dunand, and D.N. Seidman, *Precipitation evolution in Al–Zr and Al–Zr–Ti alloys during isothermal aging at 375–425 C*. *Acta Materialia*, 2008. **56**(1): p. 114-127.
18. Mochugovskiy, A.G., et al., *The mechanism of L12 phase precipitation, microstructure and tensile properties of Al–Mg–Er–Zr alloy*. *Materials Science and Engineering: A*, 2019. **744**: p. 195-205.

19. Souza, P.H.L., C.A.S.d. Oliveira, and J.M.d.V. Quaresma, *Precipitation hardening in dilute Al–Zr alloys*. Journal of Materials Research and Technology, 2018. **7**(1): p. 66-72.
20. Litynska, L., et al., *TEM and HREM study of Al₃Zr precipitates in an Al–Mg–Si–Zr alloy*. J Microsc, 2006. **223**(Pt 3): p. 182-4.
21. Tsunekawa, S. and M.E. Fine, *Lattice parameters of Al₃ (Zr_xTi_{1-x}) vs. x in Al-2 at.% (Ti + Zr) alloys*. Scripta Metallurgica, 1982. **16**: p. 391-392.
22. Jia, Z.-H., et al., *Precipitation behaviour of Al₃Zr precipitate in Al–Cu–Zr and Al–Cu–Zr–Ti–V alloys*. Transactions of Nonferrous Metals Society of China, 2012. **22**(8): p. 1860-1865.
23. Seo, H., et al., *Solidification and segregation behaviors in 6061 aluminum alloy*. Metals and Materials International, 2013. **19**: p. 433-438.
24. Wang, W. and A. Alfantazi, *Correlation between grain orientation and surface dissolution of niobium*. Applied Surface Science, 2015. **335**: p. 223-226.
25. Li, J., et al., *Hot deformation and dynamic recrystallization in Al–Mg–Si alloy*. Materials Characterization, 2021. **173**: p. 110976.
26. Luo, R., et al., *Hot workability and dynamic recrystallization behavior of a spray formed 7055 aluminum alloy*. Materials Characterization, 2021. **178**: p. 111203.
27. Shi, C. and Chen, X.G, *Effect of Zr addition on hot deformation behavior and microstructural evolution of AA7150 aluminum alloy*, in *Materials Science and Engineering: A*. 2014. p. 183-193.
28. Zang, Q., et al., *Effects of initial microstructure on hot deformation behavior of Al-7.9Zn-2.7Mg-2.0Cu (wt%) alloy*. Materials Characterization, 2019. **151**: p. 404-413.
29. Elasheri, A., et al., *Evolution of Zr-Bearing Dispersoids during Homogenization and Their Effects on Hot Deformation and Recrystallization Resistance in Al-0.8%Mg-*

1.0%Si Alloy. Journal of Materials Engineering and Performance, 2021. **30**(10): p. 7851-7862.

CHAPTER 5: Nucleation and Transformation of Zr-bearing dispersoids in Al-Mg-Si 6xxx alloys

Abstract

The nucleation and transformation of L_{12} - Al_3Zr and DO_{22} - $(Al,Si)_3Zr$ dispersoids in Al-Mg-Si 6xxx alloys during heat treatment were studied using the interrupted quench technique and transmission electron microscopy observation. The results showed that spherical L_{12} - Al_3Zr dispersoids precipitated preferentially along $\langle 001 \rangle_{Al}$ at the early stages of nucleation, coinciding with the same sites and orientation of β' precipitates that dissolved during heating, suggesting that the Si-enriched sites after the β' dissolution provided favorable nucleation sites for L_{12} dispersoids. At the relatively low heat treatment temperature (400 °C), the L_{12} - Al_3Zr dispersoids predominated in the aluminum matrix and no transformation occurred. With increasing the temperature towards 550 °C, the L_{12} - Al_3Zr dispersoids started to transform to the DO_{22} - $(Al,Si)_3Zr$. At the high temperature, the elongated DO_{22} - $(Al,Si)_3Zr$ dispersoids became the dominated phase and were formed through the transformation of the pre-existing L_{12} dispersoids rather than a direct precipitation from the supersaturated aluminum solid solution.

Keywords: Al-Mg-Si 6xxx alloys, Zr-bearing dispersoids, nucleation, transformation

5.1. Introduction

Zirconium microalloying in aluminum alloys is widely used to control the grain structure, improve the recrystallization resistance, and enhance the mechanical properties and corrosion resistance [1]. Such effects could be achieved via the precipitation of nano-sized Zr-bearing dispersoids. Due to the low solubility of Zr in α -Al, a high supersaturation could be obtained upon solidification, providing a high driving force for the precipitation of Zr-bearing dispersoids during subsequent heat treatment. Zr offers a very low diffusivity in the aluminum matrix, which improves high thermal stability and coarsening resistance of the formed dispersoids [2, 3]. However, the precipitation behavior of such dispersoids could be affected by the other alloying elements and the heat treatment parameters.

The decomposition of the supersaturated solid solution initially occurs by forming nano-scaled $L1_2$ - Al_3Zr dispersoids during heat treatment [4]. However, the nucleation of Zr-bearing dispersoids is greatly affected by the localized level of supersaturation. For instance, high precipitation rates could be found in the dendrite centers due to the large Zr concentration in those areas as a result of the peritectic reaction during solidification, leading to a high driving force for precipitation [5]. In contrast, a much lower concentration of Zr is found in the interdendritic regions resulting in weaker precipitation, which occurs by heterogeneous nucleation on dislocation [6]. On the other side, the existence of other alloying elements is essential to promote the nucleation of Zr-bearing dispersoids. For instance, Cu and Zn were reported to accelerate the precipitation of Al_3Zr via $CuAl_2$ and Zn_2Mg precipitates, respectively, which could act as nucleation sites [7, 8]. In addition, Si was reported to significantly promote the precipitation of Zr-bearing dispersoids through the Si-vacancy clusters that act as heterogeneous sites for such dispersoids [9]. Also, Si was

reported to improve the diffusion kinetics of Zr in the aluminum matrix, thus reducing the peak-aging time of Zr-bearing dispersoids [10].

Zr-bearing dispersoids can exist in different crystal structures depending on the heat treatment condition. At relatively low temperatures (300 to 450 °C), the high-symmetry cubic L_{12} - Al_3Zr dispersoids commonly precipitate with spherical morphology and small size. Such type of dispersoids exhibits a coherent interface with the matrix due to their good mismatch with the aluminum matrix [11]. This thermodynamically metastable L_{12} - Al_3Zr can eventually transform into the tetragonal structure phases (DO_{22} or DO_{23}) at high temperatures (above 500 °C) [2, 12]. Although the incoherent DO_{23} is the most stable phase that typically exists at high temperatures with elongated morphology, the semi-coherent DO_{22} is reported to precipitate instead of DO_{23} when the alloy contains a considerable amount of Si [13]. It is reported that Si stabilizes DO_{22} by promoting the phase transformation of L_{12} . This transformation occurs by substituting Al with a small amount of Si and changing the structure of L_{12} to DO_{22} instead of the stable DO_{23} . The stability of L_{12} is negatively affected by the addition of Si through decreasing the stacking fault energy of L_{12} , which subsequently lowers the barrier for the transformation to DO_{22} [14].

In our previous work [15] in 6xxx alloys, it is reported that the different Zr-bearing dispersoids could have different recrystallization resistances. However, the precipitation behavior of Zr-bearing dispersoids in Al-Mg-Si 6xxx alloys, including the nucleation and transformation, has not been well understood yet. Using a Zr-containing 6xxx model alloy, the aim of this work is to investigate the nucleation and transformation of Zr-bearing dispersoids during heat treatment. Samples were water-quenched at different temperatures

and at different soaking times. The nucleation of $L1_2$ dispersoids and the transformation of $L1_2$ to DO_{22} is examined using TEM observation.

5.2. Experimental Procedures

An Al-Mg-Si model alloy (Al-0.89Mg-0.99Si-0.18Fe-0.14Ti, in wt.%) containing 0.15 wt.% Zr was used in this study. The alloy was prepared using pure Al (99.7 wt.%) Mg (99.8 wt.%) as well as Al-50 wt.% Si, Al-25 wt.% Fe, Al-5 wt.% Ti-1 wt.% B and Al-15 wt.% Zr master alloys. The materials were melted using an electrical resistance furnace and cast into a permanent steel mould preheated to 250°C to obtain rectangular cast ingots with dimensions of 30 mm × 40 mm × 80 mm. Different heat treatment procedures were applied to cast ingots, followed by water-quenched at different temperatures and holding times (Fig. 5.1). Regarding the nucleation of $L1_2$ - Al_3Zr dispersoids, a series of samples were heated from ambient temperature to 400 °C at a relatively low heating rate of 50°C/h and isothermally held for different times. Such holding temperature was chosen to allow the sole precipitation of $L1_2$ - Al_3Zr without DO_{22} - $(Al,Si)_3Zr$ precipitation. As a second step (after 400 °C for 48 h), these samples were further heated up to 550 °C at a higher heating rate of 150°C/h to study the stability of pre-existence dispersoids and transformation mechanism. The higher heating rate was used to avoid the further precipitation of $L1_2$ - Al_3Zr dispersoids during heating. In addition, a part of the samples was directly heated from room temperature to 500 °C and 550 °C at a similar heating rate of 150°C/h for comparison.

A transmission electron microscope (TEM, JEM-2100) equipped with energy-dispersive X-ray spectroscopy (EDS) operated at 200 kV was used to observe the Zr-bearing dispersoids. The quenched samples for TEM observation were first mechanically ground to approximately 40–60 µm, and then electropolished using a twin-jet electropolisher operated

at 15 V and -20 °C with 30 vol.% nitric acid and 70 vol.% methanol. The dark-field mode of TEM was primarily used for the observation of $L1_2$ - Al_3Zr dispersoids using $L1_2$ superlattice reflection of precipitates along the $\langle 001 \rangle$ zone axis. For DO_{22} - $(Al, Si)_3Zr$ dispersoid observation, the bright-field mode of TEM near $\langle 001 \rangle$ zone axis of aluminum matrix was used.

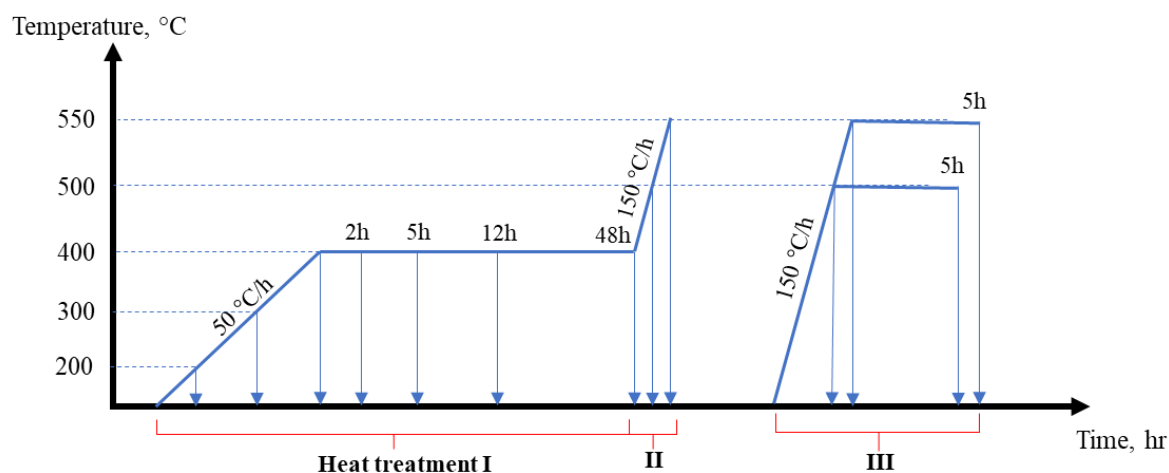


Figure 5.1 Different heat treatment procedures performed on the studied alloy.

5.3. Results and discussion

5.3.1. The nucleation of $L1_2$ dispersoids

Figure 5.2 shows bright-field TEM images of the H-Si alloy samples quenched at 200, 300 and 400 °C during the heating ramp from ambient temperature to 400 °C. The H-Si alloy contains 0.99 wt.% Si and Mg/Si ratio of ~ 1 . When the samples were heated to 200 °C, a great number of fine needle-shaped MgSi precipitates appeared along $\langle 001 \rangle_{\alpha-Al}$ with a dimension of ~ 5 nm in diameter and ~ 35 nm in length (Fig. 5.2a). The small black dots (arrowed) are the cross-sections of these precipitates. Based on the morphology and size,

such fine precipitates were identified to be the coherent β'' -Mg₅Si₆ precipitates [16]. Increasing the temperature to 300 °C resulted in coarsening and transformation of the precipitates, which reached ~10 nm in diameter and ~400 nm in length (Fig. 5.2b), suggesting the transformation to β' -Mg_{1.8}Si precipitates [17, 18]. When the samples reached 400 °C, a significant reduction of the number density of β' precipitates and a few equilibrium β -Mg₂Si particles were observed (Fig. 5.2c), implying the dissolution and transformation of the metastable β' precipitates. It is evident that the supersaturated solid solution enriched with Mg and Si after solidification was decomposed during heating to form such metastable MgSi precipitates [18]. On the other hand, there were no visible Zr-bearing dispersoids formed at this stage.

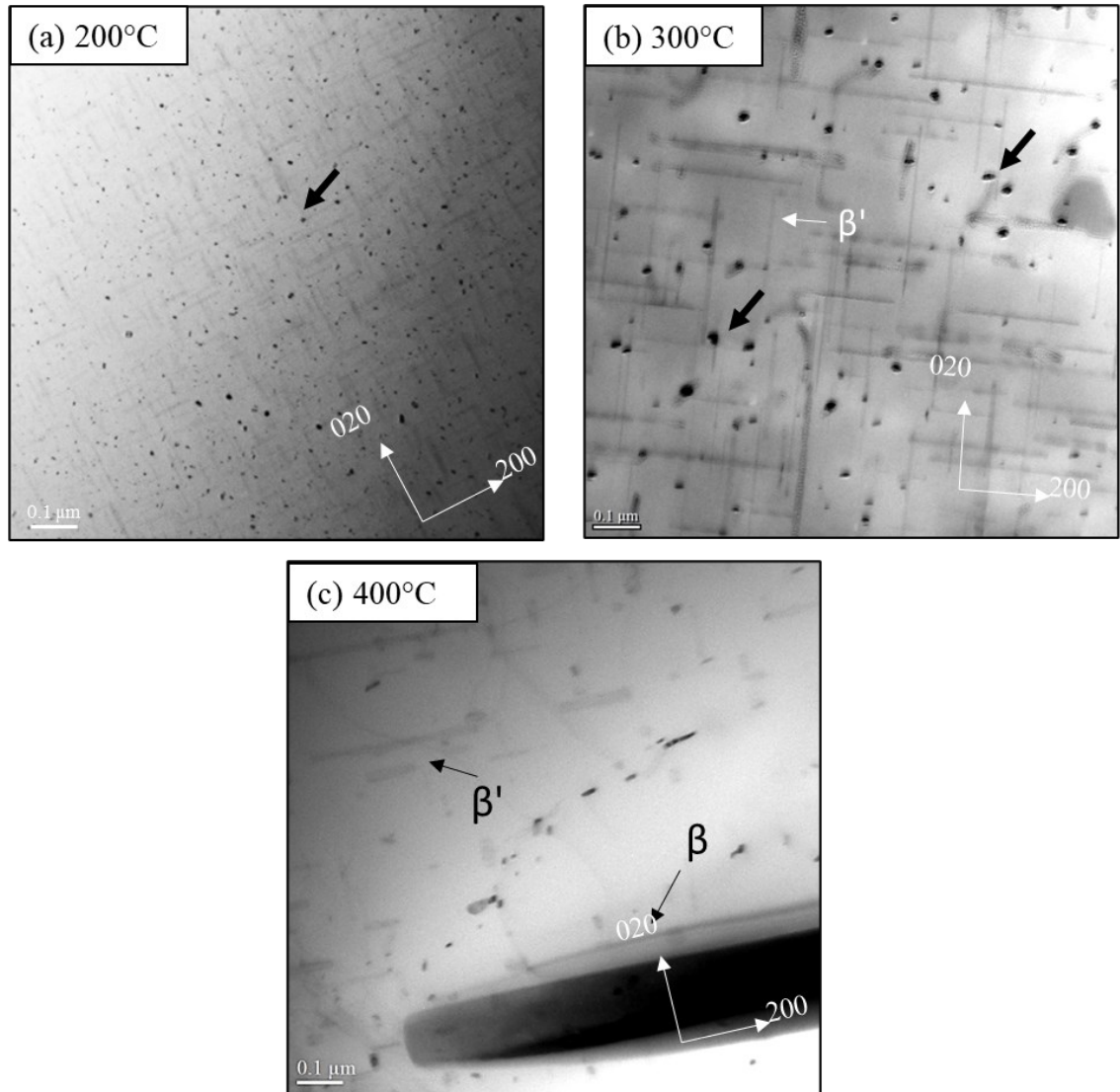


Figure 5.2 Bright-field TEM images showing the precipitation during heating to 400 °C for the samples quenched from (a) 200 °C, (a) 300 °C, (a) 400 °C.

With the isothermal holding of the samples at 400 °C, fine dispersoids with spherical morphology were precipitated. Fig. 5.3 shows dark field TEM images of these dispersoids after holding at 400°C for different times. After 2 h, a few very small dispersoids (few nm) were observed as shown in Fig. 5.3a. Based on their spherical morphology and a corresponding selected area diffraction pattern (SADP, insert of Fig. 5.3a), these dispersoids

were identified as $L1_2$ - Al_3Zr dispersoids [19]. Further isothermal holding at 400 °C for 5 h resulted in a remarkable increase in the number density of $L1_2$ - Al_3Zr dispersoids (Fig. 5.3b). Interestingly, these dispersoids were found to exhibit a preferred orientation along $\langle 001 \rangle_{Al}$, which was the same orientation as the previous β' - $Mg_{1.8}Si$ precipitates (Fig. 5.2b). With further holding towards 12 h, much more Al_3Zr dispersoids precipitated and grew, as shown in Fig. 5.3c. The preferred precipitation direction of the dispersoids along $\langle 001 \rangle_{Al}$ was still visible, which indicates that the majority of Al_3Zr dispersoids nucleated and grew on the previous β' - $Mg_{1.8}Si$ sites. As the isothermal holding was prolonged to 48 h, the preferred orientation became less clear due to the precipitation of a large number of dispersoids (Fig. 5.3d).

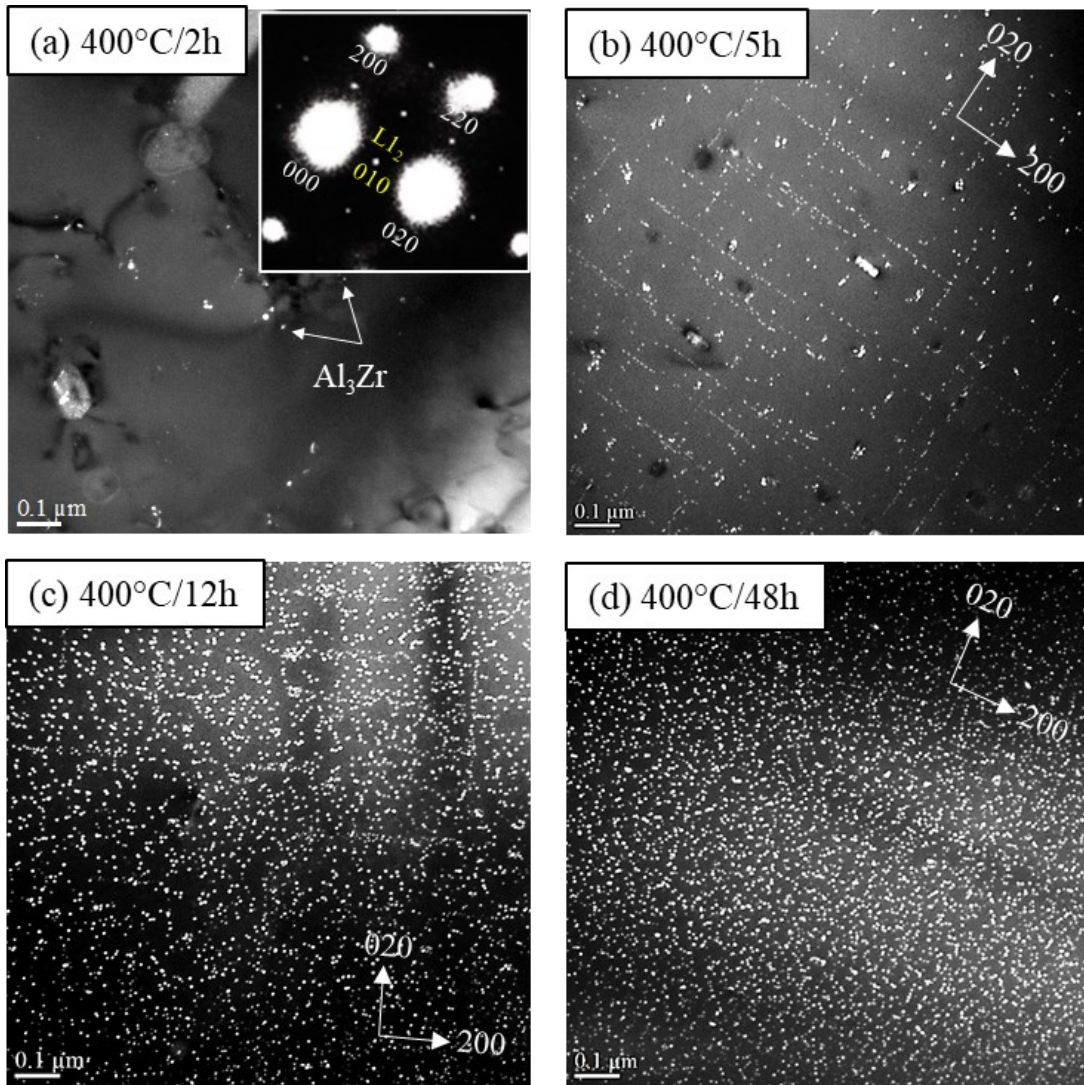


Figure 5.3 Dark-field TEM images of samples isothermally held for (a) 2 h, (b) 5 h, (c) 12 h and (d) 48 h at 400 °C.

Figure 5.4 shows a bright-field TEM image of the L-Si alloy quenched at 300 °C and dark-field TEM images after isothermal holding at 400 °C for 5 and 48 h. The L-Si alloy contains 0.39 wt.% Si and Mg/Si ratio of ~ 1 . Compared with the H-Si alloy (Figs. 5.2 and 5.3), the L-Si alloy showed much less precipitation of both MgSi precipitates and Al_3Zr dispersoids. Certainly, the low Mg and Si levels in the L-Si alloy resulted in a less supersaturated solid solution, thereby decreasing the amount of the β' - $\text{Mg}_{1.8}\text{Si}$ precipitates as

shown in Fig. 5.4a. Similar to the H-Si alloy, spherical $L1_2$ - Al_3Zr dispersoids were preferentially precipitated along $\langle 001 \rangle_{Al}$ after holding for 5 and 48 h at 400 °C, which was the same orientation of the previous β' precipitates. The lower number density of $L1_2$ - Al_3Zr dispersoids in the L-Si alloy relative to the H-Si alloy (Fig. 5.4b and c vs. Fig. 5.3b and d) seems to be proportional to the number density of the β' precipitates.

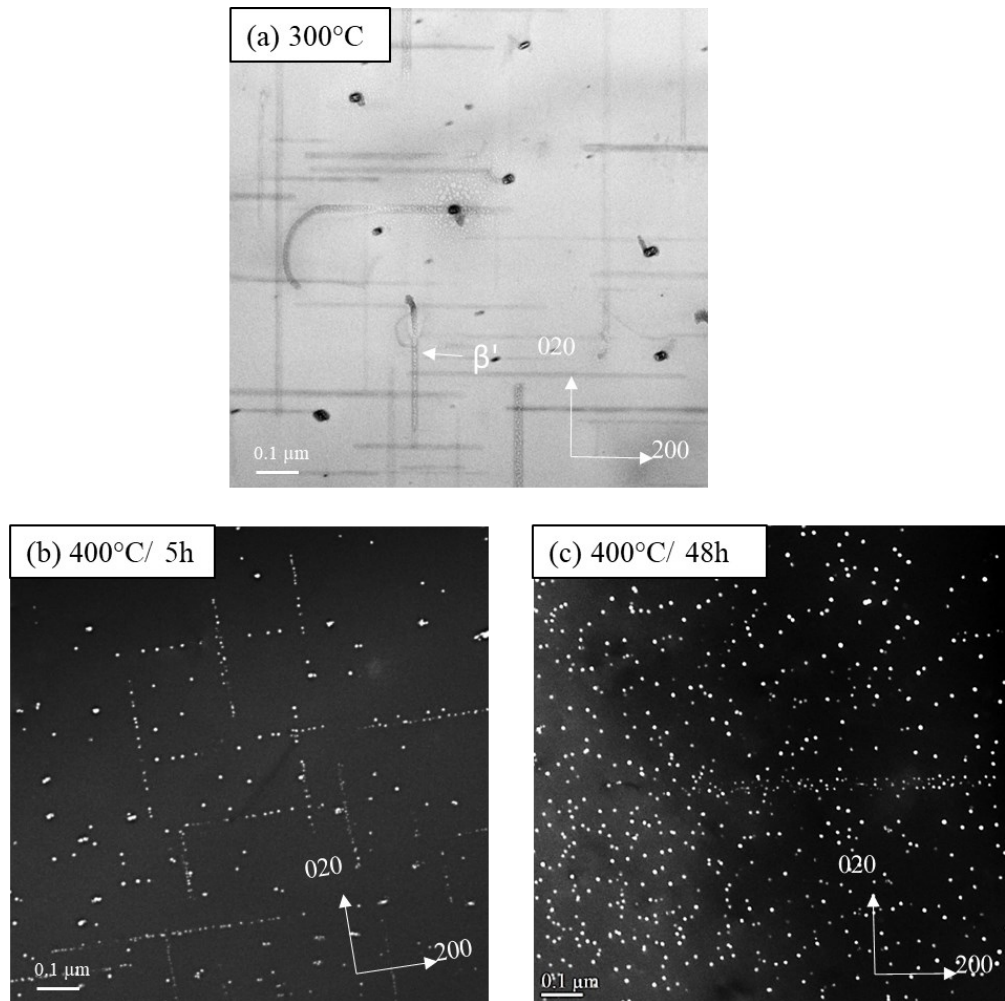


Figure 5.4 a) bright-field TEM image showing the precipitation of β' - $Mg_{1.8}Si$ in the L-Si alloy quenched at 300 °C, and the dark-field TEM images of $L1_2$ - Al_3Zr precipitation after isothermal holding at 400 °C for (b) 5 h and (c) 48 h.

The above results suggest that the pre-existing β' -Mg_{1.8}Si precipitates that formed and then dissolved during heating ramp to the precipitation temperature of the L₁₂-Al₃Zr dispersoids (~400 °C) provided favorable nucleation sites of L₁₂-Al₃Zr in both L-Si and H-Si alloys. These sites became enriched by Si atoms after the dissolution of β' -Mg_{1.8}Si precipitates. Zhen *et al.* [20] observed higher Si concentration at the sites of dissolved β' -Mg_{1.8}Si precipitates compared to the surrounding aluminum matrix, resulting in local Si-enriched sites. In the present study, such sites would promote the nucleation of Al₃Zr dispersoids during isothermal holding. Due to the strong attractive energy between Si and vacancies, Si-vacancy clusters can form and serve as nucleation sites for Al₃Zr dispersoids, as was previously reported in the literature [9, 21, 22]. Several studies reported the significant effect of Si on the precipitation kinetics of trialuminides in general, and specifically of Al₃Zr [10, 21, 23]. It should be mentioned that no precipitation of L₁₂ dispersoids was observed on the equilibrium β -Mg₂Si particles when the precipitation of these dispersoids started.

The precipitation of L₁₂-Al₃Zr dispersoids could also vary with the supersaturation of Zr solutes across the dendrite grain. The level of Zr supersaturation plays an essential role that affects the activation energy barrier for nucleation and hence the amount of precipitation [5]. Zr atoms are known to be enriched in the centers of dendrite cells/grains due to their segregation during the solidification process [24]. Figure 5.5 displays a montage of dark-field TEM images (assembly of several images) showing the precipitation of Al₃Zr dispersoids in the H-Si alloy from the grain boundary towards the grain interior after holding at 400 °C for 12 h. On the left-hand side, few L₁₂ dispersoids appeared because the Zr supersaturation level was quite low near the grain boundary. The preferred precipitation

direction of $L1_2$ dispersoids along $\langle 001 \rangle_{Al}$ was clearly visible, coinciding entirely with the orientation of the previous β' precipitates. When moving towards the grain center, the Zr supersaturation increased and consequently the number density of Al_3Zr dispersoids increased, reaching a maximum in the grain center (right-hand side). The preferred orientation along $\langle 001 \rangle_{Al}$ became less visible compared to the region close to the grain boundary.

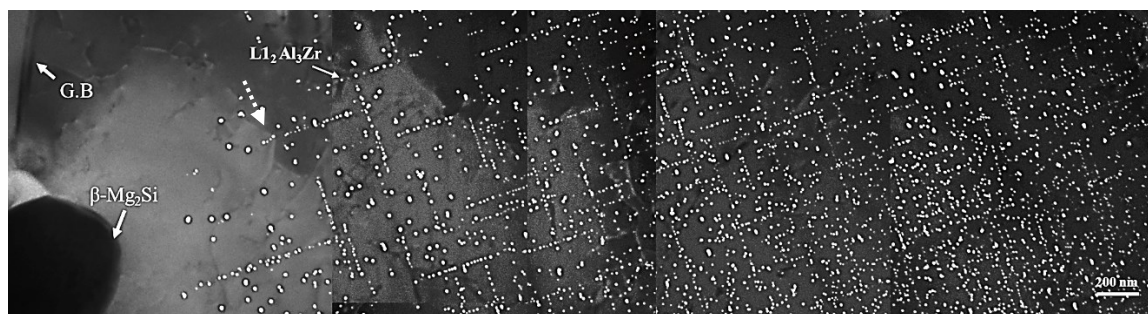


Figure 5.5 Montage of dark-field TEM micrographs of the sample holding at 400 °C for 12 h showing the precipitation of Al_3Zr dispersoids across the grain.

5.2. The Transformation of $L1_2$ to DO_{22}

The transformation of $L1_2$ to DO_{22} dispersoids was often observed when homogenized or heat-treated at high temperatures [15, 25]. In this regard, the H-Si alloy was selected to study the transformation behavior of the Zr-bearing dispersoids due to the higher number density of dispersoids compared to the L-Si alloy. Figure 5.6 shows TEM images of the dispersoid evolution in the Hi-Si alloy during the heating ramp from 400 °C to 500-550 °C after holding at 400 °C for 48 h (heat treatment II in Fig. 1). Compared with the large quantity of $L1_2$ - Al_3Zr dispersoids observed at 400 °C for 48 h (Fig. 5.2d), a significant reduction in the number density of $L1_2$ dispersoids was observed after ramping to 500 °C with a relatively

large size (Fig. 5.6a). Meanwhile, some dispersoids with an elongated morphology and large size appeared among the fine spherical $L1_2$ dispersoids (circled in Fig. 5.6b). It is worth noting that there were no elongated dispersoids observed during holding at 400 °C for 48 h, which indicated that such dispersoids were developed during heating to 500 °C. When the temperature was raised to 550 °C, the quantity of $L1_2$ dispersoids was further reduced (Fig. 5.6c), while more elongated large dispersoids appeared in the aluminum matrix (Fig. 5.6d). These elongated dispersoids were identified as $DO_{22}-(Al,Si)_3Zr$ phase by means of TEM-EDS analysis and corresponding SADP [25]. It is confirmed in previous studies [13, 26, 27] that $DO_{22}-(Al,Si)_3Zr$ dispersoid possessed a tetragonal crystal structure, which mainly precipitated at high temperatures in 6xxx alloys. The coarse DO_{22} dispersoids also appeared to align along $\langle 001 \rangle_{Al}$, suggesting that their appearance is closely related to the pre-existing $L1_2$ dispersoids (Fig. 5.6d).

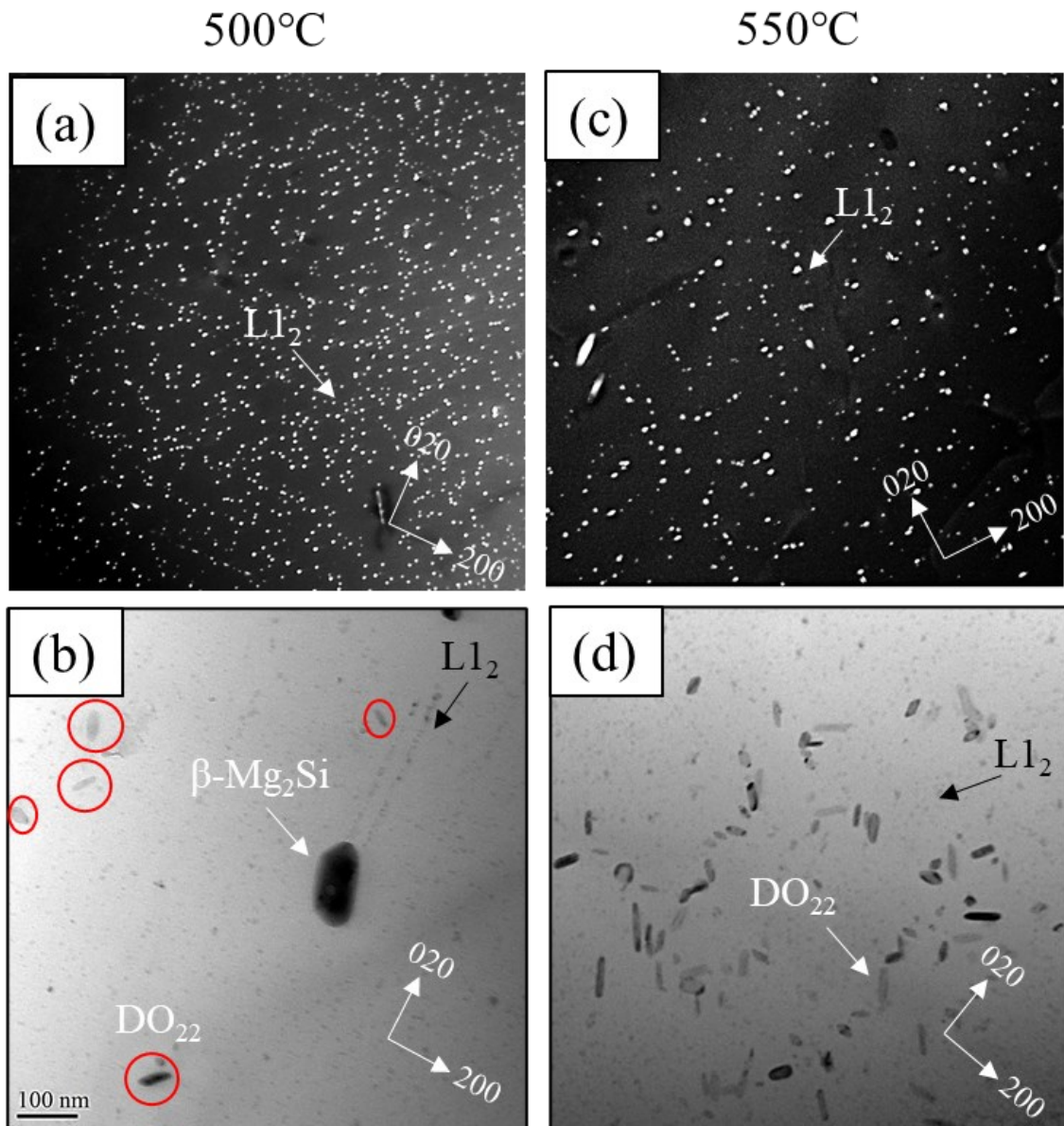


Figure 5.6 The evolution of dispersoids after heating ramp from 400 °C to 500 °C (a,b) and 550 °C (c,d) after the samples hold at 400°C/48h.

Figure 5.7 shows bright-field TEM images of dispersoid transformation from the spherical L₁₂ dispersoids into the elongated DO₂₂ dispersoids along with the TEM-EDS line scans of Si and Zr distribution. The samples were heated from 400 °C to 550 °C after holding at 400°C/48h. First, the spherical L₁₂ dispersoids coarsened (Fig. 5.7a) via the Ostwald

ripening mechanism by the dissolution of surrounding smaller $L1_2$ dispersoids [28]. In this stage, the distribution of Si through the particle showed a negligible change relative to the matrix. Subsequently, the spherical $L1_2$ dispersoids developed into an ellipsoidal morphology (Fig. 5.7b) with a slight but notable increase in Si and a remarkable increase in Zr, which indicates that a transition stage between the spherical $L1_2$ and the elongated DO_{22} dispersoids took place. Eventually, the dispersoids enlarged considerably and transformed to elongated DO_{22} particles (Fig. 5.7c) driven by the diffusion of more Si into the particle, as evidenced by the large peak of Si count in the TEM-EDS line scan. It was reported that Si decreased the stacking fault energy in $L1_2$ dispersoids and consequently lowered the energy barrier for the transformation of metastable $L1_2$ dispersoids to stable DO_{22} dispersoids [14].

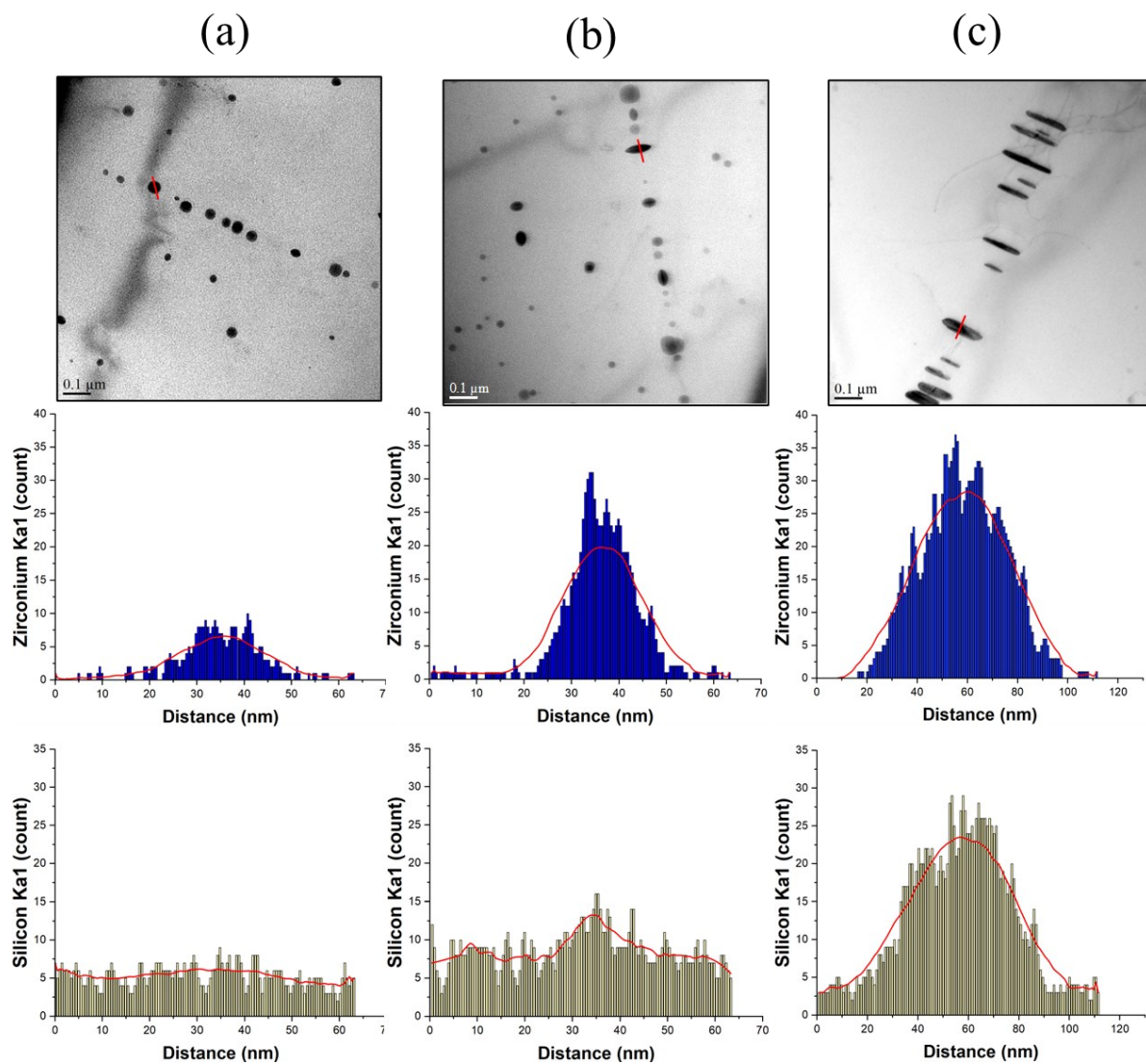


Figure 5.7 Bright-field TEM images during heating to 550 °C after the first step of 400°C/48h and TEM-EDS line scans of Si and Zr distribution across typical dispersoids (arrow-marked); (a) spherical, (b) ellipsoidal and (c) elongated dispersoids.

A thorough TEM examination revealed the details of the transformation sequence from spherical $L1_2$ dispersoids to elongated DO_{22} dispersoids, as shown in Fig.5.8. Structural faults developed inside the coarse spherical dispersoids (Fig. 5.8a). These faults were characterized by sharp lines of dark contrast parallel to $\langle 001 \rangle_{Al}$ in the middle of the

dispersoids. Similar faults have also been reported by other studies that were attributed to the anti-phase boundary (APB) generated by the transition to an imperfect tetragonal DO₂₃ [29]. Hence, they represent the early stages of the transformation of L1₂ to the DO₂₂ structure. Subsequently, several APBs were developed in the particles, which exhibited preferential growth along <001>_{Al}, resulting in an ellipsoidal morphology with a long axis along the anti-phase boundaries, as shown in Fig. 5.8b and its insert. Eventually, the coarsening and growth of the ellipsoidal dispersoids resulted in a complete transformation to elongated DO₂₂ dispersoids (Fig. 5.8c). With multiplying APBs in the particle and further growth, the preferential growth direction of the elongated dispersoids could deviate from the <001>_{Al}, as shown in Figs. 5.6(d) and 5.8(c).

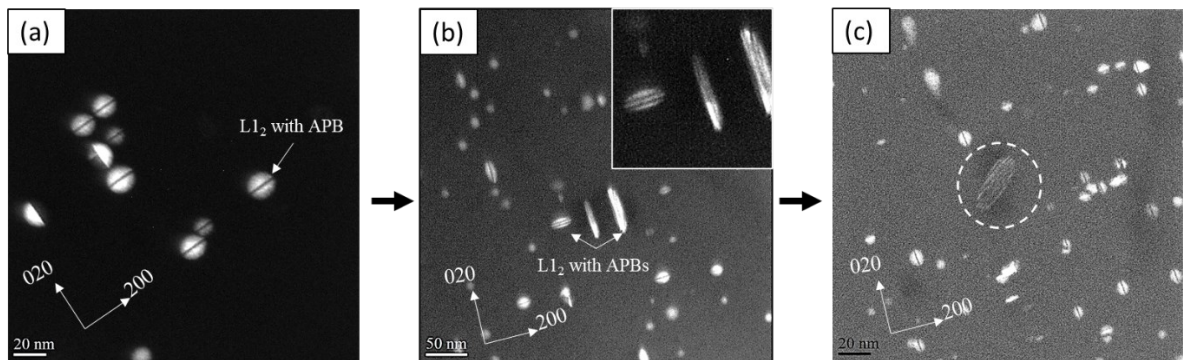


Figure 5.8 Dark-field TEM images showing the transformation sequence of spherical L1₂ dispersoids into elongated DO₂₂ dispersoids.

5.3. The precipitation of dispersoids during one-step treatment

Figure 5.9 shows the precipitation of both L1₂ and DO₂₂ dispersoids after ramp heating directly from room temperature to 500-550 °C with and without holding for 5 h (Heat treatment III, one-step heat treatment in Fig. 5.1). The dark-field TEM images were inserted in each corresponding bright-field TEM image for better showing L1₂ dispersoids. During

heating to 500 °C (Fig. 5.9a), nano-sized L₁₂-Al₃Zr dispersoids (indicated by white arrow) precipitated mainly along $\langle 001 \rangle_{\text{Al}}$. In addition, a limited quantity of small DO₂₂ dispersoids (indicated by black arrow) was observed. After holding at 500 °C for 5 h (Fig. 5.9b), L₁₂ dispersoids underwent coarsening (white arrow) resulting in a significant reduction of the number density, while some DO₂₂ dispersoids grew (black arrow). At this intermediate temperature, L₁₂ and DO₂₂ dispersoids co-existed. On the other hand, increasing the temperature from 500 to 550 °C (Fig. 5.9c) also resulted in a reduction of L₁₂ dispersoids accompanied their transformation to the elongated DO₂₂ dispersoids, which exhibited the same orientation as the pre-existing L₁₂ dispersoids. A dispersoid-free zone around the aligned DO₂₂ dispersoids was observed, suggesting the dissolution of surrounding L₁₂ particles during the transformation and growth of DO₂₂ dispersoids. Subsequently, the transformed DO₂₂ dispersoids coarsened after holding at 550 °C for 5h (Fig. 5.9d), with complete dissolution of the spherical L₁₂-Al₃Zr dispersoids. It is observed that DO₂₂ dispersoids were mostly transformed from pre-existing L₁₂-type dispersoids rather than nucleated directly from the supersaturated aluminum solid solution. This was demonstrated by the alignment of DO₂₂ dispersoids along $\langle 001 \rangle_{\text{Al}}$, which coincided with the same orientation as L₁₂ dispersoids formed earlier. In addition, the coarsening of the DO₂₂ dispersoids occurred by the dissolution of the nearby pre-existing L₁₂ dispersoids, which were less thermodynamically stable at higher temperature than the DO₂₂.

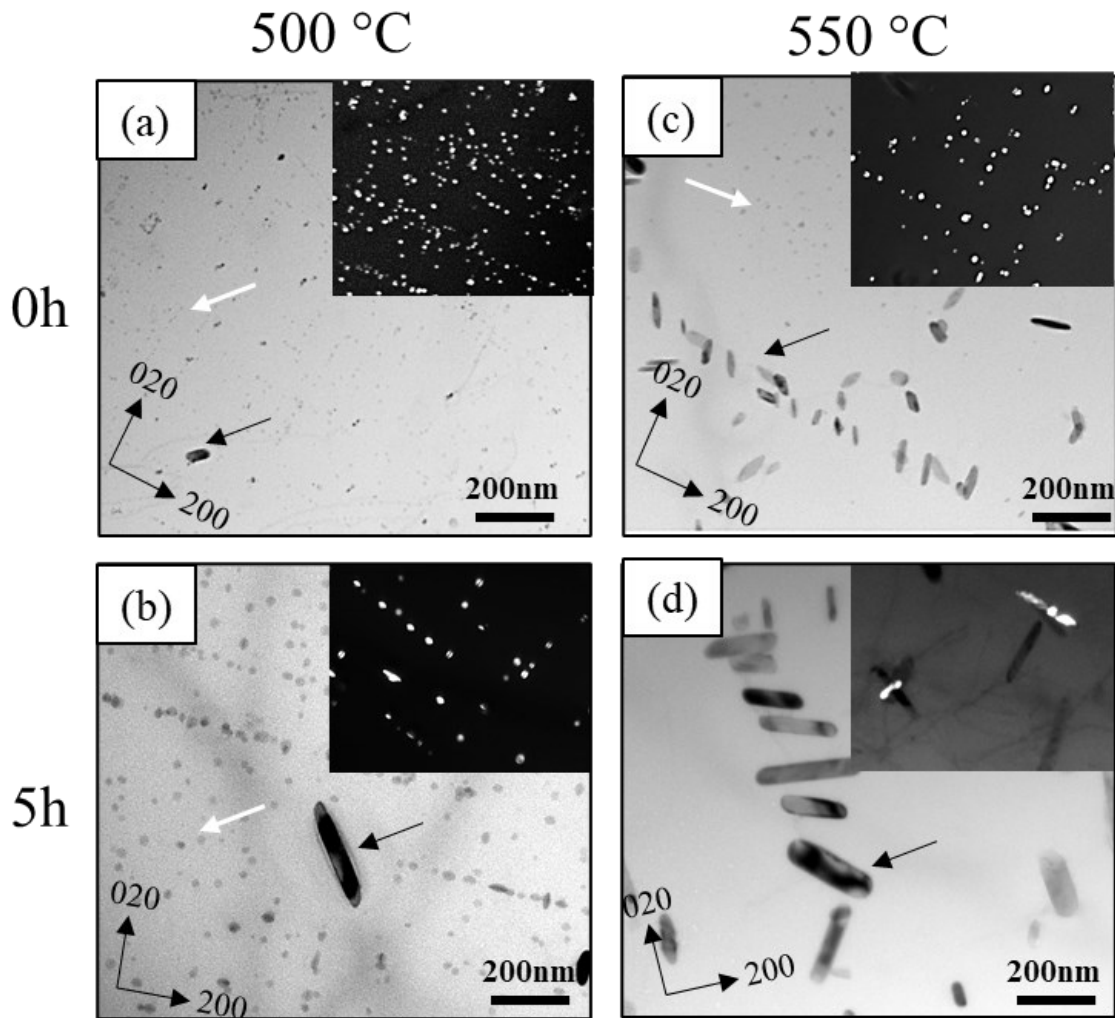


Figure 5.9 The evolution of dispersoids after ramp heating from RT to 500 °C (a,b,c) and 550 °C (d,e,f).

Figure 5.10 presents a schematic illustration of the nucleation and transformation mechanisms for Zr-bearing dispersoids during heat treatment for both L-Si and H-Si alloys. In the early stage of the heating ramp (200-300 °C), a large number of metastable β' -Mg_{1.8}Si precipitates formed with a lath-like morphology (Fig. 5.10a). During further heating towards a high temperature (~400 °C), there are two possible scenarios could happen. The first scenario that β' precipitates were gradually dissolved leaving Si-enriched sites (Fig. 5.10b),

which provided favorable nucleation sites for $L1_2$ - Al_3Zr dispersoids that started to precipitate at ~ 400 °C. With holding at 400 °C, an increased number of $L1_2$ dispersoids preferentially precipitated out along $\langle 001 \rangle_{Al}$ on the Si-enriched sites, where the previous β' precipitates dissolved (Fig. 5.10c). However, there is another possible scenario that Zr atoms were dragged by the interface of β' precipitates resulting in a supersaturation of Zr atoms adjacent to the interface. Such high supersaturation on both sides of the interface promotes the precipitation of $L1_2$ - Al_3Zr dispersoids (Fig. 5.10d).

With prolonging the holding time at 400 °C, more Al_3Zr dispersoids precipitated and grew, resulting in a random distribution of dispersoids (Fig. 5.10d). At relatively low heat treatment temperature, the $L1_2$ - Al_3Zr dispersoids predominated in the aluminum matrix, and no transformation of dispersoids occurred. By increasing the temperature towards 550 °C, the $L1_2$ dispersoids became unstable and started to coarsen through the Ostwald ripening mechanism, while the coarse dispersoids began to transform to the elongated DO_{22} -(Al, Si) $_3Zr$ that exhibited the same orientation as the pre-existing $L1_2$ dispersoids (Fig. 5.10e). Finally, with increased holding time at such high temperature, all remaining $L1_2$ dispersoids completely transformed to DO_{22} dispersoids (Fig. 5.10f). It is apparent that DO_{22} dispersoids were mostly transformed from pre-existing $L1_2$ -type dispersoids rather than precipitated directly from the aluminum matrix.

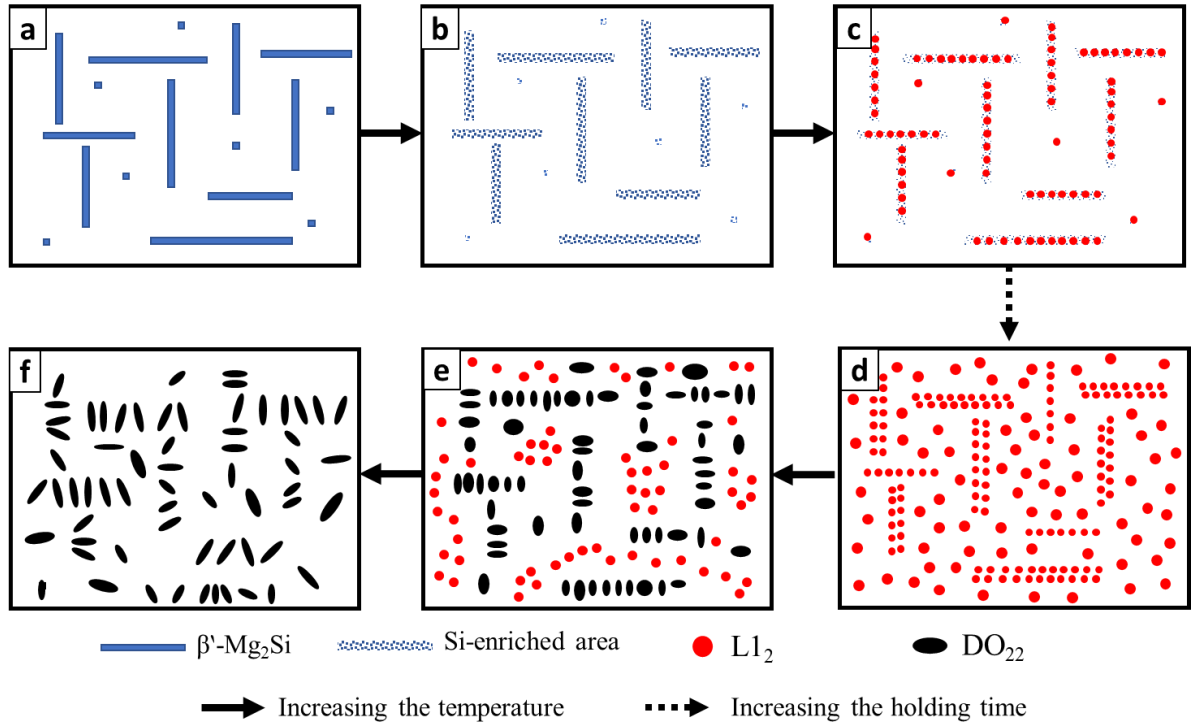


Figure 5.10 Schematic illustration of the nucleation and transformation of Zr-bearing dispersoids in Al-Mg-Si 6xxx alloys.

5.4. Conclusions

The nucleation and transformation behaviours of Zr-bearing dispersoids in Al-Mg-Si alloy were observed after different heat treatments using transmission electron microscopy (TEM). From the results obtained, the following conclusions could be drawn:

- (1) At the early stages of nucleation at 400°C, $L1_2$ - Al_3Zr dispersoids were precipitated aligned with $\langle 001 \rangle \alpha$ -Al, which coincides with the orientation of β' - Mg_2Si phase needles that observed after heating to 300°C. This result suggests that $L1_2$ - Al_3Zr heterogeneous nucleated on the traces of β' - Mg_2Si after dissolving at higher temperatures.
- (2) With prolonging the holding time at 400°C, a remarkable increase in the number density of homogeneously nucleated $L1_2$ was observed, particularly in dendritic regions where the supersaturation level of Zr is sufficiently high. While the near to grain boundary, the heterogeneous nucleation was dominant.
- (3) Further increase in temperature resulted in coarsening and transformation of spherical $L1_2$ dispersoids to elongated DO_{22} dispersoids. However, such transformation was observed to occur more rapidly to the heterogeneously nucleated $L1_2$ dispersoids. This is evident by the distribution of DO_{22} dispersoids along $\langle 001 \rangle \alpha$ -Al at the early stages of transformation.
- (4) The transformation of $L1_2$ dispersoids initiated by introducing antiphase boundary (APB) generated in the middle of the particle. Subsequently, a preferential growth along 001 directions resulting in a small ellipsoidal dispersoids, which indicated a transition stage before the growth to the imperfect DO_{22} structure.

References

1. Chen, K., et al., *Effect of Yb, Cr and Zr additions on recrystallization and corrosion resistance of Al–Zn–Mg–Cu alloys*. Materials Science and Engineering: A, 2008. **497**(1-2): p. 426-431.
2. Clouet, E., J.M. Sanchez, and C. Sigli, *First-principles study of the solubility of Zr in Al*. Physical Review B, 2002. **65**(9): p. 094105.
3. Li, H., et al., *Precipitation evolution and coarsening resistance at 400°C of Al microalloyed with Zr and Er*. Scripta Materialia, 2012. **67**(1): p. 73-76.
4. Nes, E., *Precipitation of the metastable cubic Al₃Zr-phase in subperitectic Al-Zr alloys*. Acta Metallurgica, 1972. **20**(4): p. 499-506.
5. Robson, J.D. and P.B. Prangnell, *Dispersoid precipitation and process modelling in zirconium containing commercial aluminium alloys*. Acta Materialia, 2001. **49**(4): p. 599-613.
6. Liu, Q., et al., *Precipitation of Al₃Zr by two-step homogenization and its effect on the recrystallization and mechanical property in 2195 Al–Cu–Li alloys*. Materials Science and Engineering: A, 2021. **821**: p. 141637.
7. Jia, Z.-H., et al., *Precipitation behaviour of Al₃Zr precipitate in Al–Cu–Zr and Al–Cu–Zr–Ti–V alloys*. Transactions of Nonferrous Metals Society of China, 2012. **22**(8): p. 1860-1865.
8. Mikhaylovskaya, A.V., et al., *Precipitation behavior of L12 Al₃Zr phase in Al-Mg-Zr alloy*. Materials Characterization, 2018. **139**: p. 30-37.
9. Wu, S.H., et al., *Effect of Si addition on the precipitation and mechanical/electrical properties of dilute Al–Zr–Sc alloys*. Materials Science and Engineering: A, 2021. **812**: p. 141150.

10. Vo, N.Q., D.C. Dunand, and D.N. Seidman, *Role of silicon in the precipitation kinetics of dilute Al-Sc-Er-Zr alloys*. Materials Science and Engineering A, 2016. **677**: p. 485-495.
11. Pan, T.-A., et al., *Effects of the coherency of Al₃Zr on the microstructures and quench sensitivity of Al-Zn-Mg-Cu alloys*. Materials Today Communications, 2021. **28**: p. 102611.
12. Knipling, K.E., D.C. Dunand, and D.N. Seidman, *Criteria for developing castable, creep-resistant aluminum-based alloys—A review*. Zeitschrift für Metallkunde, 2006. **97**(3): p. 246-265.
13. Litynska, L., et al., *TEM and HREM study of Al₃Zr precipitates in an Al-Mg-Si-Zr alloy*. J Microsc, 2006. **223**(Pt 3): p. 182-4.
14. Schmid, F., et al., *Stabilization of Al₃Zr allotropes in dilute aluminum alloys via the addition of ternary elements*. Materialia, 2022. **21**: p. 101321.
15. Elasheri, A., et al., *Evolution of Zr-Bearing Dispersoids during Homogenization and Their Effects on Hot Deformation and Recrystallization Resistance in Al-0.8%Mg-1.0%Si Alloy*. Journal of Materials Engineering and Performance, 2021. **30**(10): p. 7851-7862.
16. Andersen, S.J., et al., *The crystal structure of the β'' phase in Al-Mg-Si alloys*. Acta Materialia, 1998. **46**(9): p. 3283-3298.
17. Vissers, R., et al., *The crystal structure of the β' phase in Al-Mg-Si alloys*. Acta Materialia, 2007. **55**(11): p. 3815-3823.
18. Edwards, G.A., et al., *The precipitation sequence in Al-Mg-Si alloys*. Acta Materialia, 1998. **46**(11): p. 3893-3904.
19. Belov, N., et al., *Structure and Properties of Ca and Zr Containing Heat Resistant Wire Aluminum Alloy Manufactured by Electromagnetic Casting*. Metals, 2021. **11**(2): p. 236.

20. Li, Z., Z. Zhang, and Chen, X.G, *Effect of Metastable Mg₂Si and Dislocations on α -Al(MnFe)Si Dispersoid Formation in Al-Mn-Mg xxx Alloys*. Metallurgical and Materials Transactions A, 2018. **49**(11): p. 5799-5814.
21. Booth-Morrison, C., et al., *Role of silicon in accelerating the nucleation of Al₃(Sc,Zr) precipitates in dilute Al-Sc-Zr alloys*. Acta Materialia, 2012. **60**(12): p. 4740-4752.
22. Sato, T., A. Kamio, and G.W. Lorimer, *Effects of Si and Ti Additions on the Nucleation and Phase Stability of the L12-Type Al₃Zr Phase in Al-Zr Alloys*. Materials Science Forum, 1996. **217-222**: p. 895-900.
23. Vo, N.Q., D.C. Dunand, and D.N. Seidman, *Improving aging and creep resistance in a dilute Al-Sc alloy by microalloying with Si, Zr and Er*. Acta Materialia, 2014. **63**: p. 73-85.
24. Jia, Z., et al., *Effect of homogenization and alloying elements on recrystallization resistance of Al-Zr-Mn alloys*. Materials Science and Engineering A, 2007. **444**(1-2): p. 284-290.
25. Elasheri, A., et al., *Effect of Si Level on the Evolution of Zr-Bearing Dispersoids and the Related Hot Deformation and Recrystallization Behaviors in Al-Si-Mg xxx Alloys*. Advanced Engineering Materials, 2022: p. 2101606.
26. Kahriman, F. and M. Zeren, *Microstructural and Mechanical Characterization of Al-0.80Mg-0.85Si-0.3Zr Alloy*. Archives of Foundry Engineering, 2017. **17**: p. 73-78.
27. Meng, Y., et al., *Effect of Zr on microstructures and mechanical properties of an AlMgSiCuCr alloy prepared by low frequency electromagnetic casting*. Materials Characterization, 2014. **92**: p. 138-148.
28. Li, Y., et al., *Two-stage homogenization of Al-Zn-Mg-Cu-Zr alloy processed by twin-roll casting to improve L12 Al₃Zr precipitation, recrystallization resistance, and performance*. Journal of Alloys and Compounds, 2021. **882**: p. 160789.

29. Ding, L., et al., *On the formation of anti-phase boundaries and interphase boundaries in Al₃Zr precipitates of Al-Cu-Zr alloy studied at atomic scale*. Journal of Alloys and Compounds, 2021. **887**: p. 161442.

CHAPTER 6: GENERAL CONCLUSIONS AND RECOMMENDATIONS

6.1. General Conclusions

In this project, the effects of Zr addition on the hot deformation and recrystallization resistance of 6xxx alloys were studied by investigating the evolution of Zr-bearing dispersoids during the homogenization treatment.

- Two-type of Zr-bearing dispersoids were mainly observed depending on the homogenization conditions. At low-temperature homogenization (i.e., 450 °C), the fine, spherical and coherent $L1_2$ - Al_3Zr precipitated, while the larger-sized tetragonal elongated DO_{22} - $(Al,Si)_3(Zr)$ were formed with increasing the homogenization temperature and/or soaking time. The fine Al_3Zr dispersoids (~10 nm) with a uniform distribution resulted in increasing the high-temperature flow stress by 20% relative to the base alloy free of Zr.
- Both types of Zr-bearing dispersoids increased the recrystallization resistance of Zr-containing 6xxx alloy. However, the pinning effect of the $L1_2$ Al_3Zr dispersoids and hence the corresponding recrystallization resistance was significantly higher than that of the DO_{22} - $(Al,Si)_3(Zr)$ dispersoids.
- Si content significantly promoted the transformation of spherical $L1_2$ - Al_3Zr to elongated DO_{22} - $(Al, Si)_3(Zr)$, particularly at high-temperature homogenization (550 °C), where the elongated DO_{22} dispersoids became the predominant at high-silicon alloy (1.0%Si). However, both $L1_2$ and DO_{22} dispersoids were observed at the same

homogenization temperature in the case of low (0.4%Si) and medium Si (0.7%Si) levels.

- The high-temperature flow stress was mainly controlled by the level of solid solution and the hot deformation parameter rather than the dispersoid condition, and hence the flow stress increased with the silicon level. However, the high silicon alloy (1.0%) exhibited superior recrystallization resistance during post-deformation annealing than the low silicon alloys (0.4-0.7%), regardless of the homogenization condition. Such effect was attributed to the more uniform distribution of dispersoids and minimal dispersoid-free zones.
- The two-step homogenization treatments significantly improved the $L1_2$ - Al_3Zr dispersoid characteristics in terms of a higher number density and smaller size, compared to the single-step homogenization treatments of 500 °C/2 and 5 h. Such improvement was attributed to the first step at 400 °C/48 h, producing a high number density of fine-sized Al_3Zr dispersoids. The distribution of elongated $D0_{22}$ dispersoids was more spatially homogenous relative to the single-step homogenization. As a result, the two-step homogenization treatments displayed higher flow stresses and larger inhibition effect of recrystallization compared to the single-step homogenization treatments.
- For the nucleation and transformation of Zr-bearing dispersoids, $L1_2$ - Al_3Zr dispersoids were precipitated aligned with $\langle 001 \rangle_{\alpha-Al}$ during the ramp heating to 400 °C, which coincides with the orientation of β' - Mg_2Si phase needles that observed after heating to 300°C. This result suggests that $L1_2$ - Al_3Zr heterogeneous nucleated on the traces of β' - Mg_2Si after dissolving at higher temperatures. With

prolonging the holding time at 400 °C, a remarkable increase in the number density of homogeneously nucleated $L1_2$ was observed, particularly in dendritic regions where the supersaturation level of Zr is sufficiently high.

- Further increase in temperature resulted in coarsening and transformation of spherical $L1_2$ dispersoids to elongated DO_{22} dispersoids. However, such transformation was observed to occur more rapidly to the heterogeneously nucleated $L1_2$ dispersoids. The transformation of $L1_2$ dispersoids initiated by introducing antiphase boundary (APB) generated in the middle of the particle. Subsequently, a preferential growth along 001 directions resulting in a small ellipsoidal dispersoids, which indicated a transition stage before the growth to the imperfect DO_{22} structure.

6.2. Recommendations

The effect of Zr addition on hot deformation and microstructural evolution of 6xxx alloys after deformation and post-deformation annealing was studied. Furthermore, the evolution of Zr-bearing dispersoids in 6xxx alloys was systematically studied using different homogenization conditions and practices. However, there yet remains several additional issues that are worth investigating. The following recommendations can be drawn for future work in this field:

- Dynamic precipitation and dissolution behaviours of Zr-bearing dispersoids during hot deformation of 6xxx alloys should be studied to understand further the interaction between dislocations and moving boundaries with dispersoids. Also, it will allow an understanding of the deformation flow stress curve as well as the properties after deformation and annealing.
- As the coherent $L1_2$ - Al_3Zr dispersoids showed better recrystallization resistance performance than $D0_{22}$, it is worth studying how to enhance the stability of $L1_2$ by adding other elements such as Mn, Er and Cu.
- Compared to the results of high silicon, studying the nucleation of Zr-bearing dispersoids in low silicon alloy will help to understand the relationship between the β' - Mg_2Si and the nucleation of $L1_2$ Al_3Zr .
- There is still work needed to optimize the homogenization conditions to reduce the segregation of Zr across the grain in order to obtain uniform distribution of Zr dispersoids. On the other hand, the industrial requirements have to be considered during the design of the homogenization treatment.

- Achieving a high age-hardening response is mandatory after the hot deformation process. It would be interesting to study and compare the quench sensitivity of the Zr-containing alloys in the case of having $L1_2$ and DO_{22} dispersoids. Also, the combined effects of Zr dispersoids and Mg/Si precipitates on the final mechanical properties should be studied.

List of Publications

JOURNAL ARTICLES

1. Elasheri, A., Elgallad, E. M., Parson, N., & Chen, X. G., Evolution of Zr-Bearing Dispersoids during Homogenization and Their Effects on Hot Deformation and Recrystallization Resistance in Al-0.8% Mg-1.0% Si Alloy. **Journal of Materials Engineering and Performance**, 2021, doi.org/10.1007/s11665-021-05917-8
2. Elasheri, A., Elgallad, E. M., Parson, N., & Chen, X. G., Effect of Si Level on the Evolution of Zr-bearing Dispersoids and the Related Hot Deformation and Recrystallization Behaviors in Al-Si-Mg 6xxx Alloys, **Advanced Engineering Materials**, 2022, DOI: 10.1002/adem.202101606
3. Elasheri, A., Elgallad, E. M., Parson, N., & Chen, X. G., Improving the dispersoid distribution and recrystallization resistance of a Zr-containing 6xxx alloy using two-step homogenization. **Philosophical Magazine**, 2022
4. Elasheri, A., Elgallad, E. M., Parson, N., & Chen, X. G., On the precipitation and transformation of Zr-bearing dispersoids in 6xxx alloys. **Under review.**

CONFERENCE PAPERS

1. Elasheri, A., Elgallad, E. M., Parson, N., & Chen, X. G., Effect of two-step homogenization on the evolution of Al₃Zr dispersoids in Al-0.3Mg-0.4Si-0.2Zr alloy. **In Proceedings of the 60th Conference of Metallurgists (2021). Awarded the best materials paper (1st prize)**

SCIENTIFIC POSTERS

1. Effect of homogenization treatment on Zr dispersoids evolution in Al-Mg-Si alloys with two Mg and Si levels. (REGAL 2019, ***Awarded best posters prize***).
2. Effects of Zr dispersoids on the flow stress and recrystallization resistance in Al-0.8%Mg-1.0%Si alloy. (REGAL 2020, ***Awarded best posters prize***).
3. Effect of Two-Step Homogenization on Al₃Zr Dispersoids and Flow Stress in Zr-containing Al-Mg-Si Alloy. (REGAL 2021).